

THESIS

OPTOFLUIDIC INTRACAVITY SPECTROSCOPY FOR SPATIALLY, TEMPERATURE,  
AND WAVELENGTH DEPENDENT REFRACTOMETRY

Submitted by

Joel D. Kindt

Department of Electrical and Computer Engineering

In partial fulfillment of the requirements

For the Degree of Master of Science

Colorado State University

Fort Collins, Colorado

Summer 2012

Master's Committee:

Advisor: Kevin L. Lear

Kristen Buchanan  
Branislav Notaros

Copyright by Joel Donald Kindt 2012

All Rights Reserved

## ABSTRACT

### OPTOFLUIDIC INTRACAVITY SPECTROSCOPY FOR SPATIALLY, TEMPERATURE, AND WAVELENGTH DEPENDENT REFRACTOMETRY

A microfluidic refractometer was designed based on previous optofluidic intracavity spectroscopy (OFIS) chips utilized to distinguish healthy and cancerous cells. The optofluidic cavity is realized by adding high reflectivity dielectric mirrors to the top and bottom of a microfluidic channel. This creates a plane-plane Fabry-Perot optical cavity in which the resonant wavelengths are highly dependent on the optical path length inside the cavity. Refractometry is a useful method to determine the nature of fluids, including the concentration of a solute in a solvent as well as the temperature of the fluid. Advantages of microfluidic systems are the easy integration with lab-on-chip devices and the need for only small volumes of fluid. The unique abilities of the microfluidic refractometer in this thesis include its spatial, temperature, and wavelength dependence. Spatial dependence of the transmission spectrum is inherent through a spatial filtering process implemented with an optical fiber and microscope objective.

A sequence of experimental observations guided the change from using the OFIS chip as a cell discrimination device to a complimentary refractometer. First, it was noted the electrode structure within the microfluidic channel, designed to trap and manipulate biological cells with dielectrophoretic (DEP) forces, caused the resonant wavelengths to blue-shift when the electrodes were energized. This phenomenon is consistent with the negative  $dn/dT$  property of water and water-based solutions. Next, it was necessary to develop a method to separate the optical path length into physical path length and refractive index. Air holes were placed near the

microfluidic channel to exclusively measure the cavity length with the known refractive index of air. The cavity length was then interpolated across the microfluidic channel, allowing any mechanical changes to be taken into account.

After the separation of physical path length and refractive index, it was of interest to characterize the temperature dependent refractive index relationship,  $n(T)$ , for phosphate buffered saline. Phosphate buffered saline (PBS) is a water-based solution used with our biological cells because it maintains an ion concentration similar to that found in body fluids. The  $n(T)$  characterization was performed using a custom-built isothermal apparatus in which the temperature could be controlled. To check for the accuracy of the PBS refractive index measurements, water was also measured and compared with known values in the literature. The literature source of choice has affiliations to NIST and a formulation of refractive index involving temperature and wavelength dependence, two parameters which are necessary for our specialized infrared wavelength range. From the NIST formula, linear approximations were found to be  $dn/dT = -1.4 \times 10^{-4}$  RIU  $^{\circ}\text{C}^{-1}$  and  $dn/d\lambda = -1.5 \times 10^{-5}$  RIU  $\text{nm}^{-1}$  for water.

A comparison with the formulated refractive indices of water indicated the measured values were off. This was attributed to the fact that light penetration into the  $\text{HfO}_2/\text{SiO}_2$  dielectric mirrors had not been considered. Once accounted for, the refractive indices of water were consistent with the literature, and the values for PBS are believed to be accurate. A further discovery was the refractive index values at the discrete resonant wavelengths were monotonically decreasing, such that the  $dn/d\lambda$  slope for water was considerably close to the NIST formula. Thus,  $n(T,\lambda)$  was characterized for both water and PBS.

A refractive index relationship for PBS with spatial, temperature, and wavelength dependence is particularly useful for non-uniform temperature distributions caused by DEP

electrodes. First, a maximum temperature can be inferred, which is the desired measurement for cell viability concerns. In addition, a lateral refractive index distribution can be measured to help quantify the gradient index lenses that are formed by the energized electrodes. The non-uniform temperature distribution was also simulated with a finite element analysis software package. This simulated temperature distribution was converted to a refractive index distribution, and focal lengths were calculated for positive and negative gradient index lenses to a smallest possible length of about 10mm.

## ACKNOWLEDGEMENTS

It has been a fulfilling experience as a graduate student in the ECE department at Colorado State University, Fort Collins. I would like to thank my advisor Dr. Kevin L. Lear, for his enduring support and guidance through this great learning experience. I would also like to thank my committee members Dr. Kristen Buchanan and Dr. Branislav Notaros for their feedback and help to keep me on track. A most appreciated thank you goes to Dr. Dave Kisker, for his insight on the project and advice to help me become a better engineer. I would like to thank the many Optoelectronics group members I have had the privilege of working with over the years. In particular, I would like to thank Weina Wang and Ishan Thakkar for fabricating OFIS chips for me outside of their own obligations.

Most importantly, I would like to thank my loving family for their patience and continued encouragement. I could not have done it without them.

## TABLE OF CONTENTS

ABSTRACT.....	ii
ACKNOWLEDGEMENTS.....	v
Chapter 1: Introduction.....	1
1.1 Motivation.....	1
1.2 Overview of chapters.....	2
References.....	3
Chapter 2: Background.....	4
2.1 Optical cavities.....	4
2.1.1 Classic Fabry-Pérot.....	5
2.1.2 Dielectric mirrors.....	9
2.2 Dielectric properties of liquid water.....	10
2.2.1 Dielectric spectroscopy of water between 0-25THz.....	11
2.2.2 Relations between complex permittivity, RI, and absorption.....	14
2.2.3 Absorption spectrum of water with temperature dependence.....	16
2.2.4 Refractive index spectrum of water with temperature dependence.....	20
2.2.5 High conductivity solutions at optical frequencies.....	26
2.3 Single-cell manipulation and analysis with electric fields.....	30
2.3.1 Dielectrophoresis and electro-rotation.....	30
2.3.2 Electroporation of cells.....	34
2.3.3 Double-layer capacitance.....	39
2.3.4 Impedance spectroscopy.....	41
2.4 Literature review of joule heating in microfluidic systems.....	43
2.4.1 Ross <i>et al.</i> , 2001.....	44
2.4.2 Seger-Sauli <i>et al.</i> , 2005.....	45
2.4.3 Jaeger <i>et al.</i> , 2007.....	48

2.5	Literature review of microfluidic F-P refractometers .....	49
2.5.1	Device 1: Domachuk <i>et al.</i> , 2006.....	50
2.5.2	Device 2: Song <i>et al.</i> , 2006.....	51
2.5.3	Device 3: St-Gelais <i>et al.</i> , 2009 .....	53
2.5.4	Device 4: Chin <i>et al.</i> , 2010 .....	56
2.5.5	Summary of all devices.....	58
	References .....	60
Chapter 3: Modeling .....		66
3.1	Electrostatics .....	66
3.1.1	Electrostatic equations .....	67
3.1.2	Dielectrophoresis .....	68
3.1.3	Model and results .....	70
3.2	Joule heating.....	76
3.2.1	AC joule heating .....	76
3.2.2	Temperature dependent parameters .....	77
3.2.3	Model and results .....	79
3.3	Optics .....	83
3.3.1	Mirror penetration depth.....	84
3.3.2	F-P spectra with mirror penetration .....	89
3.3.3	Method to obtain GRIN lens focal length.....	93
3.3.4	Positive and negative GRIN lenses.....	99
3.3.5	Cavity stability with GRIN lenses .....	106
	References .....	108
Chapter 4: Materials and methods .....		111
4.1	OFIS chip .....	111
4.2	Experimental methods.....	113
4.2.1	Transmission spectrum collection.....	113
4.2.2	Mirror penetration depth consideration .....	115
4.2.3	Cavity length interpolation .....	117

4.2.4	Refractive index measurements with isothermal apparatus .....	119
4.2.5	Refractive index measurements with joule heating .....	121
	References .....	122
Chapter 5: Experimental results .....		123
5.1	Cavity length interpolation observations .....	123
5.1.1	Position, size, and number of air holes .....	123
5.1.2	Air hole dynamics .....	125
5.1.3	Hypotheses for air hole dynamics .....	126
5.2	RI measurements with isothermal apparatus .....	129
5.2.1	Isothermal apparatus details .....	129
5.2.2	Chip 28-Jun-2011 .....	130
5.2.3	Chip 20-Aug-2011 .....	132
5.2.4	H <sub>2</sub> O vs. NIST, PBS vs. H <sub>2</sub> O, and PBS average .....	134
5.2.5	Problem with data processing algorithm .....	137
5.2.6	Justification of linear RI approximation .....	138
5.3	RI measurements with joule heating .....	138
5.3.1	Chip 05-Apr-2011 .....	139
5.3.2	Experimental and simulated refractive index distributions .....	142
5.3.3	Implication of experimental and simulated results .....	144
5.4	GRIN lens imaging .....	145
	References .....	147
Chapter 6: Conclusions and future work .....		149
6.1	Contributions and practical considerations of the thesis .....	149
6.1.1	RI measurements .....	150
6.1.2	Gradient index lenses .....	152
6.2	Future work .....	153
	References .....	154
Appendix A: Derivations .....		155

A.1	Fabry-Pérot transmission.....	155
A.2	Electrostatic equations.....	160
A.3	Maxwell's equations to plane waves.....	161
A.4	Thermal circuit model .....	164
A.5	Round-trip phase to calculate $L_{FP}$ and $n_{FP}$ .....	166
	References .....	171
Appendix B: Diffraction limit of microscope.....		172
	References .....	174
Appendix C: Additional experimental work.....		175
C.1	DEP force magnitude from particle velocity.....	175
C.2	RI measurements using lab refractometer .....	177
C.3	Table of experiments .....	178
	References .....	180
Appendix D: COMSOL Multiphysics .....		181
D.1	DEP force directional arrows .....	181
D.2	Short tutorial to reproduce joule heating results .....	182
D.3	Comparison of results on different computers .....	190
Appendix E: PBS recipe .....		193
Appendix F: TFCalc references for $H_2O$ , $HfO_2$ , $SiO_2$ .....		194
Appendix G: Relevant journals.....		196
	References .....	198

# Chapter 1: Introduction

## 1.1 Motivation

The emerging field of optofluidics integrates optical devices with fluidic channels, often at the micro scale level. Optofluidics has great potential in biosensing applications where a fluid carries a substance to a very sensitive microphotonic circuit for analysis. These devices can provide a laboratory sensing performance with high portability, low cost, and low sample volume. Furthermore, microfluidics can be exploited to tune microphotonic devices, such as dye lasers [1].

The refractive index of a fluid is a useful optical parameter for *in-situ* measurements in a microfluidic channel. First, refractive index can determine a concentration of a solute in a solvent, and is of particular interest to determine the tonicity of a buffer solution. Secondly, refractive index can be a temperature indicator due to the temperature dependence of refractive index in fluids. Temperature is of specific interest to microfluidic channels that implement non-uniform electric fields to create a dielectrophoretic (DEP) force to trap or position biological cells. The high electric fields in combination with the high conductivity of the phosphate buffered saline needed for cells gives rise to joule heating in the microfluidic channel. Viability of the cells depends on the temperature and time of heat exposure [2]. To determine the non-uniform lateral temperature distribution caused by joule heating, high spatial resolution is needed. Previous work with the thermo-dependent fluorescent dye Rhodamine B has shown temperature distributions with high spatial resolutions of  $1\mu\text{m}$  [3]. However, Rhodamine B can be toxic to cells [4] at the  $1\text{mM}$  concentration needed for fluorescence [5].

In this thesis, an optofluidic device is created by combining a microfluidic channel with Fabry-Perot interferometer. The technique has been named optofluidic intracavity spectroscopy

(OFIS) and has been used previously to distinguish biological cells [6]. Similar work has already been done to measure refractive index in a microfluidic channel with a Fabry–Perot cavity formed between resonant Bragg grating reflectors [7], and with an evanescent field-based optical fiber sensing device [8]. Our advantage is the ability to measure temperature dependent refractive index (RI) because the optical system is compatible with an isothermal temperature apparatus and the method provides the ability to calibrate out mechanical changes with temperature.

## **1.2 Overview of chapters**

The thesis is presented in a typical format. In Chapter 2, a detailed background is provided, including much detail on the complex permittivity of water. Chapter 2 also contains a literature review of joule heating in microfluidic systems and other Fabry-Pérot microfluidic refractometers. In Chapter 3, modeling is provided to compliment experimental work, and categories include electrostatics, joule heating, and optics. Chapter 4 gives details of the experimental materials and methods, followed by the experimental work in Chapter 5. Lastly, Chapter 6 provides a conclusion of the thesis and possible future work.

## References

- [1] C. Monat, P. Domachuk, and B. J. Eggleton, "Integrated optofluidics: a new river of light," *Nature Photonics*, vol. 1, no. 2, pp. 106-114, 2007.
- [2] X. He and J. C. Bischof, "The kinetics of thermal injury in human renal carcinoma cells," *Annals of Biomedical Engineering*, vol. 33, no. 4, pp 502-510, May 2005.
- [3] D. Ross, M. Gaitan, and L. E. Locascio, "Temperature measurement in microfluidic systems using a temperature-dependent fluorescent dye," *Anal. Chem*, vol. 73, no. 17, pp. 4117-4123, 2001.
- [4] R. S. Gupta and A. K. Dudani, "Species-specific differences in the toxicity of Rhodamine 123 toward cultured mammalian cells," *Journal of Cellular Physiology*, vol. 130, no. 3, pp. 321-327, 1987.
- [5] U. Seger-Sauli, M. Panayiotou, S. Schnydrig, M. Jordan, and P. Renaud, "Temperature measurements in microfluidic systems: Heat dissipation of negative dielectrophoresis barriers," *Electrophoresis*, vol. 26, no. 11, pp. 2239-2246, 2005.
- [6] W. Wang and K. L. Lear, "A cell lens model for transverse modes in optofluidic intracavity spectroscopy," *IEEE J. Sel. Topics Quantum Electron.*, vol. 16, no. 4, pp. 946-953, 2010.
- [7] P. Domachuk, I. C. M. Littler, M. Cronin-Golomb, and B.J. Eggleton, "Compact resonant integrated microfluidic refractometer," *Applied Physics Letters*, vol. 88, no. 9, 2006.
- [8] P. Polynkin, A. Polynkin, N. Peyghambarian, and M. Mansuripur, "Evanescent field-based optical fiber sensing device for measuring the refractive index of liquids in microfluidic channels," *Optics Letters*, vol. 30, no. 11, pp. 1273-1275, 2005.

## **Chapter 2: Background**

This chapter reviews background information for the work. First, the basic physics behind optical cavities will be presented. The project started out utilizing a type of optical cavity known as a Fabry-Pérot interferometer that also acted as a microfluidic channel. Biological cells in the channel could be distinguished as healthy or cancerous with their transmission spectrum. However, this work branched off to use the interferometer exclusively for refractometry with temperature and wavelength dependence. Earlier information on single-cell manipulation and analysis with electric fields will still be included in this background. A detailed literature review will then be conducted on joule heating and other microfluidic Fabry-Pérot refractometer devices.

### **2.1 Optical cavities**

An optical cavity, or optical resonator, is an arrangement of mirrors that form standing waves between the mirrors. These cavities are a major component of lasers and are the basic component of Fabry-Pérot interferometers. One of the more important characteristics of an optical cavity is the resonance of electromagnetic waves. This resonance causes transmitted intensity distributions at discrete wavelengths, known as modes. Modes can be divided into two types: longitudinal and transverse. Longitudinal modes differ in frequency and have identical intensity distributions, whereas transverse modes may differ in both frequency and intensity. The cavity geometry will determine the type of modes, the resonant wavelengths, as well as the cavity stability. Figure 2.1 illustrates some common optical cavity geometries.

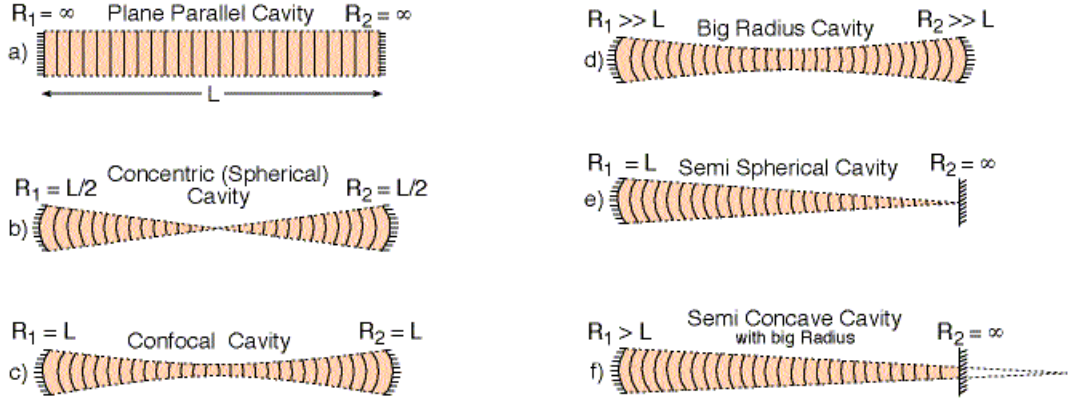


Figure 2.1 Common geometries of optical cavities, where  $R$  is the radius of curvature of the mirror, and  $L$  stands for the separation between the mirrors. (Reproduce from [1])

The geometry in this work is a plane parallel cavity. The mathematics for transverse modes in a semi concave cavity is well-established with Hermite-Gaussian modes [2]. Thus, to check for the existence of transverse modes in a plane parallel cavity, one can examine a semi concave cavity at the limit where both mirrors are planer. The longitudinal mode  $q$ , and transverse modes  $m$  and  $p$  are at the following frequencies:

$$\nu_{m,p,q} = \frac{c}{2nL} \left\{ q + \frac{1+m+p}{\pi} \tan^{-1} \left[ \frac{(L/R_1)^{1/2}}{(1-L/R_1)^{1/2}} \right] \right\} \quad (2.1)$$

where  $c$  is the speed of light,  $n$  is the refractive index in the cavity,  $L$  is the distance between the mirrors, and  $R_1$  is the radius of curvature of the first mirror. If the first mirror is planer ( $R_1 = \infty$ ), then the arc tangent term becomes  $\tan^{-1}[0] = 0$  and there are no transverse modes. A ray optics approach will be sufficient to describe the longitudinal modes of the Fabry-Pérot interferometer.

### 2.1.1 Classic Fabry-Pérot

The Fabry-Pérot (FP) interferometer was devised by C. Fabry and A. Perot in 1899 and employs multiple beam interference. The interferometer consists of two optically flat, partially reflecting plates of glass or quartz with their reflecting surfaces held parallel to each other. A

naming convention arises between an FP interferometer and an etalon. If the mirrors can be mechanically varied, the device is called an interferometer, whereas if the plates are held by fixed spacers, it is called an etalon [3]. This work intends for an etalon but experimental results will show an interferometer. For simplicity, the mirrors are considered infinitely thin. The simplification is a reasonable for now to derive the transmission spectrum of the FP interferometer. Our device actually employs dielectric mirrors, which will be presented later.

Figure 2.2 presents a diagram of the FP interferometer, in which the transmission spectrum occurs on the right-hand side of the interferometer. This diagram also shows the necessary parameters to derive the transmission spectrum. Only important parts of the derivation are presented here and further details are in Appendix A.1. The phase difference between any two successive rays is given by  $\delta = 2kL\cos\theta$ , where the wavenumber  $k = 2\pi n / \lambda$ ,  $n$  is the refractive index inside the cavity,  $L$  is the distance between the mirrors, and  $\theta$  is the angle the light travels through the cavity. Since there are two reflections between the beams, the  $\pi$  phase shift on each reflection results in the same phase of  $2\pi$  between the rays and can be ignored. It is also assumed there is no lag in phase caused by the mirrors. The transmission spectrum of the FP interferometer is found by adding all of the transmitted fields,  $E_T = E_0t^2 + E_0t^2r^2e^{i\delta} + E_0t^2r^4e^{i2\delta} + \dots$  which is a geometric series. A few algebraic tricks were played and the resulting transmission intensity  $I_T$  is given by:

$$\frac{I_T}{I_0} = \frac{1}{1 + F \sin^2(\delta/2)} \quad (2.2)$$

where  $I_0$  is the intensity distribution of the light source, the coefficient of finesse is  $F = 4R/(1-R)^2$  and  $R$  is the reflection of each mirror. The reflection of the mirrors is

traditionally different in a laser cavity and variables for  $R_1$  and  $R_2$  are needed. Equation 2.2 will often be referred in this work as the FP Equation.

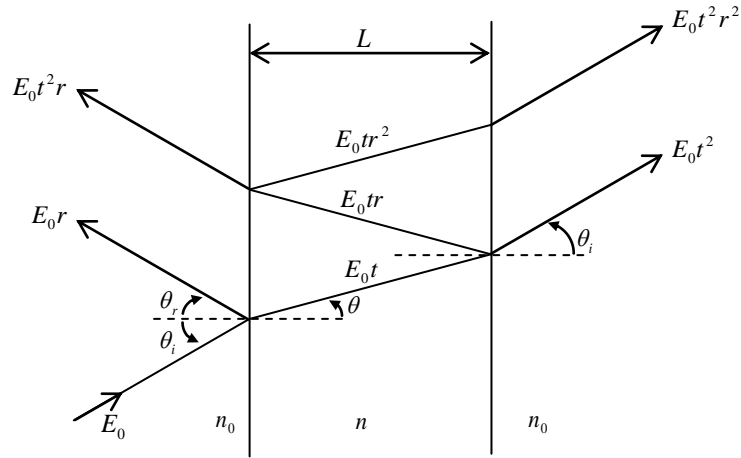


Figure 2.2 Path of light rays between two parallel mirrors creating a Fabry-Pérot interferometer. The lower case letters ‘ $r$ ’ and ‘ $t$ ’ are the Fresnel amplitude coefficients for field reflection and transmission, respectively.

As seen by Eq. 2.2, there will be points of maximum transmission when either the coefficient of finesse or the sine squared term is zero. For the coefficient of finesse to be zero, the reflection of the mirrors is zero and there is no actual optical cavity. The sine squared term is zero when  $\delta/2 = m\pi$ , where  $m$  is the integer set  $m = \{\dots, -2, -1, 0, 1, 2, \dots\}$ . However,  $\delta/2 = 0$  means the wavelength is infinite, the refractive index is zero, or cavity length is zero, which are not physical realities for the optical cavity. Negative integers can be considered redundant such that only positive integers are used. Consequently, the resonant wavelengths will occur at  $(2\pi m / \lambda_m) L \cos \theta = m\pi$ . It is assumed  $\theta = 0$  in our case because the LED is placed far enough away so that rays are normally incident on the cavity. Solving for the resonant wavelength results in the equation  $\lambda_m = 2nL/m$ .

The transmission spectrum is highly dependent on the finesse of the cavity. Finesse is related to the coefficient of finesse by the following:

$$\mathcal{F} = \frac{\pi}{2} \sqrt{F} = \frac{\pi \sqrt{R}}{1-R} \quad (2.3)$$

where each mirror has the same reflectance  $R$ . This representation of finesse is purely based on the mirror reflection. Different factors affect the finesse and are addressed in H. Shao's dissertation, Ch. 3 [4]. Rearranging Eq. 2.2 to be in terms of finesse:

$$\frac{I_T}{I_0} = \frac{1}{1 + (2\mathcal{F}/\pi)^2 \sin^2(\delta/2)} \quad (2.4)$$

Figure 2.3(a) is a visualization of the transmission spectrum over a wavelength range that is comparable to the range of our LED and with a finesse of 40. Figure 2.3(b) demonstrates the transmission spectrum over a narrow wavelength range at selected finesse values of 5, 10, 20, and 40. Lastly, Table 2.1 includes finesse values and the corresponding reflection of the mirrors.

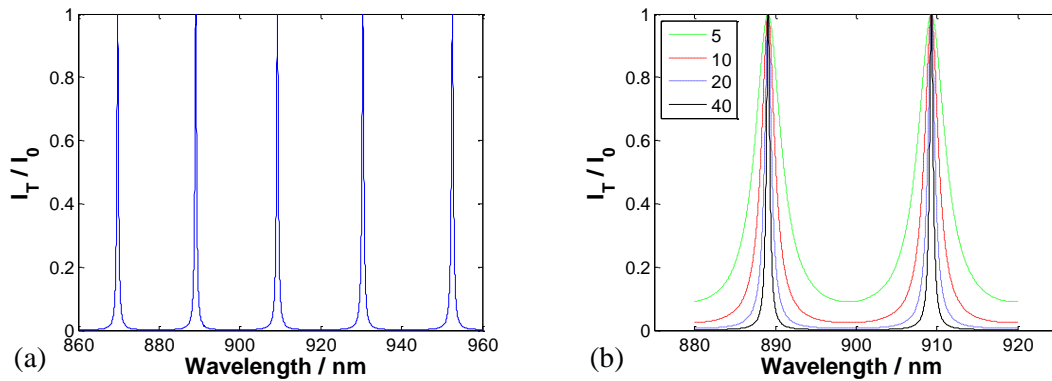


Figure 2.3 Transmission spectrum for (a) a wavelength range comparable to our LED and a finesse of 40 and (b) a narrow wavelength range at selected finesse values.

Table 2.1 Doubling finesse values and corresponding reflection of the mirrors, where  $R = R_1 = R_2$ .

$\mathcal{F}$	$R / \%$
5	53.88
10	73.13
20	85.48
40	92.45
80	96.15
160	98.06

### 2.1.2 Dielectric mirrors

A dielectric mirror, Bragg mirror, or quarter-wave mirror is a type of mirror composed of multiple thin layers of dielectric material typically deposited on a substrate. The material is referred as dielectric because it has a different refractive index. The layers are each a quarter-wavelength thick in order to take advantage of constructive interference and create high reflectivity. Figure 2.4 provides a ray diagram to show the concept of constructive interference with a dielectric mirror.

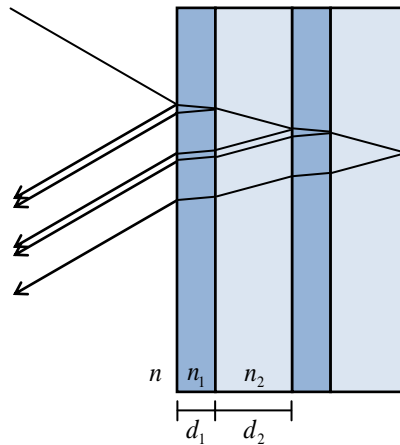


Figure 2.4 Path of light rays incident on a dielectric mirror. The rays in the incident medium will constructively interfere because of the phase shifts of the mirror.

In this figure,  $n$  is a lower refractive index,  $n_1$  is higher refractive index, and  $n_2$  is lower refractive index. Constructive interference occurs when the wave is at the same phase. The following lists the phase shifts in a dielectric mirror:

- When a ray reflects off a higher refractive index, there will be a phase shift of  $\pi$ .
- When a ray reflects off a lower refractive index, there is no phase shift.

- When the ray travels through one quarter-wavelength layer and reflects back, or a total of a half-wavelength, there is a phase shift of  $\pi$ .

Consequently, all rays in material  $n$  will be at the same phase and will constructively interfere.

The reflectance of the dielectric mirror depends on the wavelength of the incident light, such that there will be a reflectance spectrum. The maximum reflectance will be at the wavelength that determined the quarter-wavelength thickness of the layers, otherwise known as the center wavelength of the mirror. Additional spectrum characteristics include the bandwidth and the value of the maximum reflectance. Both of these characteristics depend on the types of materials and the number of layers. In general, increasing the number of layers increases the mirror reflectivity, and increasing the index contrast between the materials increases the bandwidth.

The reflectance spectrum can be determined by either transfer-matrix analysis or simulation software. One should note transfer matrices are developed from electromagnetic boundary conditions and are unlike ABCD matrices used for ray tracing. Simulation software, such as TFCalc, is easier to use than matrices for multiple reasons: it includes a database of materials with reliable refractive index values that are wavelength dependent, and it easily produces spectrum whereas transfer matrices still need a computer to sweep the wavelengths. Chapter 3 will present simulation results of the dielectric mirrors. Furthermore, Fig. 2.4 illustrates that light will penetrate into the mirrors and cause the cavity length of the Fabry-Pérot interferometer to appear longer. This will also be addressed further in Chapter 3.

## **2.2 Dielectric properties of liquid water**

In this section, the dielectric properties of liquid water are explored. A dielectric material is an electrical insulator that can be polarized by an applied electric field. In this work, both

electrostatic and electromagnetic fields are applied. Polarization occurs when the electric field aligns the charges such that positive charges are displaced in the direction of the field and negative charges shift in the opposite direction. This is contrasted with a conductive material, in which charges flow with the application of a field. A dielectric material may also be a partially conductive. The amount by which the dielectric material is conductive can be a qualification of how ‘good’ the dielectric is.

### 2.2.1 Dielectric spectroscopy of water between 0-25THz

Dielectric spectroscopy is important to address because the permittivity of water is highly frequency dependent. In this work, a static electric field around 50MHz is applied to the electrodes and a radiation source around 333THz is provided by the near-infrared LED. Even though it is possible to quantify permittivity near those frequencies, it is useful to visualize the spectrum of permittivity and understand why it changes with frequency. A complete description is given by complex permittivity to include different energy responses. When an electric field is applied, energy is lost by frictional motion and turned into heat (resistive loss), or is stored by polarization.

Complex permittivity can be illustrated by a simple electrical circuit for static electric fields and an analogy can be made to electromagnetic fields. The circuit for a lossy medium between two electric plates is illustrated in Fig. 2.5. The resulting electrical impedance is given by:

$$Z = \left[ \frac{1}{R} + j\omega C \right]^{-1} = \frac{1}{(j\omega\epsilon + \sigma)A/d} = \frac{1}{j\omega(\epsilon - j\sigma/\omega)A/d} = \frac{1}{j\omega\hat{\epsilon}A/d} \quad (2.5)$$

where  $R$  is the resistance,  $C$  is the capacitance, the complex permittivity is  $\hat{\epsilon} = \epsilon - j\sigma/\omega$ ,  $\epsilon = \epsilon_0\epsilon_r$ ,  $\epsilon_0$  is the vacuum permittivity,  $\epsilon_r$  is the relative permittivity, and  $\sigma$  is the electrical

conductivity. As a result, the electrical impedance is due to a capacitor with a capacitance of  $C = \hat{\epsilon}A/d$ . The impedance for an electromagnetic wave is provided by:

$$\eta = \sqrt{\frac{j\omega\mu}{\sigma + j\omega\epsilon}} = \sqrt{\frac{\mu}{\sigma/j\omega + \epsilon}} = \sqrt{\frac{\mu}{\epsilon - j\sigma/\omega}} = \sqrt{\frac{\mu}{\hat{\epsilon}}} \quad (2.6)$$

where the additional term  $\mu$  is permeability,  $\mu = \mu_0\mu_r$ ,  $\mu_0$  is the vacuum permeability, and  $\mu_r$  is the relative permeability. Consequently, the impedance is the same as given by a dielectric but with complex permittivity.

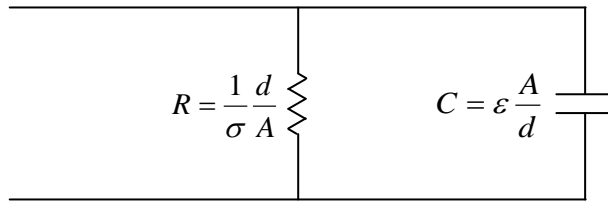


Figure 2.5 An electrical circuit that results in an impedance with complex permittivity.

The complex permittivity of water has been explored by many authors, and experimental data was recently compiled and fit by Ellison over a frequency range from 0 to 25 THz and a temperature range of 0 to 100 °C [5]. Most of the data were obtained at either standard atmospheric pressure or at saturation pressure. Ellison notes that “the variations in permittivity due to differences between standard atmospheric pressure and saturated vapor pressure in this temperature range are very small and, in any case, are considerably smaller than the experimental error in the permittivity data.” The author also describes that permittivity values in the frequency range of 1-25 THz were obtained by converting published refraction and absorption data. Relationships between complex permittivity, complex refractive index, and absorption will be presented in the next section.

Ellison fits the complex permittivity data to a function  $\varepsilon(\nu, t)$  where  $\nu$  is frequency and  $t$  is temperature. Figure 2.6 presents the compilation of permittivity data at 20°C and a fit using two Debye relaxation terms. Dielectric relaxation refers to the relaxation response of a dielectric medium to an external electric field of microwave frequencies. This relaxation can be described by the Debye equation.

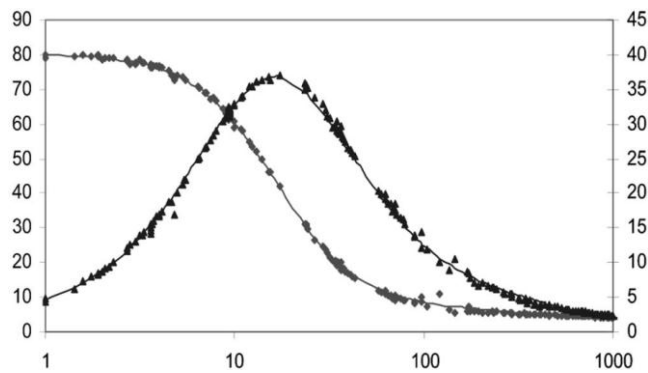


Figure 2.6 Complex permittivity at 20°C from 1 to 1000 GHz, where the real part (diamonds) is on the left axis and the imaginary part (triangles) is on the right axis. (Reproduced from [5])

The fitting is claimed to be excellent for all temperatures and frequencies up to about 500 GHz. Data in the temperature range of 0-100°C and frequencies of 0-3000 GHz are fit with three Debye relaxations. Figure 2.7 illustrates the difference between using two and three relaxation terms at higher frequencies. Their final model for the permittivity of water uses three relaxation terms and two molecular resonance terms. Resonance around 4 THz is attributed to the stretching of intramolecular hydrogen bonds and around 11 THz to librational motions of water molecules [5].

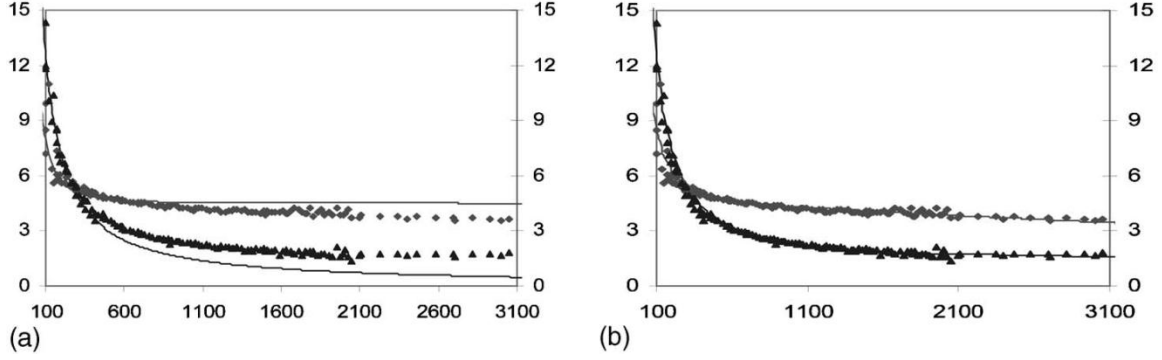


Figure 2.7 Complex permittivity at 20°C, where the real part (diamonds) is on the left axis and the imaginary part (triangles) is on the right axis. (a) Two and (b) three Debye extrapolation. (Reproduced from [5])

Ellison extends the fit to optical frequencies by taking the limit as the frequency tends to infinity. This limit is denoted in the paper as  $\varepsilon_\infty(t)$  such that  $\sqrt{\varepsilon_\infty}$  should be equal to the “optical” refractive index of the liquid. However, the difference between  $\varepsilon_\infty$  and  $n_D^2$  (refractive index at sodium D-line wavelength of 589.3nm) is really a measure of the probable existence of relaxation or resonance phenomenon between the fitted permittivity values and the optical frequencies. For a two-Debye relaxation fit, the author calculated values of  $\varepsilon_\infty(t)$  from 4.78 at 0°C to 4.27 at 30°C. For a three-Debye relaxation fit, the value of  $\varepsilon_\infty(t)$  varied from 2.94 to 2.48 over the range 0–30 °C. For a three relaxation and two resonant term fit, the calculated values of  $\varepsilon_\infty(t)$  vary from 1.7 to 1.5 over the range 0–30 °C. This final fit resulted in  $\sqrt{\varepsilon_\infty}$  values that are close to  $n_D = 1.333$ , but are still a little low.

## 2.2.2 Relations between complex permittivity, RI, and absorption

The previous section presented complex permittivity data up to 25 THz. At optical frequencies, dielectric materials are described by their complex refractive index (RI). Complex permittivity can be obtained from complex refractive index by the following:

$$\hat{\varepsilon} = \varepsilon_1 + i\varepsilon_2 = (n + i\kappa)^2 \quad (2.7)$$

where  $\varepsilon_1$  is the real part and  $\varepsilon_2$  is imaginary part of permittivity,  $n$  is the refractive index and  $\kappa$  is the extinction index. By equating the real and imaginary parts:

$$\varepsilon_1 = n^2 - \kappa^2 \quad (2.8)$$

$$\varepsilon_2 = 2n\kappa \quad (2.9)$$

The  $n$  and  $\kappa$  values have been found in terms of permittivity by Wooten [6]:

$$n = \sqrt{\frac{\sqrt{\varepsilon_1^2 + \varepsilon_2^2} + \varepsilon_1}{2}} \quad (2.10)$$

$$\kappa = \sqrt{\frac{\sqrt{\varepsilon_1^2 + \varepsilon_2^2} - \varepsilon_1}{2}} \quad (2.11)$$

Equations 2.10 and 2.11 can be validated by plugging them into Equations 2.8 and 2.9.

Absorption of electromagnetic waves in a dielectric material is related to the extinction index. The relation between absorption and the extinction index is nicely revealed by a plane wave (see Appendix A.3 for more details). The general form of a plane wave in one dimension is:

$$E(z, t) = E_0 e^{i(\hat{k}z - \omega t)} = E_0 e^{-(2\pi/\lambda)z\kappa} e^{i(kz - \omega t)} = E_0 e^{-\alpha_1 z} e^{i(kz - \omega t)} \quad (2.12)$$

where  $\omega$  is frequency,  $\lambda$  is wavelength, and  $\hat{k}$  is the complex wavenumber, which includes the complex refractive index and is given by  $\hat{k} = 2\pi(n + i\kappa)/\lambda$ . Therefore, the absorption coefficient in terms of the field and the extinction index is:  $\alpha_1 = (2\pi/\lambda)\kappa = (\omega/c)\kappa$  where  $c$  is the speed of light. However, absorption is often provided in terms of intensity, which is proportional to  $|E|^2$  such that:

$$\frac{I(z)}{I_0} = e^{-2\alpha_1 z} = e^{-\alpha_2 z} \quad (2.13)$$

As a result, the absorption coefficient in terms of intensity is  $\alpha_2 = 2\alpha_1 = (4\pi/\lambda)\kappa = 2(\omega/c)\kappa$ .

This intensity equation can be confused with the base 10 form sometimes used in the Beer-Lambert Law:

$$\frac{I(z)}{I_0} = 10^{-\xi Cz} = 10^{-\alpha_3 z} \quad (2.14)$$

where  $\xi$  is the molar absorption coefficient, and  $C$  is its concentration. The difference between the base 10 and base  $e$  form is found by equating Eq. 2.13 and 2.14, resulting in a scaling factor of  $\alpha_2 = \alpha_3 \ln(10) \approx 2.303\alpha_3$ .

### 2.2.3 Absorption spectrum of water with temperature dependence

The absorption of water at optical frequencies is a continuation of the dielectric spectroscopy of water, since absorption is related to complex permittivity. In general, water is absorbing at the ultraviolet wavelengths, then is transparent for visible wavelengths, and becomes absorbing in the infrared regions. One particular author has published the temperature dependence of the visible to near-infrared absorption spectrum of liquid water [7]. The wavelengths in the publication are over the range from 550nm to 900nm, and the temperature range is from ~15 to 60 °C.

Figure 2.8 is the resulting absorptivity reproduced from Langford *et al.* In Fig. 2.8(a), the absorption spectrum is seen to increase or decrease with temperature depending on the wavelength region. Lanford *et al.* defines absorption as using intensity of light with base 10, such that absorption is  $\alpha_3$  as seen in Eq. 2.14. Therefore, the base  $e$  spectrum is obtained by

multiplying Fig. 2.8(a) by a factor of 2.303. Figure 2.8(b) is a differential absorption spectrum, where the 25.2°C degree spectrum is subtracted and a correction for experimental drift is made.

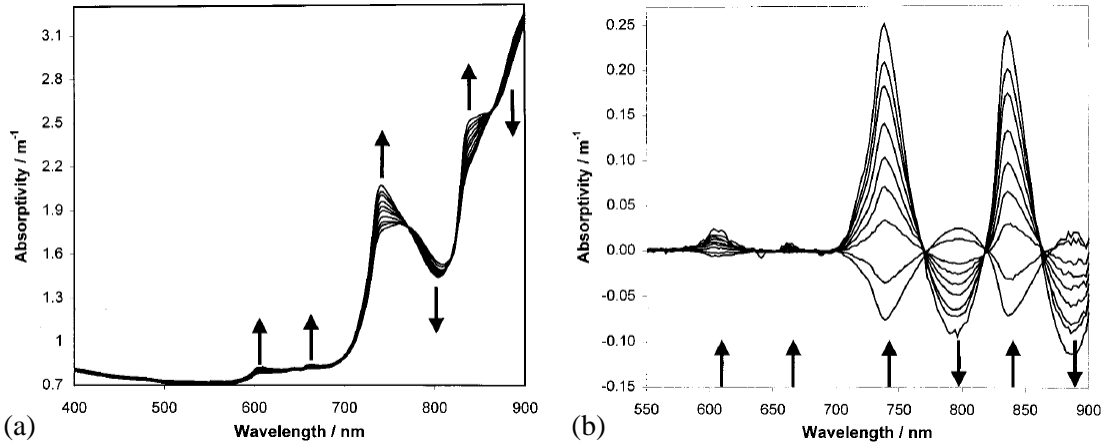


Figure 2.8 Absorption spectrum of water at different temperatures. The arrows indicate the direction of change with increasing temperature. (a) Absorption spectrum of water and (b) with the 25.2°C spectrum subtracted. (Reproduced from [7])

The data provided by Langford *et al.* makes it possible to check if absorption will affect our experimental results. Experiments could be influenced by the change in absorption with wavelength,  $d\alpha_2/d\lambda$ , or the change in absorption with temperature,  $d\alpha_2/dT$ . Our wavelength range provided by the LED is about 860nm to 940nm. This wavelength range is chosen because it is near the optical window of biological tissue and cells. Figure 2.9 illustrates the optical window is formed between the absorption of hemoglobin (<650nm) and water (>900nm). Since our wavelength range is beyond the data provided by Langford *et al.*, the linear assumptions of  $d\alpha_2/d\lambda$  is reliable up to 900nm and is assumed to continue the same slope up to 940nm. Another assumption is made that the greatest  $d\alpha_2/dT$  within our wavelength range occurs at 890nm. From Fig. 2.9, absorption changes from about  $2.5 \times 2.303 \text{m}^{-1}$  to  $3.15 \times 2.303 \text{m}^{-1}$  over the

40nm range, such that  $d\alpha_2/d\lambda = 0.0374\text{m}^{-1}\text{nm}^{-1}$ . From Fig. 2.8(b) at 890nm, absorption changes from  $0.00 \times 2.303\text{m}^{-1}$  to  $-0.12 \times 2.303\text{m}^{-1}$  over a  $34.8^\circ\text{C}$  range, so  $d\alpha_2/dT = -0.00794\text{m}^{-1}\text{C}^{-1}$ . The negative sign indicates that water becomes less absorbing as temperature increases.

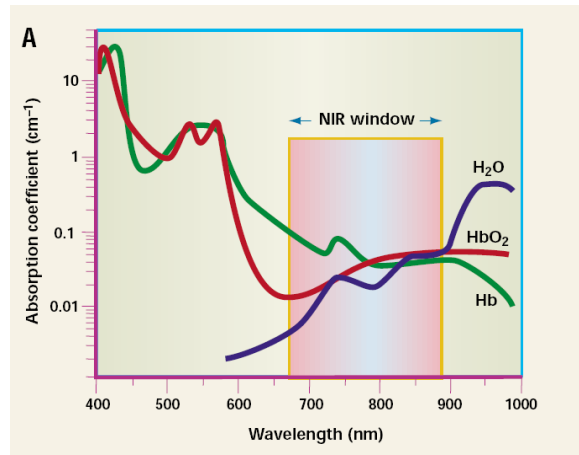


Figure 2.9 The water absorption spectrum in this figure is comparable to the water absorption provided by Langford *et al.* when Fig. 2.8(a) is scaled by 2.303. (Reproduced from [8])

The effects of  $d\alpha_2/d\lambda$  and  $d\alpha_2/dT$  on experimental results depends on whether the microfluidic channel is an optical cavity or does not have mirrors. In the latter case, the intensity of the light will be determined by Eq. 2.13. Calculations are presented in Table 2.2 with a typical cavity length of  $20\mu\text{m}$ .

Table 2.2 The first value is from Lanford *et al.* [7], who provides  $\alpha_3$  so it is multiplied by 2.303 to get  $\alpha_2$ . The second value for  $\alpha_2$  is found with the linear equation  $\alpha_2 = (\text{First value}) + m \times (\text{Difference between values})$ . The value  $I/I_0$  is from Eq. 2.13,  $\alpha_r$  is from Eq. 2.15, and  $\mathcal{F}$  is from Eq. 2.16.

	<b>Wavelength</b> @ Temperature = 25.2°C $d\alpha_2/d\lambda = m = 0.0374 \text{ m}^{-1}\text{nm}^{-1}$		<b>Temperature</b> @ Wavelength = 890nm $d\alpha_2/dT = m = -0.00794 \text{ m}^{-1}\text{°C}^{-1}$	
	<b>First value</b>	<b>Second value</b>	<b>First value</b>	<b>Second value</b>
	860nm	940nm	25.2°C	100°C
Difference between values	80nm		74.8°C	
$\alpha_2 = \alpha_s$	5.76 $\text{m}^{-1}$	8.75 $\text{m}^{-1}$	6.68 $\text{m}^{-1}$	6.09 $\text{m}^{-1}$
$I/I_0$ where $L = 20\mu\text{m}$	0.999885	0.999825	0.999866	0.999878
$\alpha_r$ where $L = 20\mu\text{m}$	2046.9 $\text{m}^{-1}$	2049.8 $\text{m}^{-1}$	2047.8 $\text{m}^{-1}$	2047.2 $\text{m}^{-1}$
$\mathcal{F}$ where $L = 20\mu\text{m}$	79.94	79.83	79.91	79.93
$\alpha_r$ where $L = 40\mu\text{m}$	1026.3 $\text{m}^{-1}$	1029.3 $\text{m}^{-1}$	1027.2 $\text{m}^{-1}$	1026.6 $\text{m}^{-1}$
$\mathcal{F}$ where $L = 40\mu\text{m}$	79.73	79.51	79.66	79.71

In both the wavelength and temperature dependent absorption cases, the change in light intensity is too small to be noticed because of the very small cavity length. If the microfluidic channel is an optical cavity, then absorption will change the finesse. The overall absorption of the cavity is given in Saleh and Teich [9]:

$$\alpha_r = \alpha_s + \frac{1}{2L} \ln \frac{1}{R_1 R_2} \quad (2.15)$$

where  $\alpha_s$  is the absorption coefficient of the medium,  $L$  is the cavity length,  $R_1$  and  $R_2$  are the reflectance of the two mirrors. The resulting finesse of the cavity is [9]:

$$\mathcal{F} = \frac{\pi \exp(\alpha_r L / 2)}{1 - \exp(-\alpha_r L)} \quad (2.16)$$

Calculations for Eq. 2.16 are also presented in Table 2.2, assuming mirror reflections of 0.96. The table demonstrates the second term in Eq. 2.15 dominates the overall absorption of the

cavity. Even though the length of the cavity is a significant variable, it ends up mostly canceled out in Eq. 2.16. Variation in finesse is negligible between the wavelength and temperature dependent absorption cases. Interestingly, the resulting finesse of about 80 with 96% reflecting mirrors agrees with Table 2.1, despite being different finesse equations.

One last possible way that absorption could affect our experimental results is by the complex refractive index. In an optical cavity, the phase difference between any two successive rays is given by  $\delta = 2kL\cos\theta$ , where the wavenumber  $k = 2\pi n/\lambda$ . A complex refractive index will result in a complex phase difference. This creates an imaginary term in Eq. 2.2 that is not measurable. The conclusion is made that absorption has little effect on the experimental results, whether the microfluidic channel is an optical cavity or does not have mirrors.

#### **2.2.4 Refractive index spectrum of water with temperature dependence**

The refractive index of water is also a continuation of the dielectric properties of water at optical frequencies. Unlike absorption, which is negligible as previously discussed, refractive index will strongly influence the transmission resonant wavelengths of the optical cavity. The refractive index of water is wavelength, temperature, and density dependent. Furthermore, the density of water is actually temperature dependent itself. These dependences will be explored and quantified.

A comprehensive collection of water and steam refractive index data was originally compiled and fit by Schiebener *et al.* [10]. The formulation by Schiebener *et al.* was based on the Lorentz-Lorentz function:

$$LL = \frac{n^2 - 1}{(n^2 + 2)\rho_m} \quad (2.17)$$

where  $n$  is the refractive index, and  $\rho_m$  is the molar density. This assumption was validated based on the existing data and was limited to a region between two water resonances. A revised version was later written by Harvey *et al.* [11]. One of the things Harvey *et al.* paid special attention to was the behavior of the refractive index in the near infrared, which is useful for this work. The formulation given by Harvey *et al.* is:

$$\frac{n^2 - 1}{n^2 + 2} \left( \frac{1}{\rho} \right) = a_0 + a_1 \bar{\rho} + a_2 \bar{T} + a_3 \bar{\lambda}^2 \bar{T} + a_4 / \bar{\lambda}^2 + \frac{a_5}{\bar{\lambda}^2 - \bar{\lambda}_{UV}^2} + \frac{a_6}{\bar{\lambda}^2 - \bar{\lambda}_{IR}^2} + a_7 \bar{\rho}^2 \quad (2.18)$$

where  $n$  is the refractive index,  $\bar{T}$  is temperature,  $\bar{\rho}$  is density, and  $\bar{\lambda}$  is wavelength. These are dimensionless variables and defined as:  $\bar{T} = T/T^*$ ,  $\bar{\rho} = \rho/\rho^*$ , and  $\bar{\lambda} = \lambda/\lambda^*$ , where the reference constants are  $T^* = 273.15\text{K}$ ,  $\rho^* = 1000\text{kg m}^{-3}$ , and  $\lambda^* = 0.589\mu\text{m}$ . The other coefficients are listed in Table 2.3. Rearranging Eq. 2.18 to isolate index of refraction provides:

$$n(\bar{\lambda}, \bar{T}, \bar{\rho}) = \sqrt{\frac{1 + 2RHS(\bar{\lambda}, \bar{T}, \bar{\rho})}{1 - RHS(\bar{\lambda}, \bar{T}, \bar{\rho})}} \quad (2.19)$$

where

$$RHS(\bar{\lambda}, \bar{T}, \bar{\rho}) = \bar{\rho} \left( a_0 + a_1 \bar{\rho} + a_2 \bar{T} + a_3 \bar{\lambda}^2 \bar{T} + a_4 / \bar{\lambda}^2 + \frac{a_5}{\bar{\lambda}^2 - \bar{\lambda}_{UV}^2} + \frac{a_6}{\bar{\lambda}^2 - \bar{\lambda}_{IR}^2} + a_7 \bar{\rho}^2 \right) \quad (2.20)$$

Equation 2.19 may sometimes be referred in this work as the NIST equation, since Harvey's affiliation is the National Institute of Standards and Technology.

Table 2.3 Coefficients for Eq. 2.17.

$a_0 = 0.244257733$	$a_4 = 1.58920570 \times 10^{-3}$
$a_1 = 9.74634476 \times 10^{-3}$	$a_5 = 2.45934259 \times 10^{-3}$
$a_2 = -3.73234996 \times 10^{-3}$	$a_6 = 0.900704920$
$a_3 = 2.68678472 \times 10^{-4}$	$a_7 = -1.66626219 \times 10^{-2}$
$\bar{\lambda}_{UV} = 0.2292020$	$\bar{\lambda}_{IR} = 5.432937$

The formulation by Harvey *et al.* is limited to certain ranges, and has estimated uncertainty values within those ranges. The formulation is endorsed by the International Association for the Properties of Water and Steam (IAPWS) for the following:

- Temperature  $-12^{\circ}\text{C} \leq t \leq 500^{\circ}\text{C}$
- Density  $0 \text{ kg m}^{-3} \leq \rho \leq 1060 \text{ kg m}^{-3}$
- Wavelength  $0.2 \text{ }\mu\text{m} \leq \lambda \leq 1.1 \text{ }\mu\text{m}$

A density close to zero implies the water has changed phase from a liquid to a vapor and there will be an abrupt change in refractive index. The user will provide the input density with some awareness that density changes significantly between phase boundaries. If the density of water is exactly zero, then Eq. 2.19 results in the vacuum refractive index of 1. The absolute uncertainty of refractive index in certain regions is reproduced in Fig 2.10. Our range of interest is the wavelength range of 0.7 to 1.1 $\mu\text{m}$ , which is only rated at the ambient temperature. The absolute uncertainty of refractive index in this case is  $1 \times 10^{-3}$ .

Wavelength ( $\mu\text{m}$ )	Temperature range ( $^{\circ}\text{C}$ )	Pressure range (MPa)	Phase	Absolute uncertainty of refractive index
0.40 to 0.70	-12 to 5	ambient	liquid	$< 6 \times 10^{-5}$
0.40 to 0.70	5 to 60	ambient	liquid	$1.5 \times 10^{-5}$
0.40 to 0.60	60 to 100	ambient	liquid	$< 3 \times 10^{-4}$
0.47 to 0.67	0 to 60	up to 150	liquid	$2 \times 10^{-4}$
0.63	100 to 225	0 to 2	vapor	$5 \times 10^{-6}$
0.70 to 1.1	ambient	ambient	liquid	$1 \times 10^{-3}$
0.21 to 0.40	0 to 100	ambient	liquid	$5 \times 10^{-4}$
In the following ranges there are no supporting data				
0.40 to 0.70	0 to 374	0 to $0.1 P_{\text{sat}}$	vapor	$5 \times 10^{-6}$
0.40 to 0.70	225 to 374	$0.1 P_{\text{sat}}$ to $P_{\text{sat}}$	vapor	$1 \times 10^{-4}$
0.40 to 0.70	60 to 374	$P_{\text{sat}}$ to 200	liquid	$1 \times 10^{-3}$
0.40 to 0.70	$> 374$	$< P(\rho_c/3)$	low density	$1 \times 10^{-5}$
0.40 to 0.70	$> 374$	$> P(\rho_c)$	high density	$2 \times 10^{-3}$

Figure 2.10 Estimated uncertainty of the refractive index formula. (Reproduced from [11])

Harvey *et al.* compares the formulation with experimental data to provide some sense of uncertainty at a wavelength of  $1.064\mu\text{m}$  and a temperature range of  $20^\circ\text{C}$  to  $60^\circ\text{C}$ . The experimental data was not used to make the formulation. Figure 2.11 reproduces the comparison, and it is shown the equation is consistent in the middle of the temperature range, but the higher and lower temperatures are in disagreement. Therefore, the author notes the estimated uncertainty in Fig. 2.10 may therefore be overly optimistic. A change in the fitting equation is likely required to accommodate the new data.

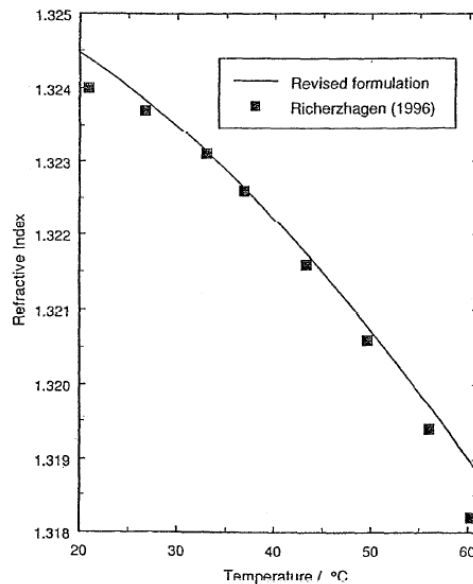


Figure 2.11 Temperature dependence of refractive index compared with data at  $1.064\mu\text{m}$ . (Reproduced from [11])

The formulation by Harvey *et al.* is also limited by the fact that density of water is difficult to calculate and is only well-established at discrete temperatures and pressures. A paper by Wagner *et al.* tabulates the density of water for different temperatures and pressures [12]. Figure 2.12 presents the tabulated data at pressures of  $0.05\text{MPa}$ ,  $0.1\text{MPa}$ , and at the standard atmospheric pressure of  $0.101325\text{MPa}$ . It can be observed from the figure that water has a maximum density around  $4^\circ\text{C}$ . In addition, the density at  $0.05\text{MPa}$  only goes up to  $81^\circ\text{C}$  as that

is the phase boundary between water and vapor. Two points can be made from this observation: (1) water does indeed have a lower boiling point at higher altitudes, and (2) an altitude of about 6,000m is needed to create an atmospheric pressure of 0.05MPa, which is close to the height of Mount McKinley, or the tallest mountain in North America.

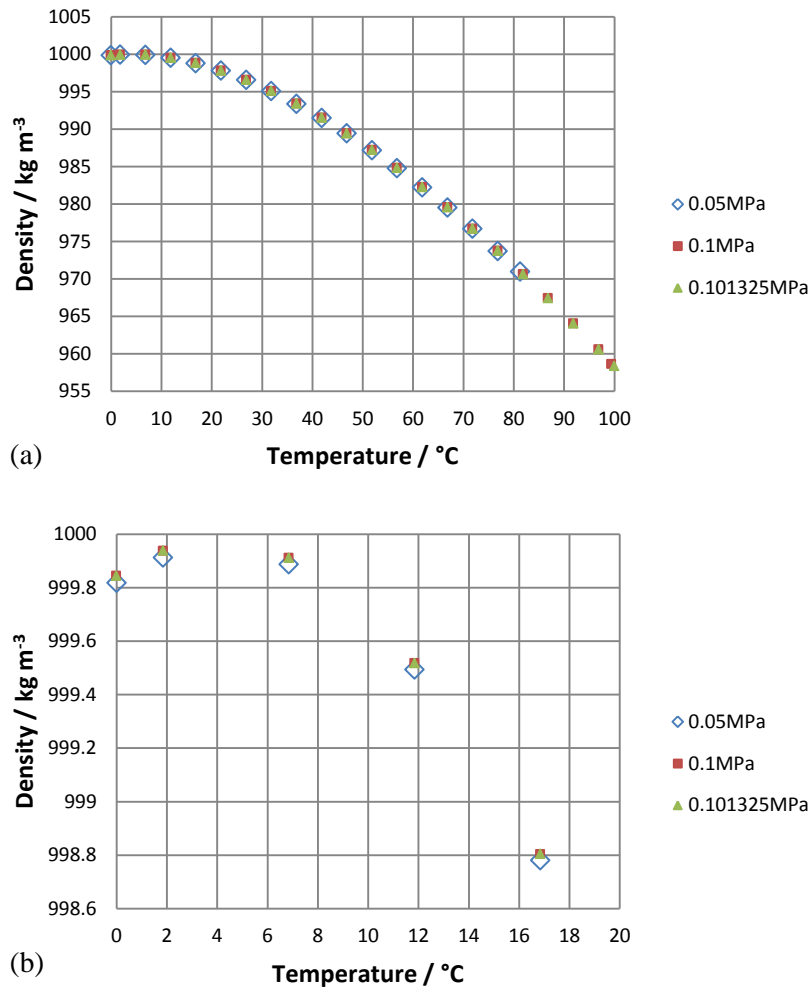


Figure 2.12 Density of water as a function of temperature at selected pressures from (a) 0°C to 100°C and (b) 0°C to 20°C. A maximum density is observed around 4°C.

The density of water at local atmospheric pressure is determined by taking a linear fit with pressure values of 0.05MPa, 0.1MPa, and 0.101325MPa. Even though density differences are very small between those pressures, this linear fit is intended to improve the accuracy of the

refractive index which has both squared and cubed density terms. Since the local atmospheric pressure is about 0.084MPa, a linear fit between 0.05MPa and 0.1MPa could have sufficed. However, it was desired to also include the standard atmospheric pressure as a fitting point. Linear fits are made at temperatures of 300K (26.85°C) to 325K (51.85°C) at 5K (5°C) increments as those were the tabulated increments. This temperature range is chosen because of the uncertainty at temperatures below 25°C and above 55°C as seen in Fig. 2.11. Table 2.4 presents the linear fits and the resulting density of water at 0.084MPa. A hidden assumption was made that the pressure in the microfluidic channel is the same as local atmospheric pressure.

Table 2.4 Linear fit:  $\rho(P) = aP + b$ . If the densities of 0.084MPa and 0.1MPa are rounded to the ones place, they will be identical.

<b>T / K</b>	<b>a / kg m<sup>-3</sup> MPa</b>	<b>b / kg m<sup>-3</sup></b>	<b>Density / kg m<sup>-3</sup> from linear fit at P = 0.084 MPa</b>	<b>Density / kg m<sup>-3</sup> from Wagner [X] at P = 0.1 MPa</b>
<b>300</b>	0.444275	996.511781	996.5491	996.556
<b>305</b>	0.444275	995.030781	995.0681	995.075
<b>310</b>	0.444275	993.338781	993.3761	993.383
<b>315</b>	0.434024	991.452306	991.4888	991.496
<b>320</b>	0.444275	989.381781	989.4191	989.426
<b>325</b>	0.434024	987.143306	987.1798	987.187

With the density of water determined at local atmospheric pressure and at selected temperatures, the refractive index can be calculated with Eq. 2.19. The refractive index as a function of temperature is presented in Fig. 2.13(a), and as a function of wavelength is seen in Fig. 2.13(b). The temperature and wavelength dependent refractive index have both been fit with quadratic and linear equations. Table 2.5 presents the fitting parameters for temperature dependence, where  $dn/dT = -1.4 \times 10^{-4}$  RIU °C<sup>-1</sup> averaged over wavelength. Table 2.6 presents the fitting parameters for wavelength dependence, where  $dn/d\lambda = -1.5 \times 10^{-5}$  RIU nm<sup>-1</sup> averaged over temperature.



Figure 2.13 Calculated refractive index from Eq. 2.19 as a function of (a) temperature with a secondary variable of wavelength, and (b) wavelength with a secondary variable of temperature.

Table 2.5 Quadratic and linear fits for the temperature dependent refractive index in Fig. 2.14(a). The quadratic fit is in the form  $n(T) = aT^2 + bT + c$ , and the linear fit is in the form  $n(T) = xT + y$ .

$\lambda$ / nm	a / RIU °C <sup>2</sup>	b / RIU °C	c / RIU	x / RIU °C	y / RIU
860	-1.2043E-6	-4.5345E-5	1.3290	-1.4012E-4	1.3308
880	-1.2029E-6	-4.5130E-5	1.3287	-1.3980E-4	1.3305
900	-1.2016E-6	-4.4912E-5	1.3284	-1.3948E-4	1.3302
920	-1.2003E-6	-4.4690E-5	1.3281	-1.3915E-4	1.3298
940	-1.1990E-6	-4.4464E-5	1.3278	-1.3883E-4	1.3295

Table 2.6 Quadratic and linear fits for the wavelength dependent refractive index in Fig. 2.14(b). The quadratic fit is in the form  $n(\lambda) = a\lambda^2 + b\lambda + c$ , and the linear fit is in the form  $n(\lambda) = x\lambda + y$ .

T / K	a / RIU nm <sup>2</sup>	b / RIU nm	c / RIU	x / RIU nm	y / RIU
300	5.1779E-9	-2.4840E-5	1.3445	-1.5520E-5	1.3403
305	5.1925E-9	-2.4792E-5	1.3438	-1.5446E-5	1.3396
310	5.2058E-9	-2.4738E-5	1.3431	-1.5368E-5	1.3389
315	5.2177E-9	-2.4679E-5	1.3424	-1.5287E-5	1.3382
320	5.2283E-9	-2.4613E-5	1.3416	-1.5203E-5	1.3373
325	5.2378E-9	-2.4543E-5	1.3407	-1.5115E-5	1.3364

### 2.2.5 High conductivity solutions at optical frequencies

The prior section presented the refractive index of pure water with temperature and wavelength dependence. Another solution in which the optical properties are useful is phosphate buffered saline (PBS). PBS is a high electrical conductivity solution often used in biomedical research because the osmolarity and ion concentration usually match those of the human body. Consequently, it is imperative to know the refractive index of PBS for any optical methods in

which it is utilized. Experiments later on in this work will report the refractive index of PBS with temperature and wavelength dependence.

The concentration of salts in phosphate buffered saline cause it to be an isotonic solution. Isotonic solutions are one of three types of tonicity classifications that arise when biological cells are immersed in an external solution. Figure 2.14 illustrates the three tonicity types with red blood cells. A hypertonic solution is one that has more impermeable solutes (e.g. salts) outside of the cell. In this case, water exits the cell to equalize the osmotic pressure, causing the cells to shrink. A hypotonic solution is one that contains a lesser concentration of solutes outside of the cell. For this case, water enters the cell to equalize the osmotic pressure, causing the cells to swell and possibly rupture. An isotonic solution means the solution has equal osmotic pressures.

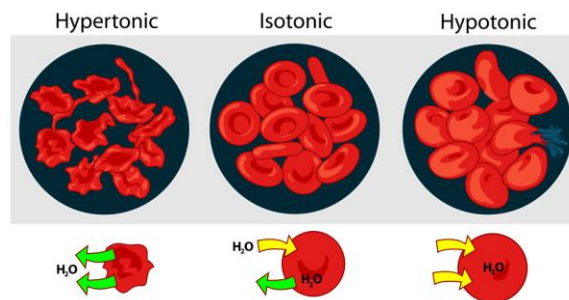


Figure 2.14 Classifications of tonicity and the effects on red blood cells. (Reproduced from [13])

A higher conductivity solution such as PBS may result in wave propagation in a good conductor. Criteria are used to tell if the material is a good conductor or good dielectric, which result in simpler approximations for wave propagation [14]. The parameters used for the criteria are conductivity  $\sigma$ , frequency  $\omega$ , and permittivity  $\epsilon$ . A good dielectric is satisfied by  $\sigma \ll \omega\epsilon$ , while a good conductor is given by  $\sigma \gg \omega\epsilon$ . There is also a possibility for a quasi-conductor that is within the range of  $1/100 \leq \sigma/(\omega\epsilon) \leq 100$ . However, the frequency dependence of conductivity and permittivity needs to be considered.

Pure water is first checked to see if it is a good dielectric with frequency dependence. The permittivity of water is known at room temperature and a frequency of 337THz to be  $\epsilon_r = n^2 = 1.326^2 \approx 1.76$ . The conductivity of water is related to the absorption of water given by [14]:

$$\alpha_1 = \omega \sqrt{\frac{\epsilon\mu}{2}} \left[ \sqrt{1 + \left(\frac{\sigma}{\omega\epsilon}\right)^2} - 1 \right]^{1/2} \quad (2.21)$$

where the absorption  $\alpha_1$  is defined in terms of field, frequency is  $\omega = 2\pi \times 337\text{THz}$ , permittivity is  $\epsilon = \epsilon_r \epsilon_0 = 1.76\epsilon_0$ , and permeability is  $\mu = \mu_0 = 4\pi \times 10^{-7} \text{H} \cdot \text{m}^{-1}$ . Rearranging Eq. 2.21 to solve for the conductivity:

$$\sigma = \omega\epsilon \sqrt{\left( \alpha_1^2 \left( \omega \sqrt{\frac{\epsilon\mu}{2}} \right)^{-2} + 1 \right)^2 - 1} \quad (2.22)$$

where the absorption at 890nm is seen from Fig. 2.8(a) and is given by  $\alpha_1 = (2.303 \times 2.9) / 2 = 3.34\text{m}^{-1}$ . The resulting conductivity is  $\sigma \approx 0.024\text{S} \cdot \text{m}^{-1}$ . Therefore,  $\omega\epsilon = 3.3 \times 10^4 \gg 0.024$  and the criterion for a good dielectric is met.

PBS is now checked to see if it is a good dielectric with frequency dependence. The conductivity of PBS is  $1.25 \text{S} \cdot \text{m}^{-1}$  [15] but this is at lower frequencies and the conductivity at optical frequencies needs to be known. An order of magnitude value can be found by assuming PBS is like seawater, as the optical properties of seawater are more well-known. Seawater will actual provide an upper limit because the electrostatic conductivity is much larger at  $4.8 \text{S} \cdot \text{m}^{-1}$  [16]. The absorption coefficient of seawater is the same as pure water from 750nm to 800nm [17]. Consequently, the conductivity of water and seawater will be within an order of magnitude

as observed in Eq. 2.21 if permittivity does not change by an order of magnitude. It is induced that if water is a good dielectric at 890nm, then so is seawater, and so is PBS.

Since PBS is a good dielectric material, its refractive index is important to know for any optical method in biomedical research. Earlier work has been done by Aly and Esmail [18] who measured the refractive index of water with dependencies on temperature and sodium chloride concentrations. Sodium chloride is one of the main salts in PBS, such that knowing the work by Aly and Esmail is useful. The wavelength implemented by Aly and Esmail was 632.8nm using a HeNe laser. At 300K and a sodium chloride concentration of zero, their refractive index was close to 1.334. Using Eq. 2.19 at the same wavelength and temperature, and at a density corresponding to standard atmospheric pressure, the refractive index is 1.3314 with an estimated uncertainty of  $1.5 \times 10^{-5}$ . Aly and Esmail disagree with the NIST equation by  $2.6 \times 10^{-3}$  RIU which is greater than the uncertainty. However, the corresponding 0.2% difference suggests that other data values by Aly and Esmail are reliable.

Figure 2.15 reproduces the refractive index data from Aly and Esmail with temperature and concentration dependence. The concentration of sodium chloride in PBS is 0.137 molar, which is about  $2/10^{\text{th}}$  of the distance between the NaCl concentrations of 0 and 0.855 molar. This corresponds to an increase in refractive index of 0.002 RIU. Consequently, the refractive index experiments in this work should expect an increase of about 0.002RIU from water to PBS, assuming the change in refractive index is similar around 890nm. The reason why refractive index increases with NaCl concentration is explained by Aly and Esmail in terms of the Lorentz-Lorentz formula. As density increases with salt, the refractive index also increases. A quick check confirms the density hypothesis: the density of water at room temperature is  $1000\text{kg m}^{-3}$ , and the density of seawater is  $1030\text{kg m}^{-3}$ .

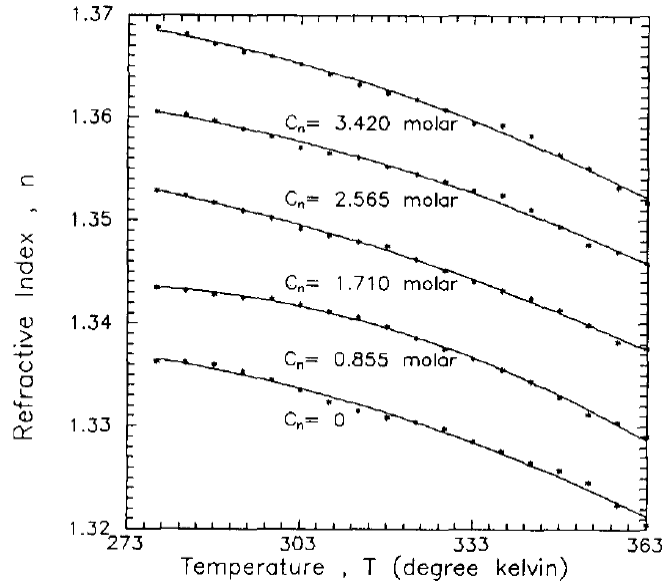


Figure 2.15 Temperature dependence of refractive index for various NaCl concentrations. (Reproduced from [18])

## 2.3 Single-cell manipulation and analysis with electric fields

As mentioned in the beginning of the chapter, the project originally started out using the microfluidic channel as a Fabry-Pérot interferometer to distinguish individual healthy and cancerous biological cells. These cells were manipulated in the microfluidic channel with dielectrophoretic forces, which is a phenomenon that occurs when cells are in the presence of electric fields. One of the concerns with using electric fields is the potential for cell permeabilization and the decrease in cell viability. Electric fields can also be utilized to analyze the dielectric properties of the cell, which have distinguishing characteristics.

### 2.3.1 Dielectrophoresis and electro-rotation

Two types of electrokinetic phenomena that can arise when a dielectric particle is in the presence of an electric field are dielectrophoresis and electro-rotation. Biological cells have dielectric properties [19] such that they can act as dielectric particles, and the cells can be exposed to electric fields by placing electrodes in a microfluidic channel. Dielectrophoresis is

often used to oppose the drag force on cell and manipulate the cell's position. However, cell discrimination can also be achieved by either dielectrophoresis or electro-rotation.

If water or a water-based solution is in the microfluidic channel, then one needs to be careful of electrolysis. Electrolysis is the decomposition of water (H<sub>2</sub>O) into oxygen (O<sub>2</sub>) and hydrogen gas (H<sub>2</sub>) due to an electric current. At the negatively charge electrode, a reduction reaction occurs to form the hydrogen gas. At the positively charged electrode, an oxidation reaction takes place to generated oxygen gas. Electrolysis can be avoided by using alternating current (AC) electric fields. The frequency necessary to avoid electrolysis is determined experimentally and has been found to be in the 10-50MHz range.

Dielectrophoresis (DEP) is the movement of particles in non-uniform fields, and is illustrated in Fig. 2.16. A particle subjected to an electric field will result in the induction of a dipole. If the electric field is nonuniform, its strength on one side of the particle is larger than on the other, resulting in a force on the particle known as the dielectrophoretic force. The time-average magnitude of this force depends on the gradient of the electric field as seen by:

$$\langle F_{DEP} \rangle = 2\pi R^3 \varepsilon_m \text{Re}[CM] |\nabla |\mathbf{E}_{rms}|^2| \quad (2.23)$$

where  $R$  is the radius of the particle,  $\varepsilon_m$  is the permittivity of the medium,  $CM$  is the frequency dependent Clausius-Mossotti (CM) factor,  $\text{Re}$  indicates the real part, and  $\mathbf{E}_{rms}$  is the root-mean-square value of the alternating electric field. The CM factor is similar to the Lorentz-Lorentz equation:

$$CM = \frac{\varepsilon_p^* - \varepsilon_m^*}{\varepsilon_p^* + 2\varepsilon_m^*} \quad (2.24)$$

where  $\varepsilon_p^*$  and  $\varepsilon_m^*$  are the respective complex permittivities of the particle and the medium.

Complex permittivity is in the form:  $\varepsilon^* = \varepsilon + j\sigma/\omega$ , where  $j = \sqrt{-1}$ ,  $\omega$  is electrical frequency, and  $\sigma$  is the conductivity of the medium.

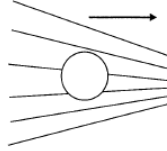


Figure 2.16 Illustration of dielectrophoresis, resulting from a particle in a non-uniform field. (Reproduced from [19])

Electro-rotation is the rotation of particles in a rotating electric field, and is illustrated in Fig. 2.17 (a) and (b). The rotating electric fields can be generated by applying phase-shifted electric fields to electrodes surrounding a particle. Even though electro-rotation can also be observed in nonrotating electric fields, the term is generally used for rotating fields. A particle subjected to a rotating electric field results in a torque exerted on it because of the phase difference between the applied electric field and the induced dipole. The magnitude of the torque is given by:

$$\Gamma = -4\pi\varepsilon_m R^3 \text{Im}[CM]E^2 \quad (2.25)$$

where  $CM$  is again the frequency dependent Clausius-Mossotti factor, and **Im** indicates the imaginary part. When the particle rotates in a viscous liquid, the surrounding fluid exerts a hydrodynamic drag force on the particle. The resulting rotation rate depends on the equilibrium between the drag force and the electro-rotation torque and is provided by:

$$\Omega(\omega) = \frac{\varepsilon_m}{2\eta} \text{Im}[CM]E^2 \quad (2.26)$$

where  $\eta$  is the viscosity of the fluid.

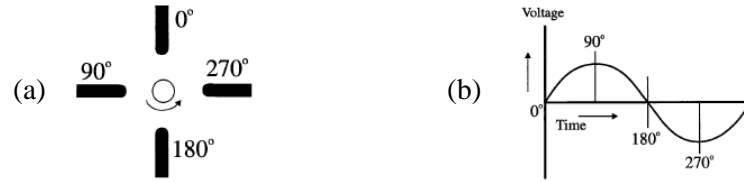


Figure 2.17 Illustration of (a) electro-rotation, and (b) the phase of the rotating electric field. (Reproduced from [19])

The Clausius-Mossotti factor is frequency-dependent and has a spectral response. Figure 2.18(a) illustrates the general spectra of the CM factor for both the real and imaginary parts. The real part of the CM factor can be either negative or positive, such that the direction of the DEP force is either positive (pDEP) or negative (nDEP). A negative DEP force will move the particle away from higher electric fields. This is preferred in our case as it pushes the biological cell away from the opaque electrodes and the larger electric field magnitude. Figure 2.18(b) shows the real part of the CM factor at various external medium conductivities. Our medium used for biological cells is phosphate buffered saline with a conductivity around  $1.25 \text{ S m}^{-1}$ . Thus, the DEP force remains negative for the frequency range that avoids electrolysis. At frequencies above  $\sim 50\text{MHz}$ , the CM factor can be approximated as [20]:  $CM \approx (\epsilon_p - \epsilon_m) / (\epsilon_p + 2\epsilon_m)$ .

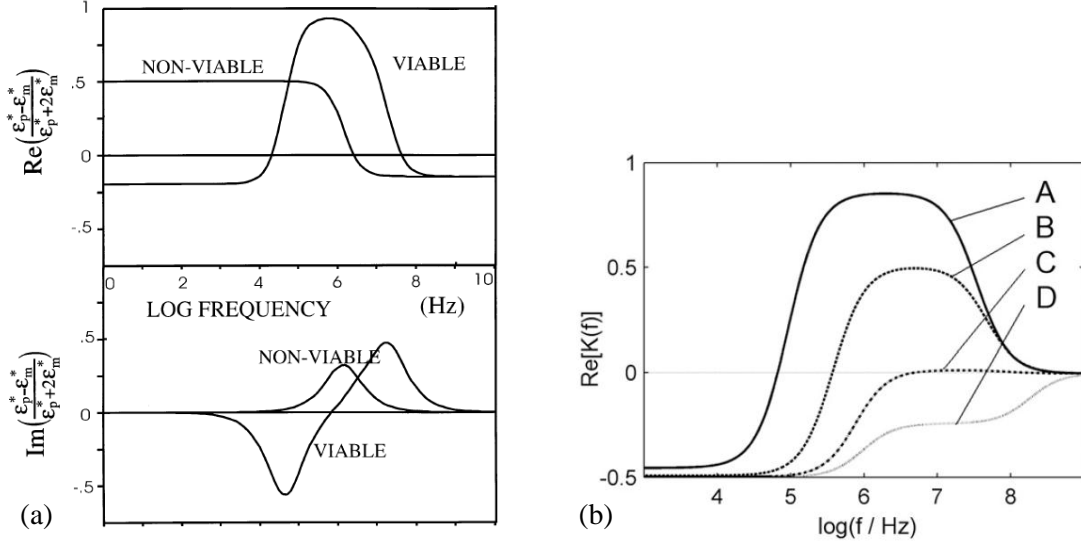


Figure 2.18 (a) Spectrum of real and imaginary parts of the CM factor. (Reproduced from [19]) (b) The real part of the CM factor at medium conductivities of A:  $0.0175 \text{ S m}^{-1}$ ; B:  $0.1 \text{ S m}^{-1}$ ; C:  $0.4 \text{ S m}^{-1}$ ; D:  $1.0 \text{ S m}^{-1}$ . (Reproduced from [21])

### 2.3.2 Electroporation of cells

Electroporation, or electro-permeabilization, occurs when biological cells are subjected to some critical electric field strength and become transiently permeabilized. This results in the ability to introduce exogenous DNAs and other macro-molecules into the cells [22]. Electroporation is a dynamic process that depends on the local transmembrane potential. A transmembrane potential is induced in a cell by the external field, generally described by the equation [23]:

$$V_m = fE_{ext}r \cos \Phi \quad (2.27)$$

where  $V_m$  is the transmembrane potential,  $f$  is a form factor describing the impact of the cell,  $E_{ext}$  is the applied electric field,  $r$  is the cell radius, and  $\Phi$  is the polar angle with respect to the electric field. The value for the factor  $f$  is often listed as 1.5, but this factor depends on a number of different factors.

Electroporation occurs when the induced membrane potential  $V_m$  superimposed on the resting membrane potential is larger than a threshold potential. The threshold potential is on the order of 200mV to 1V, which is a common range as the bilayer membrane is a common feature for eucaryotic cells. Permeabilization will initially happen at the pole of the cell facing the positive electrode. This is because the resting transmembrane potential is negative on the inside of the cell with respect to the outside, such that the superimposed potential is larger. Permeabilization then occurs at the pole of the cell facing the negative electrode. The pore formation happens in the microsecond time frame, whereas membrane sealing happens over a range of minutes.

Figure 2.19 demonstrates the pore formation caused by electro-permeabilization. It has been shown that the area of the membrane being permeabilized is larger on the pole facing the positive electrode, but the degree of permeabilization is larger towards the negative electrode, allowing larger molecules to diffuse into the cell. The waveform type will also influence how the cell is permeabilized. Waveform types that have been studied are unipolar square waves, bipolar square waves, and a single square pulse [22]. Figure 2.20 presents selected video frames of electro-permeabilized cells in which ethidium bromide was used as a permeabilization-indicator probe. In this figure, the positive electrode is at the bottom and the negative electrode is at the top of each image. Thus, the electro-permeabilization images are consistent between Fig. 2.19 and 2.20.

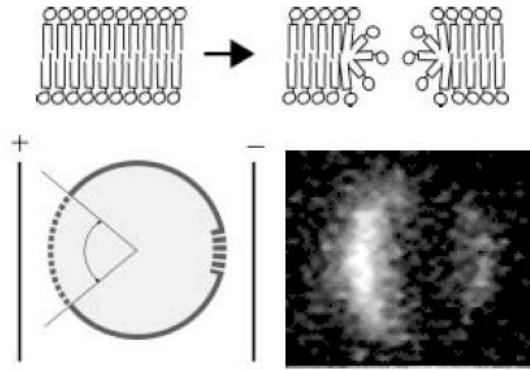


Figure 2.19 Top panel: Electroporation occurs when an electric field is applied and the induced potential exceeds the capacity of the membrane. This results in transient hydrophilic pores that allow DNA and larger molecules into the cell. Bottom left: Since the resting transmembrane potential is negative on the inside respective to the outside, the membrane facing the positive electrode will be first permeabilized. Bottom right: Image of a CHO cell suspended in a medium being permeabilized. The positive electrode is on the left and negative electrode on the right. (Reproduced from [23])

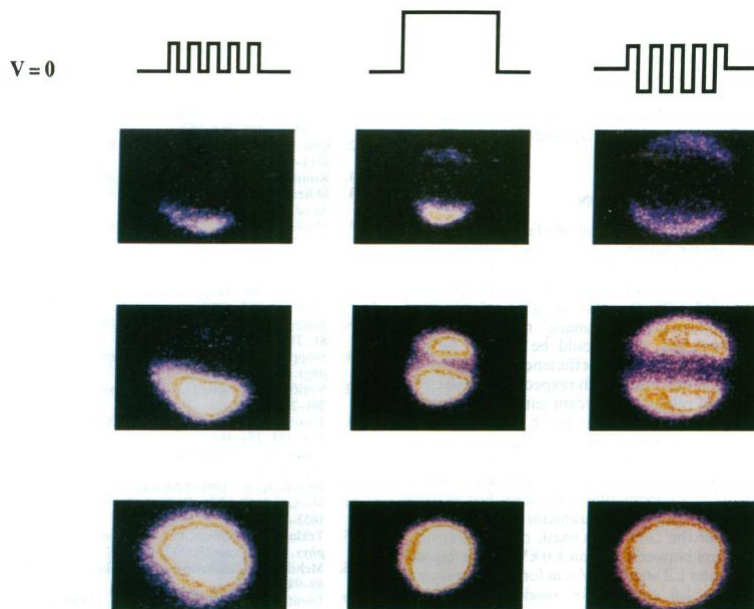


Figure 2.20 Selected video frames of electro-permeabilized cells exposed to various waveforms. Time increases from top to bottom. The pulse duration was  $400\mu\text{s}$ , and frequency was  $250\text{kHz}$  for the unipolar and bipolar square waves. *Left*: unipolar square wave;  $1.10\text{kV/cm}$ , frames at  $0.528$ ,  $2.739$ , and  $8.745\text{s}$ . *Middle*: single square pulse;  $4.95\text{kV/cm}$ , frames at  $0.297$ ,  $1.419$ , and  $8.943\text{s}$ . *Right*: Bipolar square wave;  $2.25\text{kV/cm}$  (peak-to-peak), frames at  $0.132$ ,  $0.891$ , and  $3.267\text{s}$ . (Reproduced from [22])

If an AC waveform is applied, the induced transmembrane potential is strongly dependent on the frequency. The maximum membrane potential induced by an RF field is [24, 25]:

$$V_m = \frac{3rE \cos \Phi}{2[1 + (\omega\tau)^2]^{1/2}} \quad (2.28)$$

where the additional terms as compared to Eq. 2.27 is the frequency  $\omega$  and the relaxation time of the cell  $\tau$ . A form factor of 1.5 has been assumed. The relaxation time is given by  $\tau = rC_m(\rho_i + 0.5\rho_e)$ , where  $r$  is the radius of the cell,  $C_m$  (in F m<sup>-2</sup>) is the capacitance of the membrane,  $\rho_i$  (in  $\Omega$  m) is the resistivity of the interior of the cell, and  $\rho_e$  (in  $\Omega$  m) is the resistivity of the electrolyte. The time constant is usually in the range of 0.1 to 1  $\mu$ s. Eq. 2.28 will reduce to Eq. 2.27 when  $\omega = 0$ , and the induced transmembrane potential will decrease with increasing frequency.

A simple electrical circuit model can be made to help determine the transmembrane potential with frequency dependence for a cell suspended in a lossy medium. Membranes are modeled as capacitors, and conductive fluids are modeled as resistors. The model can include or neglect the nucleus membrane. In general, the electrical pulses do not affect the intracellular membranes because the outer membrane shields the interior of the cell. Figure 2.21(a) presents an electrical model of a cell suspended in a medium and also includes the nucleus. The frequency response is seen in Fig. 2.21(b), and it is observed that higher frequencies lower the induced transmembrane potential.

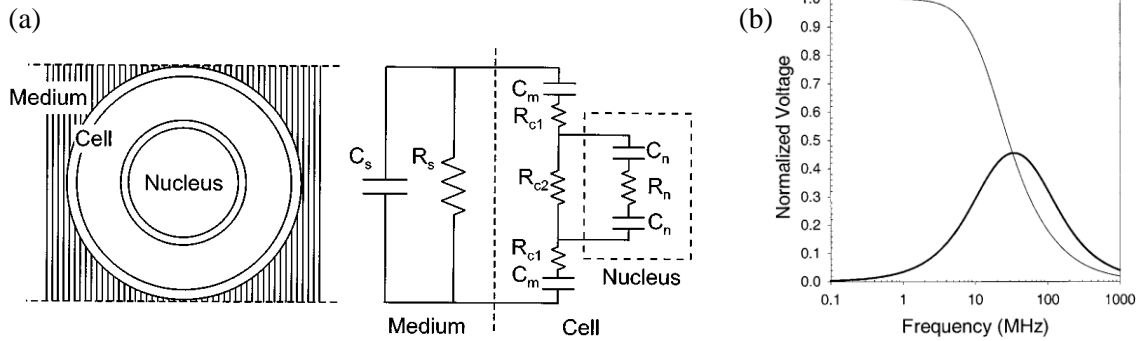


Figure 2.21 (a) A simplified biological cell in a medium and the corresponding electrical circuit. (b) Normalized voltages across the outer membrane (thin line) and the nuclear membrane (bold line) versus frequency for given electrical parameters in the paper. (Reproduced from [26])

Electroporation presents viability concerns for the biological cells. If the induced membrane potential is excessively large in magnitude or pulse duration, the membrane will not reseal, leading to cell death. This is also known as irreversible electroporation. Tekle *et al.* [22] presents a nice table with experimental parameters including the electric field magnitude, waveform type, frequency, pulse duration, and the resulting cell viability percentage. The table is partially reproduced in Fig. 2.22. One should note that Tekle *et al.* used square-wave AC fields whereas this work exclusively implements sinusoidal fields. A correction factor between the root-mean-square of square-waves and sinusoid, could make comparison possible. The parameters closest to our work are a bipolar square wave (BSW) with an electric field of 0.4 to 4.0 kV cm<sup>-1</sup> (in terms of peak-to-peak for BSW) and a frequency of 1000kHz. As seen in the table, viability for the BSW drops quickly with increasing electric field strength or increasing pulse duration.

Electric field,* kV/cm	Frequency,† kHz	Pulse duration, μs	Survival, %		
			BSW	USW	SSP
0.4	60	400	97	95	95
0.8	60	400	93	95	81
1.2	60	400	93	77	43
1.6	60	400	89	59	27
2.2	60	400	62	25	17
3.0	60	400	44	11	7
4.0	60	400	19	3	<1
1.6	60	400			
1.6	60	400			
1.6	60	400			
1.6	60	1000	81	53	26
1.6	60	5000	41	28	21
1.6	250	400	93	68	
1.6	1000‡	400	92	78	
0	0	0	96	96	98
1.6	60	400	86	61	38
0	0	0	95	98	96

Figure 2.22 Cell viability as a result of different electrical parameters. (Reproduced from [22])

### 2.3.3 Double-layer capacitance

The previous section worked up to a simple circuit model to determine the transmembrane potential in a lossy medium. The model did not include the double-layer capacitance often associated with an electrode/electrolyte interface. This capacitance can be neglected at higher frequencies, but it is wise to quantify if the capacitance is negligible for our work. The characteristic thickness of the double-layer is the Debye length, given by [27]:

$$\lambda_D = \frac{1}{\sqrt{8\pi l_B N_A I}} \quad (2.29)$$

where  $I$  is the ionic strength,  $N_A$  is Avagadro's number, and  $l_B$  is the Bjerrum length. The ionic strength of the PBS needs to be calculated with all of the ions using the following [27]:

$$I = \frac{1}{2} \sum_{i=1}^n c_i z_i^2 \quad (2.30)$$

where  $c_i$  is the molar concentration of the ion, and  $z_i$  is the charge number of that ion. For a 1:1 electrolyte such as sodium chloride, the ionic strength is equal to the concentration. Using Eq. 2.30 and the ion concentration of 1X PBS (Appendix E), the ionic strength is  $171.46 \text{ mol m}^{-3}$ . The Bjerrum length is given by [27, 28]:

$$l_B = \frac{e^2}{4\pi\epsilon k_B T} \quad (2.31)$$

where  $e$  is the elementary charge, permittivity is  $\epsilon = \epsilon_0 \epsilon_r$ , thermal energy is  $k_B T$ , where  $k_B$  is the Boltzmann constant and  $T$  is temperature in Kelvin. The resulting double-layer capacitance is defined as:

$$\frac{C_{dl}}{A} = \frac{\epsilon}{d} = \frac{\epsilon_0 \epsilon_r}{\lambda_D} \quad (2.32)$$

The Bjerrum length, Debye length, and capacitance per unit area are calculated in Table 2.7 for the fixed 1X PBS concentration and over our temperature range from 20°C to 100°C. The room temperature (300K) Debye length of 0.7nm is consistent with noted values in the literature [29, 30]. Furthermore, the impedance magnitude of the double-layer capacitance is calculated assuming a rectangular electrode surface area of  $30\mu\text{m} \times 400\mu\text{m}$  and a frequency of 50MHz. As seen in the table, the double-layer electrical impedance remains negligible over the range of temperatures.

Table 2.7 Calculated double-layer impedance across a temperature range from 20-100°C.

<b>T (K)</b>	<b><math>k_B T</math> (eV)</b>	<b><math>l_B</math> (nm)</b> From Eq. 2.31 where $\epsilon_r = 80$	<b><math>\lambda_D</math> (nm)</b> From Eq. 2.29	<b><math>C_{dl} / A</math> (F m<sup>-2</sup>)</b> From Eq. 2.32 where $\epsilon_r = 80$	<b><math> Z_{dl} </math> (ohm)</b> $A = 30\mu\text{m} \times 400\mu\text{m}$ $\omega = 2\pi \times 50\text{MHz}$
<b>293</b>	2.52E-2	0.715	0.734	0.965	0.275
<b>300</b>	2.59E-2	0.695	0.745	0.950	0.279
<b>303</b>	2.61E-2	0.690	0.747	0.948	0.280
<b>313</b>	2.70E-2	0.667	0.760	0.932	0.285
<b>323</b>	2.78E-2	0.648	0.771	0.918	0.289
<b>333</b>	2.87E-2	0.627	0.784	0.903	0.294
<b>343</b>	2.96E-2	0.608	0.796	0.889	0.298
<b>353</b>	3.04E-2	0.592	0.807	0.877	0.302
<b>363</b>	3.13E-2	0.575	0.819	0.864	0.307
<b>373</b>	3.21E-2	0.561	0.829	0.854	0.311

### 2.3.4 Impedance spectroscopy

Impedance spectroscopy measures the AC electrical properties of particles in suspension, such that the dielectric parameters can be obtained. Notable authors include Gawad *et al* [31, 32, 33] as well as reviews by Sun and Morgan [34] and Cheung *et al.* [35]. The impedance of biological cells has a spectral response. At low frequencies, the cell membrane blocks current flow and the impedance amplitude will provide the cell size. At intermediate frequencies, impedance measurements give information about the membrane properties. At high frequencies, the membranes have little effect and measurements here give information about intracellular structures and the cell interior. There is a possibility for an invalid measurement if there are two cells being measured. However, one author [31] claims that the “probability of having two cells simultaneously in the sensing area is remote as it has a small volume (~30 pl) compared to the cell density in the prepared solution (~1/600 pl<sup>-1</sup>).”

Impedance spectroscopy offers several advantages in single-cell analysis. An opacity measurement can be made, which is the ratio of the impedance magnitude at a high frequency to a low frequency. This helps to normalize the data for both cell size and cell position between the measurement electrodes in the microfluidic channel. However, at frequencies below 100 kHz, the signal value is non-linear to the cell volume because of the double-layer [32]. The double-layer was presented in the earlier and is not desirable as it will affect the normalization. A further advantage is the on-the-fly measurement, which allows a short exposure time to the potentially lethal electric field and provides a relatively higher throughput. In addition, cell manipulation by dielectrophoresis can easily be added to this system for focusing or sorting.

A differential method has been implemented by adding a second pair of electrodes. This is preferred because [31]:

- The cell's properties can be measured directly against its surrounding media.
- Any uneven drift of the electrode properties can be sensed and corrected, as both signal maxima should be the same amplitude.
- The speed of the particle can be determined, as the distance and transit time between electrodes are known.

The differential measurement can be realized on both planar and 3D electrode configurations.

The 3D electrode structure is seen in Fig. 2.23.

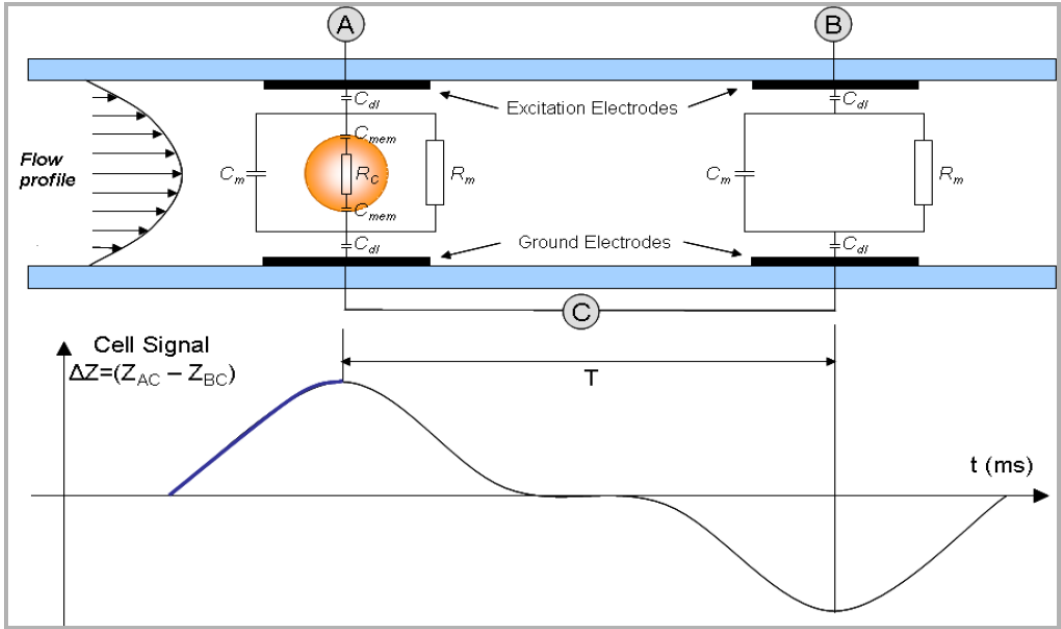


Figure 2.23 Schematic of a differential impedance measurement on a biological cell. The double-layer capacitance has been included. (Reproduced from [36])

## 2.4 Literature review of joule heating in microfluidic systems

The combination of a high conductivity solution and high magnitude electric fields may result in joule heating. A high conductivity solution is necessary for biological cells, because the osmolarity and ion concentration usually match those of the human body. High magnitude electric fields are often used for cell manipulation in a microfluidic channel. In the case where dielectrophoresis is utilized, the electric field needs to be high enough to create a field gradient that opposes the drag force on the cell. Temperature rises caused by joule heating can be fatal to biological cells depending on the time of exposure and peak temperature [37]. A temperature rise can also be helpful in resealing membranes after electroporation [23]. Consequently, it is useful to quantify the temperature rises induced by joule heating in microfluidic systems.

### 2.4.1 Ross *et al.*, 2001

In the work by Ross *et al.* [38], temperatures rises are measured using temperature-dependent fluorescence and imaging. Rhodamine B was chosen as the fluorescent dye because it is readily available and is known to have a quantum yield that is strongly temperature dependent in the range between 0 and 100°C. First, a calibration curve was generated to accurately measure the relationship between fluorescence and temperature, and is reproduced in Fig. 2.24. After the calibration curve has been determined, it can be used to measure the temperature of the solution in the microfluidic channel by comparing to the fluorescence intensity at room temperature (22°C). Joule heating was caused by a DC voltage and a carbonate buffer with a concentration of 20mM.

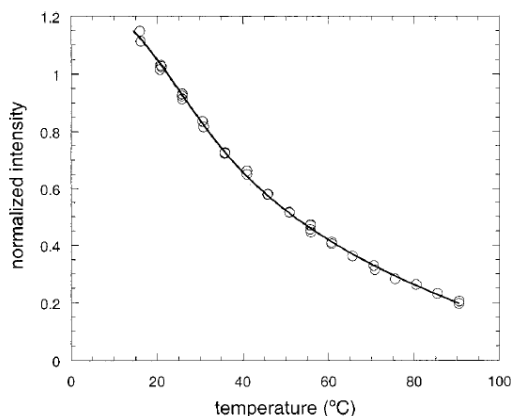


Figure 2.24 Calibration curve for Rhodamine B normalized at room temperature (22°C). The solid line is a third-order polynomial fit. (Reproduced from [38])

The fluorescence intensity is imaged using a standard fluorescence microscope and CCD camera. An appropriate filter set was used (excitation, 500-550nm; emission, >565nm). The spatial resolution is claimed to only be limited by the microscope optics. In the work by Ross *et al.*, a 0.32 numerical aperture objective was used, resulting in a spatial resolution of 1 $\mu$ m. This value was checked with the diffraction limit equation (Appendix B) and an emission wavelength

of 585nm, such that the spatial resolution is indeed close to 1 $\mu$ m. One should note the diffraction limit is the ideal limit of the microscope. The temporal resolution is determined by the video frame rate of the camera, resulting in a resolution of 33ms.

There are a few trade-offs using the temperature-dependent fluorescent dye method for thermometry. One drawback claimed by the authors is that it deduces temperatures by comparing the fluorescence intensity of images at unknown temperatures with only one reference image: room temperature. This introduces the possibility of large systematic uncertainties, especially at temperatures far from the reference temperature. However, the advantages gained from the speed and ease of implementation can outweigh the disadvantage of increased uncertainty. Another drawback is that Rhodamine B can be toxic to biological cells. It has been shown the relative plating efficiencies, or cloning efficiencies, is greatly reduced at a Rhodamine B concentration of 15  $\mu$ g/mL ( $\sim$ 30 $\mu$ M) or higher [39]. The concentration of Rhodamine B used by Ross *et al.* is  $\sim$ 100 $\mu$ M, such that it would be toxic to cells. The toxicity problem can be avoided by taking temperature measurements outside of cell experiments. This prevents real-time thermometry with cells, which may or may not be okay.

#### **2.4.2 Seger-Sauli *et al.*, 2005**

Seger-Sauli *et al.* [15] measures temperature rises induced from joule heating specifically by negative DEP electrodes. Two methods are used for measurements: (1) thermo-dependent fluorescent dye Rhodamine B, and (2) water-soluble polymers with thermo-precipitating properties are used to detect temperature thresholds. The author also derives an equation to estimate the temperature rise for a given electrode geometry and electric field. However, the equation is ambiguous regarding how it includes both the thermal conductivity of the PBS and glass.

The first method utilizes the temperature-dependent fluorescent dye Rhodamine B and a fluorescence microscope. Rhodamine B is quoted in this work to have an excitation wavelength of 560nm, and an emission wavelength of 585nm. A 1mM concentration of Rhodamine B was prepared in a PBS buffer. This concentration is toxic to cells, according to Gupta and Dudani [39] who presented the cloning efficiency of cells is greatly reduced for Rhodamine B concentrations of 30 $\mu$ M or more.

A calibration curve of intensity versus temperature was assessed in the microfluidic chip itself by placing the chip in an airtight hood and increasing the air temperature. This curve was fit with an exponential function, unlike Ross *et al.* who used a third-order polynomial. Figure 2.25 reproduces fluorescence intensity images with the delectrophoresis electrodes both off and energized. The applied signals were sinusoidal at 1MHz, electrodes were 8 $\mu$ m wide, and the channel height separating the electrodes was 20 $\mu$ m. Figure 2.26 is the fluorescence intensities for various applied voltages as well as the resulting temperature distribution obtained from the calibration curve.

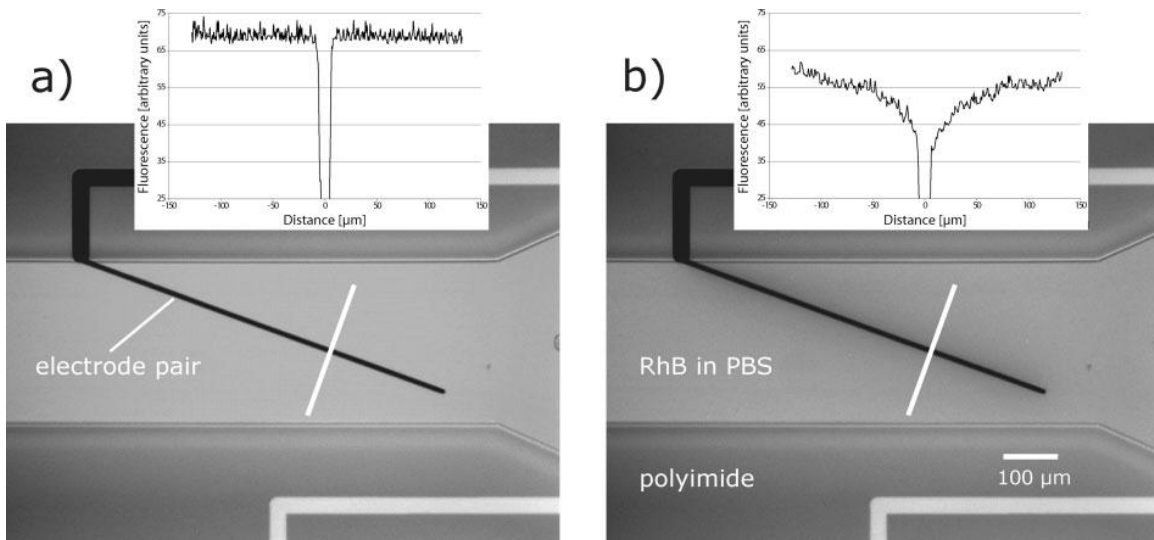


Figure 2.25 Image and fluorescence intensities with electrodes (a) off and (b) energized. (Reproduced from [15])

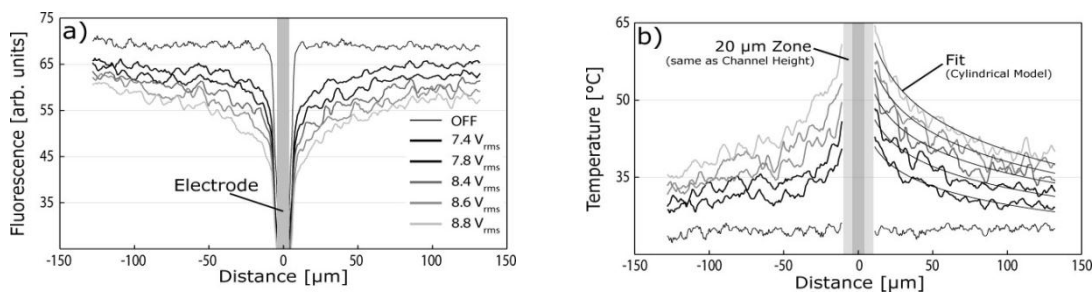


Figure 2.26 Fluorescence intensity for various voltages and their calculated temperature profiles. (Reproduced from [15])

In the second experimental method, water-soluble polymers with thermo-precipitating properties are implemented to detect temperature thresholds. These polymers are soluble in water at low temperatures but separate from solution when the temperature is raised above the lower critical solution temperature (LCST). The effect is reversible. LCSTs were optically determined in a thermo-cycled water bath to be  $29 \pm 1^\circ\text{C}$  and  $40 \pm 1^\circ\text{C}$ . The heat generated will cause the polymers to become optically detectable if the medium locally reaches or exceeds the LCST. Consequently, the boundary between the visible polymers and transparent solution would be the known temperature of either  $29^\circ\text{C}$  or  $40^\circ\text{C}$ . This kind of measurement does not make it possible to obtain 2D temperature distributions in one shot. Instead, one can sweep through a range of applied voltages and record the distance between the electrodes and the known boundary. The  $40^\circ\text{C}$  temperature boundary was measured at a distance of about  $150\mu\text{m}$  for an applied voltage of  $8.8V_{\text{rms}}$ , which is consistent with Fig. 2.25.

Each of the two experimental methods has advantages and disadvantages. The fluorescence method allows an optical assessment of 2D temperature distributions, but its precision depends on the calibration and illumination uniformity. The advantage using the thermo-precipitating polymers is the ability to probe absolute temperature without optical intensity calibration. However, only one temperature can be obtained in one measurement. A

benefit having two independent experimental methods is that if they are in agreement, the data is more reliable.

### 2.4.3 Jaeger *et al.*, 2007

In the work by Jaeger *et al.* [40], many different thermometry methods are implemented to measure temperature rises caused by DEP joule heating. The DEP chips consist of 5 dielectrophoretic elements: 2 funnels and 3 octode cages (Fig. 2.27). Two different types of voltages are applied to the octode cages. In AC mode, opposite electrodes of the four electrode pairs are supplied with the same phase, while there is a phase shift of  $\pi$  between neighboring electrodes. In the ROT mode, electrodes on one glass plane are driven with phases of  $0$ ,  $\pi/2$ ,  $\pi$ , and  $3\pi/2$  in a circular manner while the opposite electrode of each pair is phase shifted by  $\pi$ . The ROT mode is most similar to our work because top and bottom electrodes have opposite polarity.

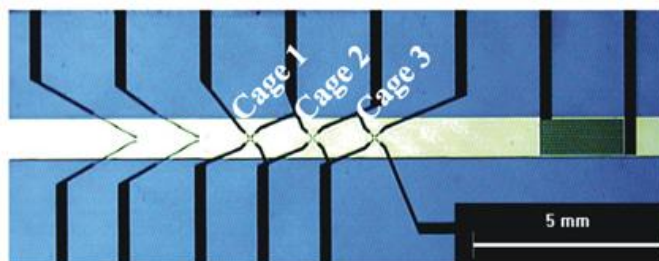


Figure 2.27 Image of microfluidic channel and electrode structures. (Reproduced from [40])

All thermometry methods had their own advantages and limitations. Ohmic resistors offered easy implementation, but they must be placed at some distance from the dielectrophoretic elements. The themofluorometry method used Rhodamine B as similarly utilized by Ross *et al.* and Seger-Sauli *et al.* and provides high spatial resolution. The Rhodamine B concentration was  $100\mu\text{M}$ , which again is a toxic amount to cells [39]. Liquid crystal sensors best mimic the situation of a cell trapped in a dielectrophoretic element, but seem to be more susceptible to

interference from electric fields. IR thermometry is a convenient method. However, IR only detects the temperature of the outer glass surface of the channel and is incapable of measuring inside the buffer. The bubble size thermometry method is problematic because it also must be placed some distance from the dielectrophoretic elements. All of the methods help to obtain a full understanding of the temperature profile in the microfluidic channel. Unfortunately, the methods are very different and not easy to compare. Only a bulk temperature rise averaged over a larger area can be compared fairly.

## 2.5 Literature review of microfluidic F-P refractometers

This section presents a literature review of microfluidic refractometry specifically using a Fabry-Pérot optical cavity. Microfluidic refractometers can be used to measure the refractive index of a fluid or biological samples. The Fabry-Pérot optical cavities are good for refractometry because the transmission spectrum is highly dependent on the optical path length inside the cavity. Consequently, any method using a Fabry-Pérot optical cavity will need to separate the refractive index and physical cavity length.

The process of separating refractive index from optical path length can be avoided by a few methods. First, one can measure the change in the optical path length, such that any change in resonant wavelength indicates a change in refractive index, assuming the cavity length does not change. The change in refractive index,  $\Delta n$ , may or may not be preferred over an absolute value of refractive index,  $n$ . Secondly, one can measure the resonant wavelengths for liquids with calibrated refractive indices. This  $\lambda_m$  versus  $n$  calibration curve can then be used to determine unknown refractive indices, again assuming the cavity length does not change. The calibration curve will need to be completed for different devices as fabrication likely causes the cavity length to be different. Thirdly, one can measure a resonant wavelength  $\lambda_{ml}$  for liquids

with an unknown refractive index shortly after measuring a resonant wavelength  $\lambda_{m0}$  with a known refractive index, such as water. The unknown refractive index can then be determined by  $n_1 = n_0(\lambda_{m1} / \lambda_{m0})$ .

One of the primary areas of review is how the Fabry-Pérot refractometers are constructed. If dielectric mirrors are implemented, light penetration into the mirrors will cause the cavity length to appear larger for wavelengths different than the mirror resonant wavelength. It will be noted if the authors used dielectric mirrors and corrected for the light penetration. Furthermore, the cavity length may change if a polymer is used to construct the microfluidic channels. Water can diffuse into the polymer over time and distort the cavity length [41]. Lastly, the refractometer needs to be constructed such that light within the cavity is collimated to avoid losses.

### **2.5.1 Device 1: Domachuk *et al.*, 2006**

Domachuk *et al.* [42] introduces a microfluidic refractometer using two single-mode fibers, incorporating fiber Bragg gratings (FBGs) to form the Fabry-Pérot cavity. The resolution of the refractometer is enhanced by collimating the beam across the channel. This is done by attaching a graded index fiber, which is a fiber with a parabolic refractive index. Figure 2.28 presents a schematic of the optical device. The fibers are held in SU-8 alignment channels on either side of the microfluidic channel. The gap between the fibers is set manually to approximately 50 $\mu$ m. The cavity length does not need to be accurate because a  $\lambda_m$  versus  $n$  calibration curve will be established.

Once the fibers are in the channel, the whole device is covered with a polydimethylsiloxane (PDMS) seal. Wavelengths are swept around 1550nm, which is the resonant wavelength of the FBGs. Consequently, there should be negligible penetration into the

mirrors [43]. Figure 2.29 presents the resonant wavelengths for calibrated refractive indices. In addition to the data, the device is simulated using coupled mode theory. The authors claim good agreement is observed between theory and experiment. From the data, the responsivity of the device (gradient of the linear fit in Fig. 2.29) is 6.825nm. The authors state this is sufficient to detect up to 0.2 percent-by-weight variation in saline solution concentration.

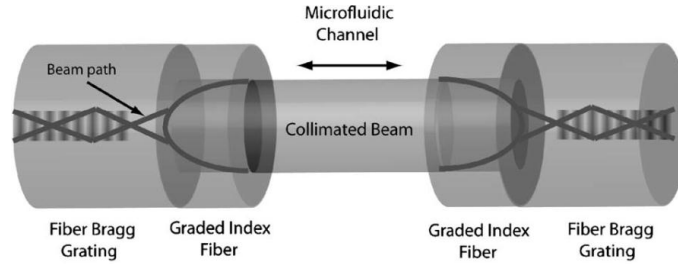


Figure 2.28 Schematic diagram of the Fabry-Pérot cavity. (Reproduced from [42])

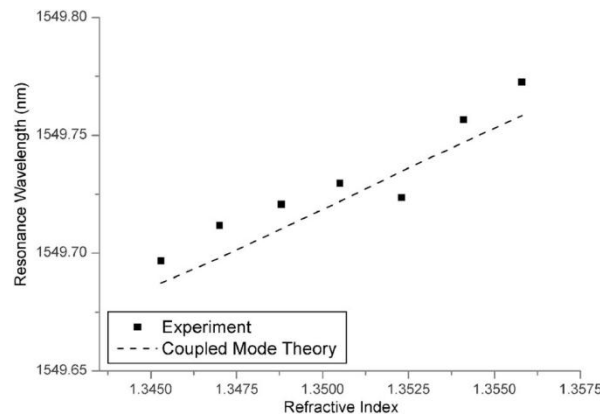


Figure 2.29 Refractometer resonant wavelengths for provided solutions with known refractive indices. (Reproduced from [42])

### 2.5.2 Device 2: Song *et al.*, 2006

Song *et al.* [44] reports a microfluidic refractometer formed by two aligned single mode fibers, and is designed to measure the refractive index of biological cells. Cells are a non-uniform medium causing different parts of the cell to have different refractive indices. This is verified in later work with quantitative refractive index imaging [45]. However, an effective refractive index can represent the entire cell. The effective RI is a key indicator to determine protein levels or to discriminate normal and cancerous cells. A difficulty arises when trying to

distinguish the cell's physical length from its refractive index. The work by Song *et al.* proposes a differential method in which two buffers with slightly different refractive indices are used. Another challenge occurs when considering the refraction of light caused by the cell. The cell could ultimately be considered a lens in a microfluidic channel.

The design of the microfluidic refractometer is seen in Fig. 2.30. Each of the input and output fibers are coated with a layer of gold, approximately 40nm thick, to have a reflectivity of 80%. The microchip is formed by scribing the microfluidic structures on poly methylmethacrylate (PMMA). The input and output fibers form a gap of 35.5 $\mu\text{m}$ , which is measured using an optical microscope. This distance between the fibers will be used to calculate the physical length of the cell. The cell holder is used to temporarily fix the cell during measurement, and is actually a micropipette controlled by another syringe pump. The wavelength range is from 1475nm to around 1625nm.

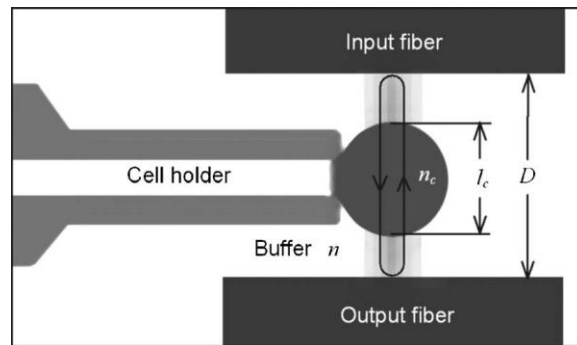


Figure 2.30 Working principle of the microfluidic device. The light in the cavity is illustrated as if there is no refraction caused by the cell. (Reproduced from [44])

Two buffer solutions with slightly different refractive indices are used alternatively in a measurement. Four spectra are obtained as a result: (1) no cell and buffer 1, (2) no cell and buffer 2, (3) with cell and buffer 1, and (4) with cell and buffer 2. With these spectra, the authors have presented equations for the cell's physical length and refractive index. The first two spectra

only need to be measured once for calibration, whereas the second two spectra with the cell will need to be measured for each cell. This raises concerns about the throughput of the device, especially if it takes time to alternate the buffers. A further concern is whether the buffers are indeed completely changed after the alteration.

Additionally, the first two spectra provide the refractive index of buffer 2 using the relation  $n_2 = n_1(\lambda_{m2} / \lambda_{m1})$ . Buffer 1 is phosphate buffered saline with a nominal refractive index  $n_1 = 1.350$ . This value seems pretty high considering the refractive index of water in Section 2.2.4 and the estimation of the refractive index of PBS in Section 2.2.5. However, the refractive index formulation for water is only approved up to a wavelength of  $1.1\mu\text{m}$ . Buffer 2 is a combination of PBS and a small amount of ethylene glycol to obtain a slightly higher refractive index. The accuracy of the fluidic FP cavity is determined by measuring the refractive index of buffer 2 multiple times. Buffer 2 is measured four times with a resulting standard deviation of 0.1%. The authors claim that since the buffer does not change, the standard deviation actually indicates the measurement accuracy. It is ambiguous if the buffers are changed between the four measurements.

### **2.5.3 Device 3: St-Gelais *et al.*, 2009**

In the work by St-Gelais *et al.* [46], a refractive index sensor is built using vertically etched silicon Bragg reflectors. The authors note previous microfluidic Fabry-Pérot interferometers [42, 44], but distinguish themselves as the first to use silicon/air Bragg reflectors. Silicon is chosen as it permits flexibility in the design, minimizes the number of fabrication steps, and reaches the highest resolution reported for a volume refractive index sensor integrated with a microfluidic system. This claim as the highest resolution device will be technically reviewed in a later section.

Figure 2.31 presents a schematic view of the refractometer as well as scanning electron microscope (SEM) images. Each Bragg reflector is made of three layers of silicon and two layers of air to ensure a high reflectivity. These mirrors have a theoretical bandwidth of 80nm for a reflectivity of  $R > 90\%$ . The central wavelength of the band is left unknown. An etch is made near the channel to allow conventional single-mode fibers to be inserted in the alignment grooves. The cavity length is  $24.5\mu\text{m}$ , which is chosen as it is larger than the thickness of the mirrors,  $11.1\mu\text{m}$ . Consequently, most of the electromagnetic field is located in the liquid rather than the mirrors. This raises the question of what the actual cavity length is due to penetration into the mirrors. However, the cavity length does not need to be accurate because a  $\lambda_m$  versus  $n$  calibration curve will be established.

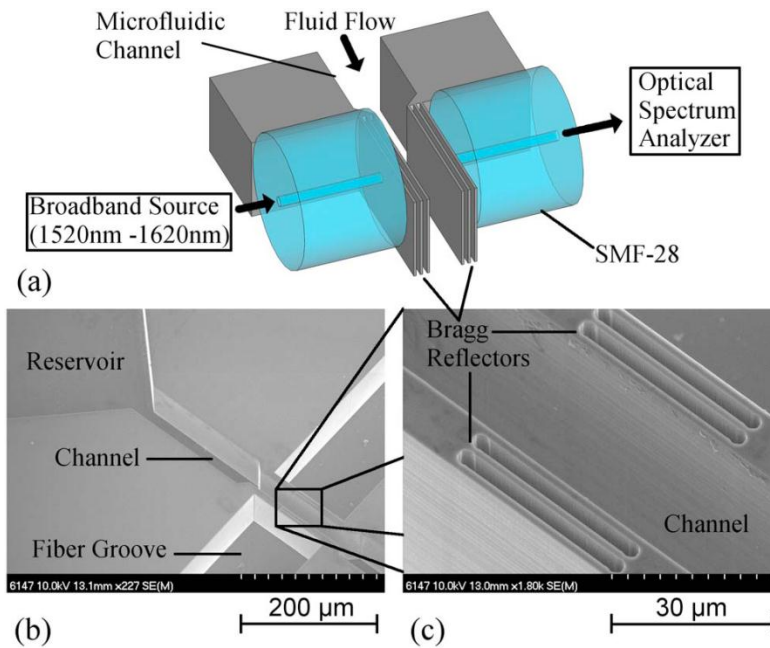


Figure 2.31 Schematic view and SEM figures of the microfluidic refractometer. (Reproduced from [46])

Experiments are performed at room temperature with certified refractive index liquids. These liquids have a low temperature dependence ( $0.0004\text{ }^{\circ}\text{C}^{-1}$ ), but are a little higher than the

$dn/dT$  of water ( $0.00014 \text{ } ^\circ\text{C}^{-1}$ ) as discussed in Section 2.2.4. The liquids are placed in the reservoir and flow into the channel by a capillary effect. Light is incident on the Fabry-Pérot cavity at a wavelength range of 1520 to 1620nm. The transmitted light is collected and the resonant wavelengths are found. Figure 2.32 presents the resonant wavelengths at the discrete refractive indices, as well as a simulation curve. The authors claim the simulations match the experimental results perfectly with a sensitivity of 907nm/RIU.

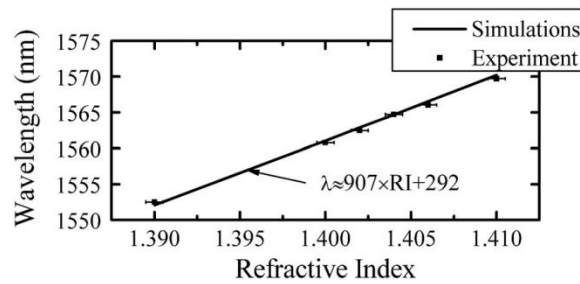


Figure 2.32 Experimental and simulated  $\lambda_m$  vs.  $n$  curve. (Reproduced from [46])

Despite the high reflectivity mirrors, the optical cavity has a relatively low quality factor. The quality factor for the  $n=1.400$  spectrum is  $Q=400$ , which is converted to finesse by [47, 48]:  $\mathcal{F} = Q \times FSR / \lambda_m$ , where  $\mathcal{F}$  is the finesse,  $FSR$  is the free spectral range, and  $\lambda_m$  is the resonant frequency. The paper for the  $n=1.400$  spectrum shows there are resonant wavelengths at 1560nm and 1590nm, such that the free spectral range is close to 30nm. Consequently, the finesse is about 8 for both the resonant wavelengths.

The authors state that because of the low quality factor, the main source of uncertainty is expected to be the amplitude noise that is superimposed on the resonance spectrum. This source of error was quantified by recording the transmission spectrum for the  $n=1.400$  liquid at a quantity of 20 times at 90s intervals. The resonant wavelengths had a standard deviation of

$\sigma = 0.005\text{nm}$ , resulting in a detection limit of  $3\sigma = 0.015\text{nm}$ . From this value and the sensitivity, a refractive index resolution is calculated to be  $\Delta n = 3\sigma / \text{sensitivity} \approx 1.7 \times 10^{-5} \text{RIU}$ .

#### 2.5.4 Device 4: Chin *et al.*, 2010

Chin *et al.* [49] reports an optofluidic Fabry-Pérot resonator, which specializes in a pair of liquid microlenses for efficient light coupling into the cavity. The authors critique Domachuk *et al.*, and state that using a graded index fiber end makes the control of the length for full collimation difficult, and also reduces the measurement range as the cavity range is increased. The liquid microlenses proposed by Chin *et al.* are of high optical performance and allow for real-time tuning. Figure 2.33 is a schematic of the overall optofluidic resonator with the liquid microlenses. The chip is fabricated in polydimethylsiloxane (PDMS) using soft lithography, and the mold is fabricated using SU-8 on a silicon wafer.

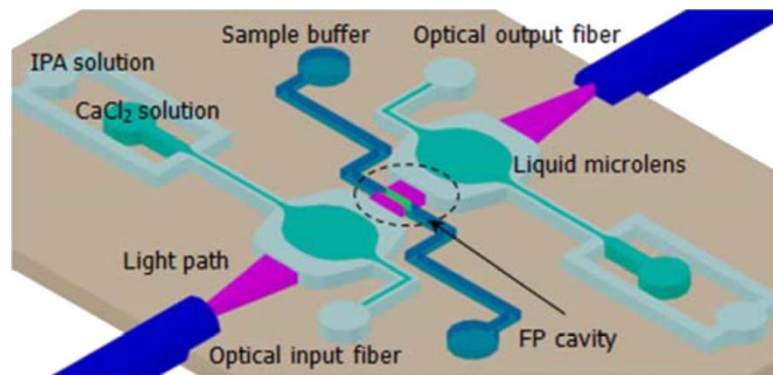
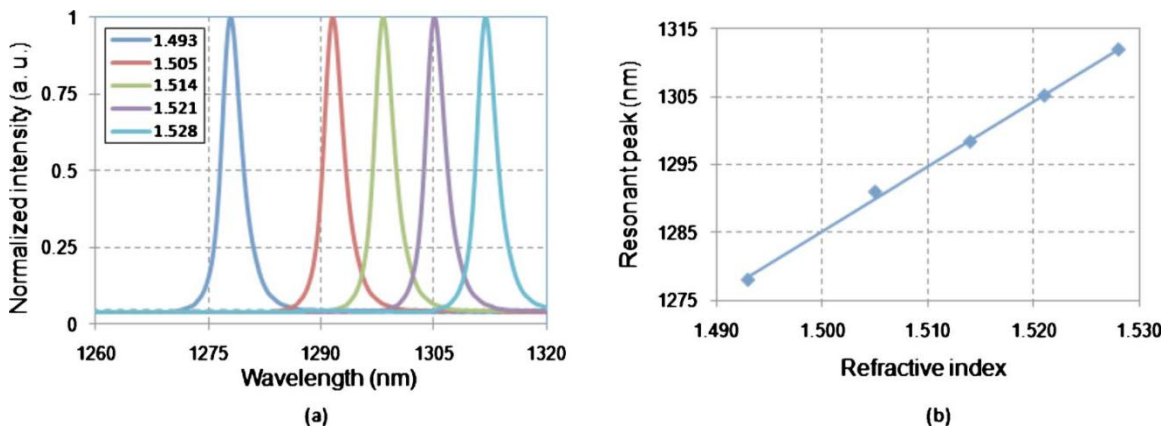


Figure 2.33 Schematic of the refractometer with fluid lenses. (Reproduced from [49])

The liquid microlenses are formed using two different solutions and different flow rates. The central flow stream is injected with  $4.16 \text{ mol L}^{-1} \text{CaCl}_2$  solution ( $\text{RI} = 1.4621$ ), and the side flow streams are injected with an isopropyl alcohol solution ( $\text{RI} = 1.3802$ ). It is claimed by the

authors that diffusion at the liquid interfaces due to concentration differences between the liquids is minimized because the diffusion distance of  $\text{Ca}^{2+}$  and  $\text{Cl}^-$  ions is reduced when the flow rate is very fast. Since the refractive index of the central stream is larger than the side streams, a biconvex converging lens is formed. Tuning the ratio of the flow rates will result in different radii of curvature ( $r$ ). The highest finesse was achieved when liquid microlenses with  $r = 138\mu\text{m}$  were formed, indicating the light is collimated in the FP cavity.

Figure 2.34(a) provides the transmission spectra for certified refractive index fluids. These fluids have low temperature dependence ( $0.0004\text{ }^\circ\text{C}^{-1}$ ) to avoid measurement error due to the surrounding temperature. Again, this  $dn/dT$  is a little higher than water ( $0.00014\text{ }^\circ\text{C}^{-1}$ ). Figure 2.34(b) provides the relationship between the refractive index of the sample liquid and the resonant peak. The sensitivity is measured as  $960\text{nm}/\text{RIU}$ , which the authors claim to be in good agreement with a theoretical calculation based on the perturbation method. The detection limit, defined as  $FWHM / \text{sensitivity}$  is estimated by the authors to be 0.01. This is a different way to determine detection limit compared to the method used by St-Gelais *et al.*



### 2.5.5 Summary of all devices

A literature review was completed, with four microfluidic refractometer devices under critique. These devices were chosen as they are made with a Fabry-Pérot optical cavity, similarly utilized in this work. Table 2.8 presents a summary of the four devices. The refractometer reported by Song *et al.* (Device 2) was intended for measuring the refractive index of biological cells, while the other three are exclusively for liquids. All of the devices operated in the infrared with wavelength ranges from 1260nm to 1650nm. This makes sense, because all of the refractometers presented were based on optical fibers that have an optical window around 1550nm. None of the authors addressed mirror penetration, but this was not necessary. One other concern was the use of polymers in many of the devices. It is quite possible that water entered the polymer and changed the cavity length.

Table 2.8 Comparison of the different microfluidic Fabry-Pérot refractometers.

Device	Wavelength range	RI values from data	Reported finesse	Reported sensitivities and limits	Comments
1 [42]	1549.65nm to 1549.80nm	1.3452 1.3470 1.3488 1.3506 1.3524 1.3542 1.3560		RI changes: 0.2%  Responsivity: 6.825nm / RIU	
2 [44]	1475nm to 1650nm	1.365	5.2	Accuracy: 0.1%	- Measured buffer RI relative to PBS. - Accuracy is defined as the standard deviation on the buffer RI.
3 [46]	1550nm to 1575nm	1.390 1.400 1.402 1.404 1.406 1.410	Q=400, so finesse is about 8	Sensitivity: 907nm / RIU,  Resolution: $\Delta n = 1.7 \times 10^{-5}$ RIU	- Resolution is defined as $3\sigma/\text{sensitivity}$ , where $\sigma$ is the standard deviation of resonant wavelengths.
4 [49]	1260nm to 1315nm	1.493 1.505 1.514 1.521 1.528	18.79	Sensitivity: 960nm / RIU  Detection limit: ~0.01 RIU	- Detection limit is defined as FWHM/sensitivity.

The four different refractometers all had different methods in determining the accuracy of the device. However, the three refractometers not dealing with biological cells all produced a responsivity, or sensitivity value. This value was the linear slope of the  $\lambda_m$  versus  $n$  calibration curve. As mentioned earlier, providing a  $\lambda_m$  versus  $n$  curve avoids the need to separate refractive index from the optical path length in the cavity. It turns out the linear slope actually hides this information. Section 2.1.1 presents the relation  $\lambda_m = 2nL/m$ , where  $n$  is the refractive index in the cavity,  $L$  is the cavity length, and  $m$  is the resonant mode number. Consequently, the slope of the  $\lambda_m$  versus  $n$  curve is equal to  $2L/m$ . This slope will also include any light penetration into the mirrors, as  $L = L_{cav} + L_{mirror}$ . The authors of Devices 3 and 4 used the sensitivity value in different ways to calculate the limit of the device. St-Gelais *et al.*, the author of Device 3, seems to have calculated the limit of the device in the best fashion because it is based on the noise of the spectrum.

## References

- [1] <http://perg.phys.ksu.edu/vqm/laserweb/Ch-4/F4s4t1p1.htm>
- [2] J. T. Verdeyen, *Laser Electronics*, 2nd ed. Englewood Cliffs, NJ: Prentice-Hall, 1989.
- [3] G. R. Fowles, *Introduction to Modern Optics*, 2nd ed. Mineola, NY: Dover Publications, Inc., 1989.
- [4] H. Shao, "Optofluidic intracavity spectroscopic biosensing system for single cell identification," Ph.D. dissertation, Dept. Elect. Comp. Eng., Colorado State Univ., Fort Collins, CO, 2007.
- [5] W. J. Ellison, "Permittivity of pure water, at standard atmospheric pressure, over the frequency range 0-25 THz and the temperature range 0-100°C," *J. Phys. Chem. Ref Data*, vol. 36, no. 1, pp.1-18, 2007.
- [6] <http://www.lrsm.upenn.edu/~frenchrh/download/0208fwootenopticalpropertiesofsolids.pdf>
- [7] V. S. Langford, A. J. McKinley, and T. I. Quickenden, "Temperature dependence of the visible-near-infrared absorption spectrum of liquid water," *J. Phys. Chem. A*, vol. 105, no. 39, pp. 8916-8921, 2001.
- [8] R. Weissleder, "A clearer vision for in vivo imaging," *Nature Biotechnology*, vol. 19, no.4, pp. 316-317, 2001.
- [9] B. E. A. Saleh and M. C. Teich, *Fundamentals of Photonics*, New York, USA: John Wiley & Sons, Inc., 1991.

- [10] P. Schiebener, J. Straub, J. M. H. Levelt Sengers, and J. S. Gallagher, "Refractive index of water and steam as function of wavelength, temperature, and density," *J. Phys. Chem. Ref. Data*, vol. 19, no. 3, pp. 677-717, 1990.
- [11] A. H. Harvey, J. S. Gallagher, and J. M. H. Levelt Sengers, "Revised formulation for the refractive index of water and steam as a function of wavelength, temperature and density," *J. Phys. Chem. Ref. Data*, vol. 27, no. 4, pp. 761-774, 1998.
- [12] W. Wagner and A. Pruß, "The IAPWS formulation 1995 for the thermodynamic properties of ordinary water substance for general and scientific use," *J. Phys. Chem. Ref. Data*, vol. 31, no. 2, pp. 387-535, 2002.
- [13] <http://chemistry.about.com/od/imagesclipartstructures/ig/Science-Clipart/Osmosis---Blood-Cells.htm>
- [14] B. M. Notaroš, *Electromagnetics*, Upper Saddle River, NJ: Prentice Hall, 2011.
- [15] U. Seger-Sauli, M. Panayiotou, S. Schnydrig, M. Jordan, and P. Renaud, "Temperature measurements in microfluidic systems: heat dissipation of negative dielectrophoresis barriers," *Electrophoresis*, vol. 26, no.11, pp. 2239-2246, 2005.
- [16] [http://www.kayelaby.npl.co.uk/general\\_physics/2\\_7/2\\_7\\_9.html](http://www.kayelaby.npl.co.uk/general_physics/2_7/2_7_9.html)
- [17] R. C. Smith and K. S. Baker, "Optical properties of the clearest natural waters (200-800 nm)," *Applied Optics*, vol. 20, no. 2, pp. 1981.
- [18] K. M. Aly and E. Esmail, "Refractive index of salt water: effect of temperature," *Optical Materials*, vol. 2, no. 3, pp. 195-199, 1993.

- [19] G. H. Markx and C. L. Davey, "The dielectric properties of biological cells at radiofrequencies: applications in biotechnology," *Enzyme and Microbial Technology*, vol. 25, no. 3-5, pp. 161-171, 1999.
- [20] R. Pethig, "Dielectrophoresis: status of the theory, technology, and applications," *Biomicrofluidics*, vol. 4, 2010.
- [21] L. A. MacQueen, M. D. Buschmann, and M. R. Wertheimer, "Gene delivery by electroporation after dielectrophoretic positioning of cells in a non-uniform electric field," *Bioelectrochemistry*, vol. 72, no. 2, pp. 141-148, 2008.
- [22] E. Tekle, R. D. Astumian, and P. B. Chock, "Electroporation by using bipolar oscillating electric field: an improved method for DNA transfection of NIH 3T3 cells," *Proc. Natl. Acad. Sci. USA*, vol. 88, no. 10, pp. 4230-4234, May 1991.
- [23] J. Gehl, "Electroporation: theory and methods, perspectives for drug delivery, gene therapy and research," *Acta Physiologica Scandinavica*, vol. 177, no. 4, pp. 437-447, 2003.
- [24] P. Marszalek, D. -S Liu, and T. Y. Tsong, "Schwan equation and transmembrane potential induced by alternating electric field," *Biophysical Journal*, vol. 58, no. 4, pp. 1053-1058, 1990.
- [25] T. Y. Tsong, "Electroporation of cell membranes," *Biophysical Journal*, vol. 60, no. 2, pp. 297-306, 1991.
- [26] K. H. Schoenbach, S. Katsuki, R. H. Stark, E. S. Buescher, and S. J. Beebe, "Bioelectrics—new applications for pulsed power technology," *IEEE Transactions on Plasma Science*, vol. 30, no. 1, pp. 293-300, Feb 2002.
- [27] [http://ocw.mit.edu/courses/chemical-engineering/10-626-electrochemical-energy-systems-spring-2011/lecture-notes/MIT10\\_626S11\\_lec28.pdf](http://ocw.mit.edu/courses/chemical-engineering/10-626-electrochemical-energy-systems-spring-2011/lecture-notes/MIT10_626S11_lec28.pdf)

- [28] P. Nelson, *Biological Physics*, Updated 1st ed., New York, NY: W. H. Freeman and Company, 2008.
- [29] A. T. Conlisk, S. Datta, W. H. Fissell, and S. Roy, "Biomolecular transport through hemofiltration membranes," *Ann Biomed Eng.*, vol. 37, no. 4, pp. 722-736, 2009.
- [30] F. N. Ishikawa, M. Curreli, C. A. Olson, H. Liao, R. Sun, R. W. Roberts, R. J. Cote, M. E. Thompson, and C. Zhou, "Importance of controlling nanotube density for highly sensitive and reliable biosensors functional in physiological conditions," *ACS Nano*, vol. 4, no. 11, pp. 6914-6922, 2010.
- [31] S. Gawad, L. Schild, and Ph. Renaud, "Micromachined impedance spectroscopy flow cytometer for cell analysis and particle sizing," *Lab Chip*, vol. 1, no. 1, pp. 76-82, 2001.
- [32] S. Gawad, K. Cheung, U. Seger, A. Bertsch, and P. Renaud, "Dielectric spectroscopy in a micromachined flow cytometer: theoretical and practical considerations," *Lab Chip*, vol. 4, no. 3, pp. 241-251, 2004.
- [33] S. Gawad, T. Sun, N. G. Green, and H. Morgan, "Impedance spectroscopy using maximum length sequences: application to single cell analysis," *Review of Scientific Instruments*, vol. 78, 2007.
- [34] T. Sun and H. Morgan, "Single-cell microfluidic impedance cytometry: a review," *Microfluid Nanofluid*, vol. 8, no. 4, pp. 423-443, 2010.
- [35] K. C. Cheung, M. D. Berardino, G. Schade-Kampmann, M. Hebeisen, A. Pierzchalski, J. Boci, A. Mittag, and A. Tárnok, "Microfluidic impedance-based flow cytometry," *Cytometry Part A*, vol. 77A, no. 7, pp. 648-666, 2010.
- [36] <http://www.facs.ethz.ch/news/Impedance>

- [37] X. He and J. C. Bischof, "The kinetics of thermal injury in human renal carcinoma cells," *Annals of Biomedical Engineering*, vol. 33, no. 4, pp. 502-510, 2005.
- [38] D. Ross, M. Gaitan, and L. E. Locascio, "Temperature measurement in microfluidic systems using a temperature-dependent fluorescent dye," *Analytical Chemistry*, vol. 73, no. 17, pp. 4117-4123, 2001.
- [39] R. S. Gupta and A. K. Dudani, "Species-specific differences in the toxicity of rhodamine 123 toward cultured mammalian cells," *Journal of Cellular Physiology*, vol. 130, no. 3, pp. 321-327, 1987.
- [40] M. S. Jaeger, T. Mueller, and T. Schnelle, "Thermometry in dielectrophoresis chips for contact-free cell handling," *J. Phys. D: Appl. Phys.*, vol. 40, no. 1, pp. 95-105, 2007.
- [41] G. Gervinskas, D. Day, and S. Juodkazis, "High-precision interferometric monitoring of polymer swelling using a simple optofluidic sensor," *Sensors and Actuators B*, vol. 159, no. 1, pp. 39-43, 2011.
- [42] P. Domachuk, I. C. M. Littler, M. Cronin-Golomb, and B.J. Eggleton, "Compact resonant integrated microfluidic refractometer," *Applied Physics Letters*, vol. 88, no. 9, 2006.
- [43] D. I. Babic, and S. W. Corzine, "Analytic expressions for the reflection delay penetration depth, and absorptance of quarter-wave dielectric mirrors," *IEEE Journal of Quantum Electronics*, vol. 28, no. 2, pp. 514-524, 1992.
- [44] W. Z. Song, X. M. Zhang, A. Q. Liu, and C.S. Lim, "Refractive index measurement of single living cells using on-chip Fabry-Pérot cavity," *Applied Physics Letters*, vol. 89, 2006.
- [45] Y. Sung, W. Choi, C. Fang-Yen, K. Badizadegan, R. R. Dasari, and M. S. Feld, "Optical diffraction tomography for high resolution live cell imaging," *Optics Express*, vol. 17, no. 1, pp. 266-277, 2009.

[46] R. St-Gelais, J. Masson, and Y. –A. Peter, “All-silicon integrated Fabry-Pérot cavity for volume refractive index measurement in microfluidic systems,” *Applied Physics Letters*, vol. 94, 2009.

[47] <http://www.rp-photonics.com/finesse.html>

[48] [http://www.rp-photonics.com/q\\_factor.html](http://www.rp-photonics.com/q_factor.html)

[49] L. K. Chin, A. Q. Liu, C. S. Lim, C. L. Lin, T. C. Ayi, and P. H. Yap, “An optofluidic volume refractometer using Fabry-Pérot resonator with tunable liquid microlenses,” *Biomicrofluidics*, vol. 4, 2010.

## Chapter 3: Modeling

In this chapter, theoretical models will be developed in order to better understand the OFIS chip. These models include a combination of general theory and computer simulations. By better understanding the OFIS chip through models, one can optimize designs without needing multiple iterations of chip fabrication. However, the downside of models is they are only as good as the assumptions made. This is why experimental observations have precedence over theoretical models.

The logical flow in each section will generally be theory and equations, parameters implemented in the model, assumptions, results, and comparison with the literature. The commercial software utilized in Sections 3.2 and 3.3 will be COMSOL Multiphysics, which has further instructions in Appendix D. In Section 3.4, the commercial software to be used is TFCalc by Software Spectra, Inc.

### 3.1 Electrostatics

The underlying physical phenomenon of this work is a time-changing electric field within a microfluidic channel. The microfluidic channel is a 3D structure that is formed in SU-8 with layers of glass on the top and the bottom. The electric field only needs to be determined in a 2D plane as illustrated in Fig. 3.1. One can easily calculate the magnitude of the electric field for a uniform distribution. However, it is important to know the non-uniform electric field distribution as it is a more accurate model, and accuracy is important to describe secondary physical phenomena. These secondary effects include dielectrophoretic forces and joule heating. Computer simulations are a useful way to visualize the non-uniform distributions for a range of input parameters.

### 3.1.1 Electrostatic equations

Figure 3.1 presents an illustration of the electrostatic geometry. Solutions are obtained by solving Laplace's equation,  $\nabla^2 V = 0$ , where  $V$  is the scalar electric potential and the value of zero indicates a charge-free region. Further details are found in Appendix A.2. Since the electric field varies sinusoidally in time, the scalar electric potential will represent the root-mean-square value. The charge-free region claim should be taken with some caution. The simulations often involve a phosphate buffered saline (PBS) solution in the microfluidic channel, where most of the electric field distribution occurs. PBS is a water-based solution and contains many salts. Water molecules are electrically neutral, but salts have charges when they are dissolved. Below in Table 3.1 lists the different salts in PBS and their respective concentrations in water using the recipe for 1X PBS (Appendix E). Since none of the concentrations are greater than 1%, it is assumed the charges are negligible.

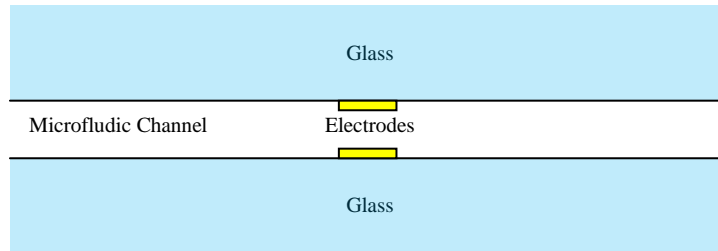


Figure 3.1 The general two dimensional structure for electrostatic simulations.

Table 3.1 A list of the salts in PBS and their respective concentration in water.

	<b>Concentration (g/L)</b>	<b>Concentration in water (%)</b>
NaCl	8	~0.8
KCl	0.2	~0.02
Na <sub>2</sub> HPO <sub>4</sub>	1.44	~0.144
KH <sub>2</sub> PO <sub>4</sub>	0.24	~0.024

Electrostatic boundary conditions are necessary to solve the simulation. These conditions relate normal and tangential electric field components at the boundary between two different mediums, and can be derived from Maxwell's equations. The conditions are:  $\epsilon_1 E_{n1} = \epsilon_2 E_{n2}$  and  $E_{t1} = E_{t2}$ , where  $\epsilon$  is the relative permittivity, subscripts 1 and 2 represent the two different mediums, and subscripts  $n$  and  $t$  indicate the normal and tangential components of the electric field, respectively. Boundary conditions have a significant impact when there is a large difference between the permittivity of the two different mediums. There is indeed a large permittivity difference between glass and water. Figure 3.2 is an illustration of the electric field vectors  $\mathbf{E}_1$  and  $\mathbf{E}_2$  between a glass and water interface. The magnitude of the electric field in each medium is given by  $|\mathbf{E}_1| = \sqrt{E_{n1}^2 + E_{t1}^2}$  and  $|\mathbf{E}_2| = \sqrt{E_{n2}^2 + E_{t2}^2}$ . Since the tangential components are equal, the electric field magnitude will be slightly larger in the glass.

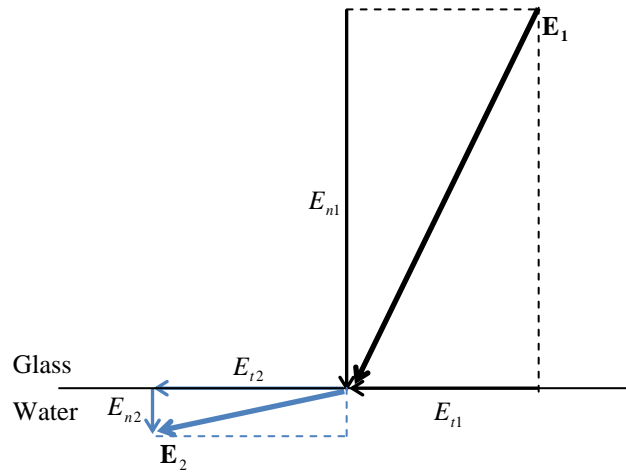


Figure 3.2 Example of the electric field normal and tangential components at the boundary between glass and water.

### 3.1.2 Dielectrophoresis

A phenomenon resulting from the non-uniform electric field in the microfluidic channel is a dielectrophoretic (DEP) force. This gradient force acts on dielectric particles, even including

biological cells. The dielectric particles do not necessarily need to be charged as the electric field will induce a charge on the particle. The strength of the DEP force depends on many parameters as seen in the following time-averaged equation [1]:

$$\langle F_{DEP} \rangle = 2\pi R^3 \varepsilon_m \operatorname{Re}[CM] \nabla |\mathbf{E}_{rms}|^2 \quad (3.1)$$

where  $R$  is the radius of the particle,  $\varepsilon_m$  is the permittivity of the medium,  $CM$  is the frequency dependent Clausius-Mossotti factor given by  $CM = (\tilde{\varepsilon}_p - \tilde{\varepsilon}_m) / (\tilde{\varepsilon}_p + 2\tilde{\varepsilon}_m)$ , where  $\tilde{\varepsilon}_p$  and  $\tilde{\varepsilon}_m$  are the respective complex permittivities of the particle and the medium. Complex permittivity is in the form:  $\tilde{\varepsilon} = \varepsilon + j\sigma/\omega$ , where  $j = \sqrt{-1}$ ,  $\omega$  is electrical frequency, and  $\sigma$  is the conductivity of the medium. Previous work by illustrates the dependence of the CM factor with respect to frequency and conductivity [2, 3]. If the CM factor is positive, the DEP force is positive and dielectric particles are pulled towards higher electric fields. If the CM factor is negative, the DEP force is negative and dielectric particles are pushed away from higher electric fields.

The vector field of the DEP force can be visualized with electrostatic simulations. This is possible because COMSOL Multiphysics allows the user to enter in equations for the desired results. Only the term  $\nabla |\mathbf{E}_{rms}|^2$  of Eq. 3.1 will be realized, since the other factors depend on the uncertain properties of the dielectric particle. The magnitude of the electric field vector is  $|\mathbf{E}_{rms}| = \sqrt{E_x^2 + E_y^2}$ , where  $x$  and  $y$  represent the 2D space. Only a two dimensional simulation is necessary for the electrostatic model because an additional dimension has little effect on the results of interest. Consequently, the gradient terms of Eq. 3.1 are:

$$\frac{\partial |\mathbf{E}_{rms}|^2}{\partial y} = \frac{\partial \left( \sqrt{E_x^2 + E_y^2} \right)^2}{\partial y} \quad (3.2)$$

$$\frac{\partial |\mathbf{E}_{rms}|^2}{\partial x} = \frac{\partial \left( \sqrt{E_x^2 + E_y^2} \right)^2}{\partial x} \quad (3.3)$$

The above equations can then be entered into COMSOL Multiphysics, where Eq. 3.2 is for the y-component and Eq. 3.3 is for the x-component. Further details of how to enter in these equations are found in Appendix D.1. In this work, the DEP force was often negative, so both Eq. 3.2 and 3.3 are multiplied by negative one to provide arrows that point in the negative DEP direction.

### 3.1.3 Model and results

The geometry for the electrostatic simulation is seen in Fig. 3.3. The channel height is set to be 20 $\mu\text{m}$  because it is close to experimental values. Overall dimensions are chosen to be large enough so that outside boundary conditions have negligible effect on the electric field distribution, and small enough so that a finer resolution mesh can be made. It is of interest to have a fine resolution mesh between electrodes in order to avoid the mesh size a being variable within that spatial area. Electrodes are given a thickness of 0.15 $\mu\text{m}$ , similar to the actual thickness, which automatically creates a higher resolution mesh near the electrodes.

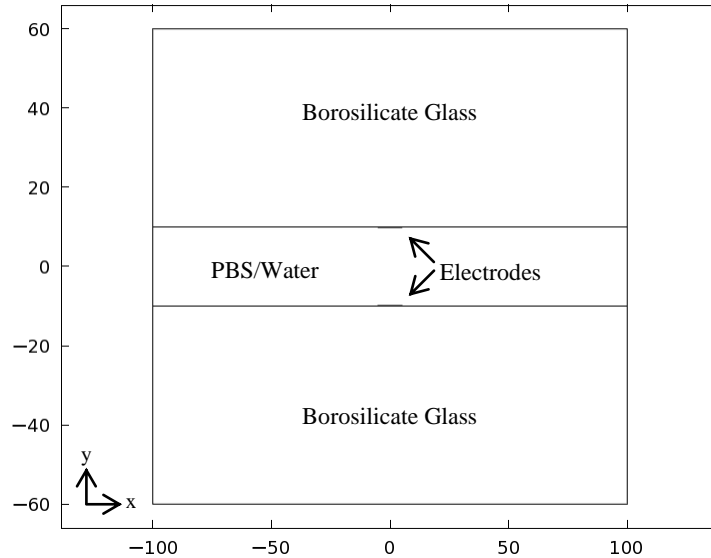


Figure 3.3 Geometry for the electrostatic simulation. The outer dimensions are 200 $\mu\text{m}$  wide by 120 $\mu\text{m}$  tall, the microfluidic channel is 20 $\mu\text{m}$  tall, and electrodes are 10 $\mu\text{m}$  wide by 0.15 $\mu\text{m}$  tall.

The fixed electrostatic parameters for each domain are listed in Table 3.2. One should note that even though this electrostatic simulation was of a microfluidic channel, no fluid properties were used. Furthermore, gold has a real permittivity value of 1, which is not physically accurate at RF frequencies. COMSOL Multiphysics uses the value of 1 for other pre-defined metals. The dimensions of the electrodes as well as the relatively small difference between the electrical permittivities of the gold and glass reduce this inaccuracy.

Table 3.2 Electrostatic parameters for each of the domains.

	<b>Water</b>	<b>PBS</b>	<b>Gold</b>	<b>Borosilicate Glass</b>
Relative permittivity [no unit]	80 [4]	(Water)	1	4.6 [5,6]

Variable parameters include the electrode configuration and the magnitude of the voltage applied to the electrodes. An electrode configuration consists of the electrode size, number, position, and applied voltage relative to other electrodes. While varying the electrode configurations, the voltage magnitude and the electrode width will remain the same. A voltage magnitude of  $5V_{\text{rms}}$  is chosen because it is close to the maximum voltage the function generator can produce at high frequency. The electrode width is chosen to be  $10\mu\text{m}$  since it is the minimum width that was possible during the time these simulations were first performed.

The useful types of results are the electric field magnitude distribution, the electric field lines, and the direction of the DEP force. COMSOL Multiphysics can produce these results and allows the user to plot different types of results on top of each other. This feature was made to good use by plotting the directional arrows of the DEP force on top of the electric field magnitude distribution. Electric field lines are practical because they show the vector direction of the electric field, thus representing the field uniformity. COMSOL creates random electric field lines in which the user only has control of the number of lines seen.

One of the first electrode configurations used in the project was based on a trap by Rosenthal and Voldman [7] and is simulated in Fig. 3.4. However, experiments indicated this trap did not provide a sufficient DEP force to oppose Stokes' drag force at useful cell velocities. Simulations were performed and demonstrated that a 3D electrode structure, with electrodes on the top and bottom of the microfluidic channel, does increase the DEP force. The simplest implementation of a 3D electrode structure is a dipole trap and is simulated in Fig. 3.5. In addition to creating stronger DEP forces, a design goal was to exert forces on both the downstream and upstream sides of the biological cell. Figure 3.6 shows how this can be implemented with two dipole traps, otherwise known as a double-dipole. The voltage for the double-dipole configuration is such that  $5V_{\text{rms}}$  is applied to the top two electrodes and the bottom two electrodes are at zero volts. The quadrupole electrode configuration in Fig. 3.7 is a variation of the double-dipole, in which the voltage in order of the top left, top right, bottom left, bottom right electrodes is  $5V_{\text{rms}}$ ,  $0V_{\text{rms}}$ ,  $0V_{\text{rms}}$ ,  $5V_{\text{rms}}$ . Figures 3.4 to 3.7 all illustrate an electric field magnitude discontinuity at the boundary between the glass and water. The reason for the discontinuity was explained earlier with electrostatic boundary conditions.

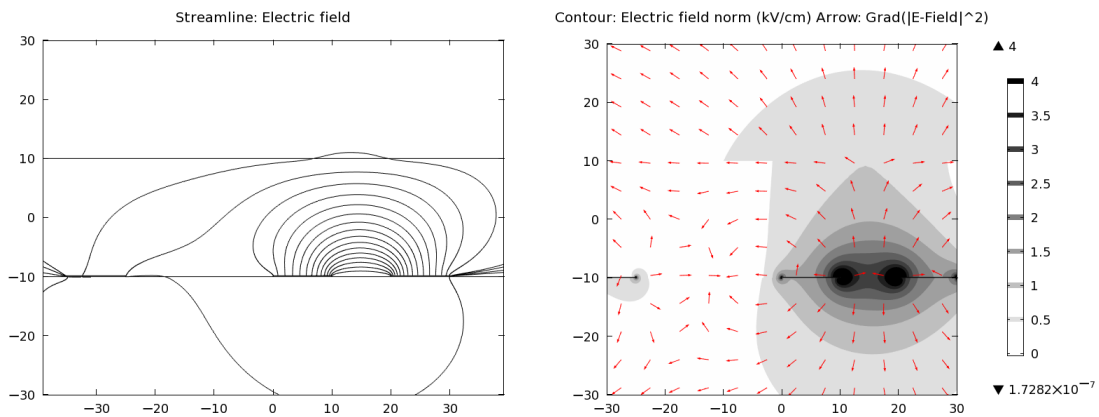


Figure 3.4 (a) Rosenthal and Voldman trap [7] electric field lines. (b) Electric field magnitude with  $\nabla|\mathbf{E}_{\text{rms}}|^2$  arrows.

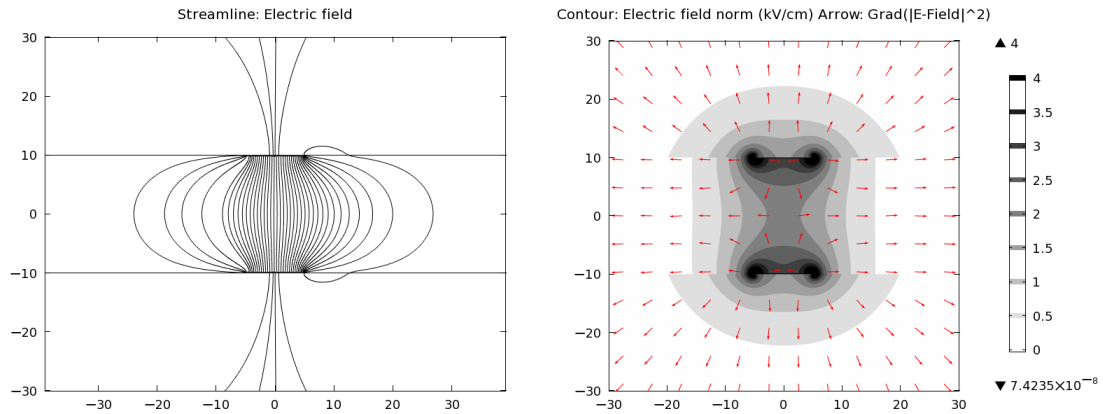


Figure 3.5 (a) Dipole electric field lines, where the asymmetry is a plotting artifact (b) Electric field magnitude with  $\nabla|\mathbf{E}_{rms}|^2$  arrows.

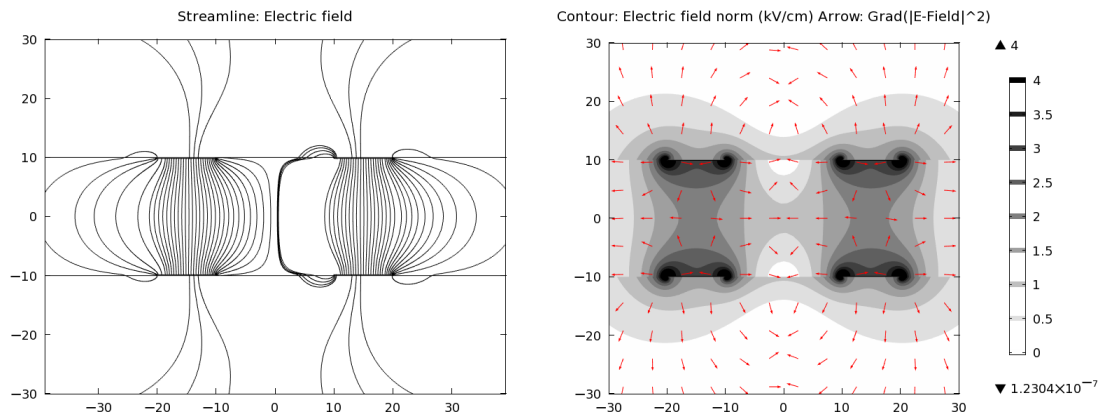


Figure 3.6 (a) Double-dipole electric field lines, where the asymmetry is a plotting artifact. (b) Electric field magnitude with  $\nabla|\mathbf{E}_{rms}|^2$  arrows.

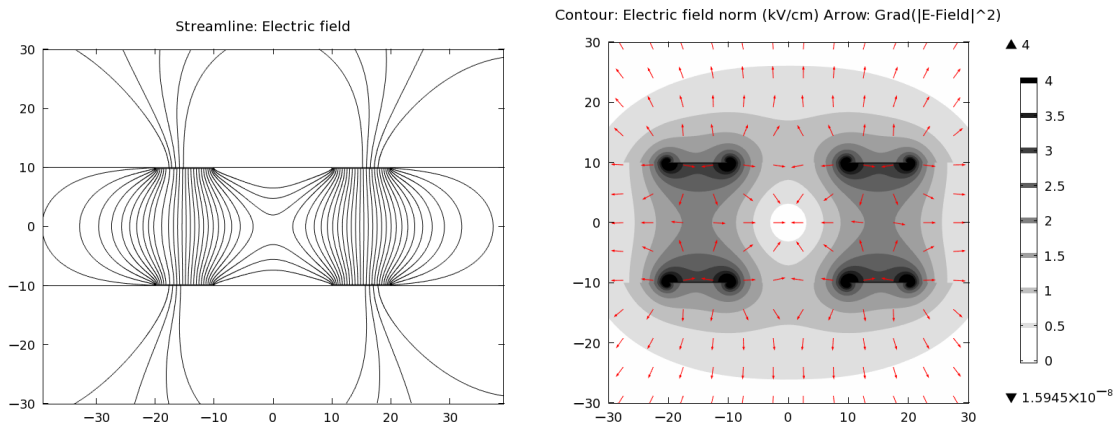


Figure 3.7 (a) Quadrupole electric field lines, where the asymmetry is a plotting artifact. (b) Electric field magnitude with  $\nabla|\mathbf{E}_{rms}|^2$  arrows.

Further post-processing of the simulations is possible by exporting the data to a text file. In particular, the electric field magnitude in the center of the microfluidic channel, or at  $y=0\mu\text{m}$ , is exported as two vectors of the same length,  $x_i$  and  $E_i$ . The electric field magnitude is squared and then a spatial derivative is taken to find the quantity  $\left| \text{Grad}(E_{rms}^2) \right|_{y=0}$ . To help reduce numerical noise from the derivative, the following method is used:

$$\left| \frac{\partial E_i^2}{\partial x} \right| \equiv \left| \frac{\Delta E_i^2}{\Delta x} \right| = \left| \frac{\frac{1}{3}(E_{i+1}^2 + E_{i+2}^2 + E_{i+3}^2) - \frac{1}{3}(E_{i-1}^2 + E_{i-2}^2 + E_{i-3}^2)}{\frac{1}{3}(x_{i+1} + x_{i+2} + x_{i+3}) - \frac{1}{3}(x_{i-1} + x_{i-2} + x_{i-3})} \right| \quad (3.4)$$

where  $i$  is the index of the vector. Consequently, the resulting derivative vector is shortened by three index values both at the beginning and ending of the vector. Figure 3.8 shows the resulting E-field squared and  $\left| \text{Grad}(E_{rms}^2) \right|_{y=0}$  for the different electrode configurations. It is convenient to have chosen  $y=0\mu\text{m}$  for the dipole, double-dipole, and quadrapole electrode configurations because the DEP arrows are in the same direction as  $\left| \text{Grad}(E_{rms}^2) \right|_{y=0}$ . Figure 3.9 presents the maximum of the electric field gradient for the dipole electrode configuration.

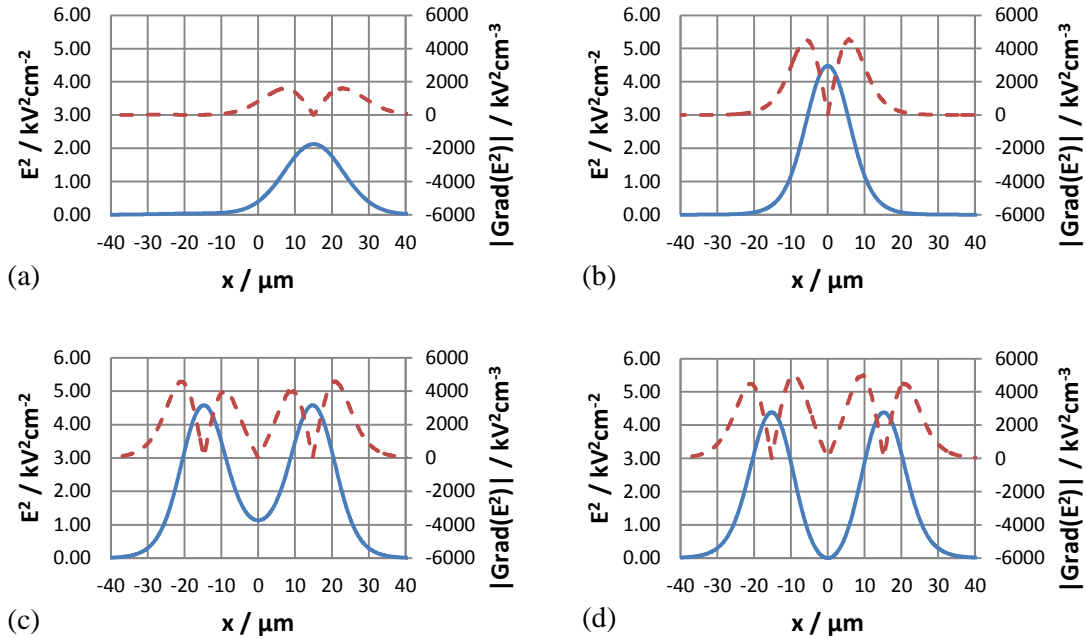


Figure 3.8 E-field squared (solid) and gradient of E-field squared (dashed) at  $y=0\mu\text{m}$  for (a) Rosenthal and Voldman [7], (b) dipole, (c) double-dipole, and (d) quadrupole electrode configurations.

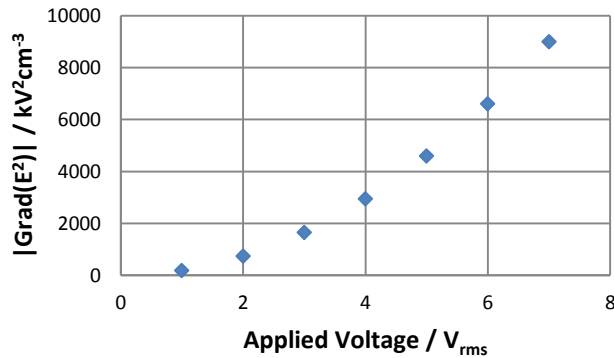


Figure 3.9 The maximum electric field gradient of the dipole electrode configuration as a function of applied voltage. This indicates the DEP force is quadratic with applied voltage.

Similar work was performed by Ramos *et al.* to obtain electric field and electric field gradient plots [1]. Ramos *et al.* found an electric field gradient for planar electrodes on the range of  $10 \text{ kV}^2 \text{ cm}^{-3}$  to  $100,000 \text{ kV}^2 \text{ cm}^{-3}$ , such that electric field gradient values in Fig. 3.8 and Fig. 3.9 fall within this range. Furthermore, the time-averaged DEP force on a biological cell can now be estimated from the electric field gradient. Choosing  $7\mu\text{m}$  polystyrene spheres,

$R = 3.5\mu\text{m}$ ,  $\varepsilon_m = 80\varepsilon_0$ ,  $\text{Re}[CM(\omega)] = -0.5$ ,  $\nabla|\mathbf{E}_{rms}|^2 = 1000\text{kV}^2\text{cm}^{-3}$ , then Eq. 3.1 is a negative DEP force of  $\sim 95\text{pN}$ . The time-averaged DEP force was also calculated experimentally by measuring the velocity of a polystyrene sphere and presuming drag forces are equal and opposite of DEP forces. Details of this calculation are found in Appendix C.1 and are in agreement with the values above.

## 3.2 Joule heating

The combination of high electric fields and a high conductivity solution in the microfluidic channel results in the phenomenon of joule heating. This model should be in 3D space since heat transfer in all spatial directions is important to determine the non-uniform temperature profile. From the temperature profile, one can estimate the viability of biological cells based on the temperature and time of exposure. A peak temperature of  $65^\circ\text{C}$  for less than a minute can reduce the viability of suspended cells to 30% [8].

### 3.2.1 AC joule heating

The particular case of AC or RF joule heating is of interest since a high frequency is necessary to avoid electrolysis of the water. A steady-state relationship between electric field and temperature has been previously derived by Ramos *et al.* [1]:

$$k\nabla^2 T + \sigma E^2 = 0 \quad (3.5)$$

Where  $k$  is the thermal conductivity,  $T$  is the temperature,  $\sigma$  is electrical conductivity, and  $E$  is electric field. The Joule Heating Model in COMSOL Multiphysics uses the following differential equation found in the User's Guide (Version 4.1, p. 496):

$$\rho C_p \frac{\partial T}{\partial t} - \nabla \cdot (k \nabla T) = Q \quad (3.6)$$

where  $\rho$  is the density,  $C_p$  is the heat capacity, and  $Q$  is the heat source. The simulations are time-independent since the temperature usually reaches steady-state in less than a second [1]. Since all materials are modeled to have a scalar thermal conductivity, Eq. 3.6 equals Eq. 3.5 when the heat source density is given by  $Q = \sigma E^2$ . The electrostatic simulations above for the dipole electrode configuration at  $5V_{\text{rms}}$  indicate an E-field squared value of about  $4 \text{ kV}^2 \text{ cm}^{-2}$ , or  $40 \times 10^9 \text{ V}^2 \text{ m}^{-2}$ . Considering a reasonable PBS electric conductivity of  $1.25 \text{ S m}^{-1}$  [9], the heat source density is then on the scale of  $50 \text{ GW m}^{-3}$ . The approximate volume of the dipole electrode structure is  $25\mu\text{m} \times 400\mu\text{m} \times 20\mu\text{m}$ , resulting in a power dissipation on the order of  $10 \text{ mW}$ .

### 3.2.2 Temperature dependent parameters

To improve the physical accuracy of the AC joule heating model, the temperature dependence of various parameters may be considered. In particular, the electrical conductivity, electric permittivity, and thermal conductivity of the PBS solution are known to depend on temperature. The relations for each parameter are found in [10] and reproduced here:

$$\sigma(T) = \sigma_0(1 + \alpha(T - T_0)) \quad (3.7)$$

$$\varepsilon(T) = 78.54 \left( 1 - (T - 25^\circ\text{C}) \left( 4.6 \times 10^{-3} - 8.86 \times 10^{-6} (T - 25^\circ\text{C}) \right) \right) \quad (3.8)$$

$$k(T) = 0.555 - 2.71 \times 10^{-5} \sqrt{T} - T \left( 9.93 \times 10^{-5} - T \left( 6.27 \times 10^{-5} - 4.9286 \times 10^{-7} T \right) \right) \quad (3.9)$$

where  $T$  is the dependent variable for temperature,  $T_0$  is the reference temperature,  $\alpha$  is the conductivity temperature coefficient, and  $\sigma_0$  is the electrical conductivity at the reference temperature. An advantage of COMSOL Multiphysics is that a variable for temperature can be entered into the input fields for electrical conductivity, electric permittivity, and thermal conductivity. Thus, the temperature dependencies can be modeled.

Including Eq. 3.7, 3.8, or 3.9 is only useful if their respective values change significantly over the temperature range of interest. Plots of the equations are seen in Fig. 3.10 and percent

changes are calculated for each equation in Table 3.3. Reasonable values were chosen for Eq. 3.7 where  $\sigma_0 = 1.25 \text{ S m}^{-1}$ ,  $\alpha = 0.022$ , and  $T_0 = 22^\circ\text{C}$ . Each of these equations can also be prioritized for use in the model by how much their value changes. Consequently, the priority to include temperature dependence would be in order of electrical conductivity, electrical permittivity, and thermal conductivity.

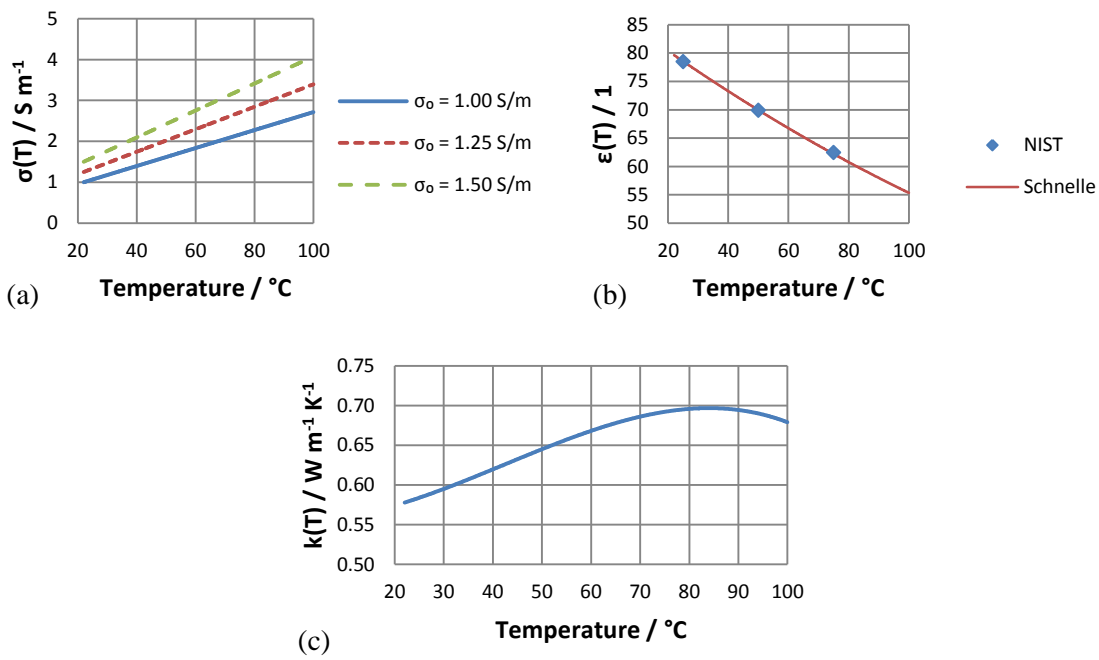


Figure 3.10 Plots of the temperature dependent parameters (a) electrical conductivity, (b) electrical permittivity, and (c) thermal conductivity.

Table 3.3. Percent changes of temperature dependent parameters.

$T / ^\circ\text{C}$	$\sigma(T)$ % change from $22^\circ\text{C}$	$\epsilon(T)$ % change from $22^\circ\text{C}$	$k(T)$ % change from $22^\circ\text{C}$
22	0%	0%	0%
25	+6.6%	-1.37%	+1.05%
50	+61.6%	-12.2%	+11.6%
75	+117%	-21.9%	+19.8%
100	+172%	-30.5%	+17.5%

A problem that is caused by adding the linearized temperature dependence of electrical conductivity is that an asymptote might be created. This problem is observed when Eq. 3.5 is solved for a parallel plate capacitor in one dimension, as provided by Ramos *et al.* and reproduced here:  $\Delta T = \sigma V_{rms}^2 / (8k)$ , where  $V_{rms}$  is the RMS voltage applied to the capacitor. By including Eq. 3.7, the temperature rise becomes:

$$\Delta T = \left( \frac{\sigma_0 V_{rms}^2}{8k} \right) \left( 1 - \frac{\sigma_0 \alpha V_{rms}^2}{8k} \right)^{-1} \quad (3.10)$$

This equation has an asymptote at an applied voltage of  $V_{rms} = \sqrt{(8k)/(\sigma_0 \alpha)}$ . A similar asymptote arises when Jaeger *et al.* [11] includes temperature dependence of electrical conductivity. However, there is likely not an asymptote when all of the temperature dependent parameters are considered and most certainly not an asymptote in experimental work. To understand where the asymptote might be in the COMSOL simulation with only  $\sigma(T)$ , a thermal circuit model has been developed in Appendix A.4. This circuit model begins with the temperature rise given by Eq. 3.10 and then includes heat transfer into the glass substrate and superstrate. The analytic solution from the circuit model runs into problems when trying to determine the spreading thermal resistances.

### 3.2.3 Model and results

The geometry for the joule heating simulation is seen in Fig. 3.11. The channel height is set to be 20 $\mu$ m because it is close to experimental values. For simplicity, only the dipole electrode configuration is implemented. The electrode width is chosen to be 30 $\mu$ m to be consistent with experiments. Overall dimensions were chosen to be large enough that outside boundary conditions had negligible effect on the temperature distribution.

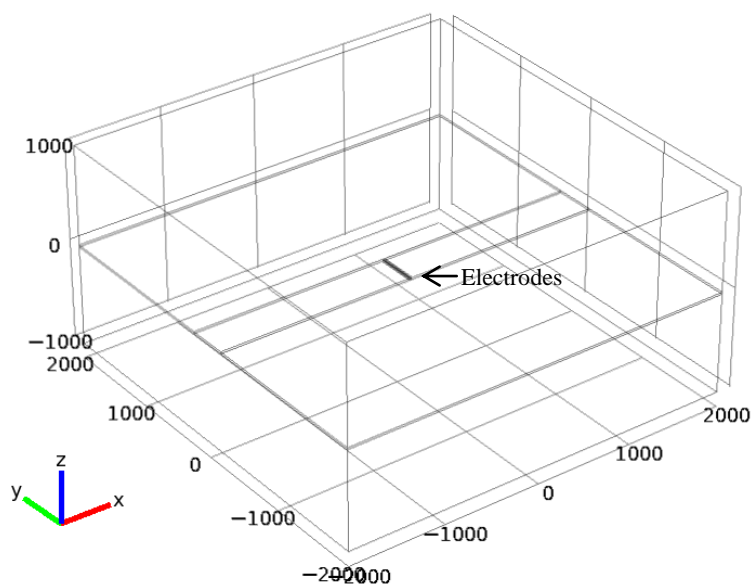


Figure 3.11 Geometry for the joule heating simulation. The outer dimensions are  $4\text{mm} \times 4\text{mm} \times 2\text{mm}$ , the microfluidic channel is  $20\ \mu\text{m}$  tall, and electrodes are  $30\ \mu\text{m}$  wide with no height.

The joule heating parameters for each domain are listed in Table 3.4. No fluid properties were used as liquid cooling is a negligible effect [1]. In addition to the borosilicate glass, sapphire glass is also simulated. Sapphire glass has a high thermal conductivity that allows heat to be spread away from the electrodes and reduce the temperature rise in the microfluidic channel. Consequently, higher voltages can be applied to the electrodes without compromising cell viability with temperature exposure. This allows for a greater DEP force as seen back in Fig. 3.9, such that the opposing Stokes' drag force, and consequently cell velocity, can be higher. A higher cell velocity results in higher throughput as the volumetric flow rate is proportional to the velocity.

Table 3.4 Joule heating parameters for each of the domains. The density of PBS should be slightly higher than water. Density and heat capacity are ignored in steady-state, as observed in Eq. 3.6.

	<b>PBS</b>	<b>Borosilicate Glass</b>	<b>Sapphire Glass</b>	<b>SU-8</b>
Relative permittivity [no unit]	Eq. 3.8	4.6 [5,6]	10 [12, 13]	3.2 [14]
Electric conductivity [S/m]	Eq. 3.7, $\sigma_0=1.25$ [9]	1e-13 [5]	1e-12 [12, 13]	5e-15 [14]
Thermal conductivity [W/(m·K)]	Eq. 3.9	1.14 [5]	40 [12, 13]	0.2 [14, 15, 16]
Density [kg/m <sup>3</sup> ]	1000 (water)	2230 [5,6]	3980 [12, 13]	1218 [16]
Heat capacity [J/(kg·K)]	4181 (water)	830 [6]	750 [13]	1200 [16]

It is again of interest to have a fine resolution mesh between electrodes in order to avoid the mesh size a being variable within that spatial area. The idea implemented in the 2D model, where electrodes are given a thickness of 0.15 $\mu\text{m}$  to automatically create a higher resolution mesh, creates too many elements in three dimensions. This is a problem because the selected computer only has enough computational power to solve for an empirically determined 30,000  $\pm$  3,000 mesh elements. An excessive number of elements results in an out of memory error message and the problem is not solved. Thus, the electrodes will have no thickness and will instead be 2D planes.

In order to create a finer resolution mesh between electrodes, boundary layer meshes will be applied. A boundary layer mesh is a mesh with a dense element distribution along specific boundaries. The general idea for meshing is illustrated in Fig. 3.12 (a) and (b). Two boundary y-z planes were placed within the dimensions of the microfluidic channel and were spaced 10 $\mu\text{m}$  from each other. This mesh design was compared with computers that have a greater computational power in Appendix D.3.

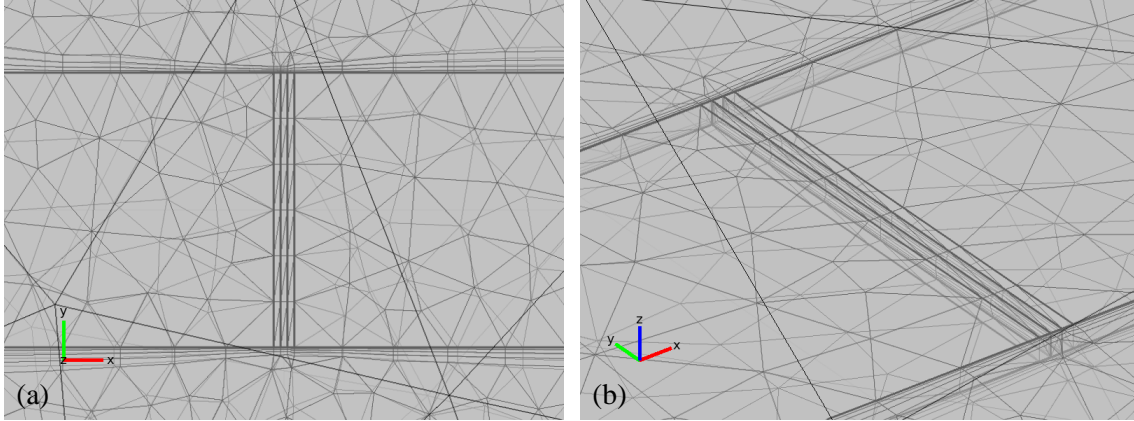


Figure 3.12 Boundary y-z planes to improve mesh as viewed in (a) x-y plane and (b) 3D view.

Simulation results for the dipole electrodes and borosilicate glass is presented in Fig. 3.13(a) and Fig 3.13(b). The same results are shown for the sapphire glass in Fig. 3.14 (a) and Fig 3.14 (b). At an applied voltage of  $4V_{\text{rms}}$ , the maximum temperature rise of the borosilicate glass is  $48^{\circ}\text{C}$ , whereas the sapphire glass is  $6^{\circ}\text{C}$ . This returns a ratio of maximum temperature rises between the borosilicate and sapphire glass of 8. Conversely, the ratio of thermal conductivities between glass types is about 35. Therefore, the ratio of thermal conductivities is not a good estimate for how much the temperature will be reduced with sapphire, as the temperature distribution also needs to be considered.

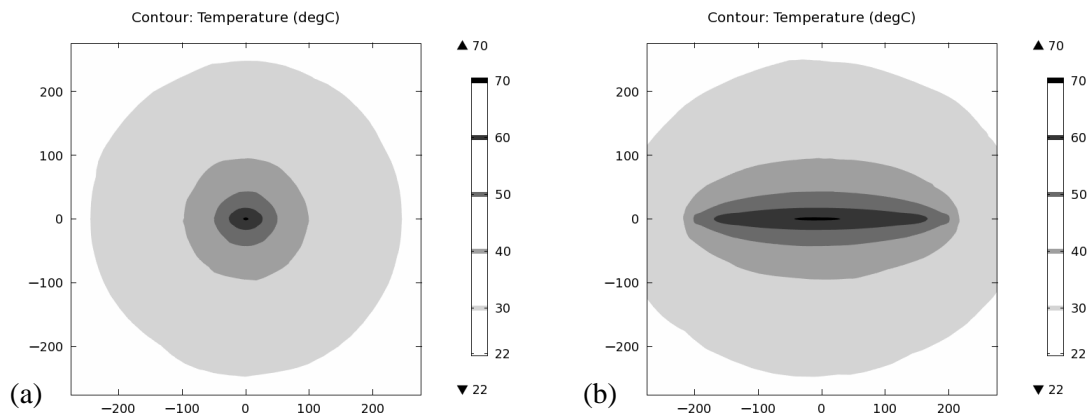


Figure 3.13 Temperature distribution with borosilicate glass and dipole electrodes in (a) z-x plane and (b) y-z plane.

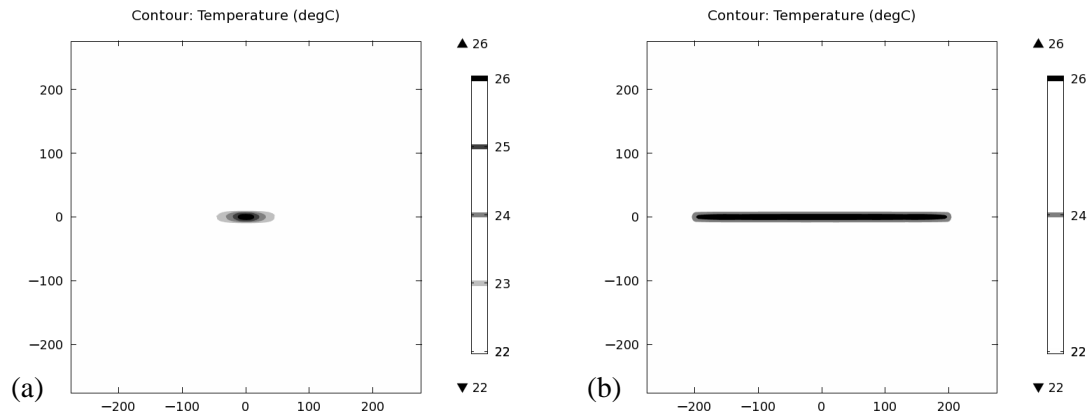


Figure 3.14 Temperature distribution with sapphire glass and dipole electrodes in (a) z-x plane and (b) y-z plane.

### 3.3 Optics

The microfluidic channel in an OFIS chip is also an optical resonant cavity formed by two plane mirrors on the top and bottom of a microfluidic channel. More specifically, the optical resonant cavity acts as a plane-plane Fabry-Pérot interferometer. The mirrors that are implemented are high-reflecting dielectric mirrors, which are created by multiple thin layers of materials. Each layer is a quarter-wavelength in optical thickness in order to create constructive interference. Optical modeling is done to understand penetration depth into the dielectric mirrors and its effect on the Fabry-Pérot transmission spectra. The cavity length, or the refractive index in the cavity, can then be calculated with higher accuracy from the transmission spectra.

Furthermore, a discovery was made in which the significant amount of joule heating in the microfluidic channel creates a negative or positive gradient index lens, depending on the electrode configuration. This is a result of temperature-dependent refractive index as described in Chapter 2. An optical model is developed to calculate the focal length of both the negative and positive gradient index lens. The negative gradient lens inherently creates an unstable cavity,

which is confirmed with geometrical optics and an ABCD matrix. Joule heating simulations are repeated in order to provide temperature profiles.

### 3.3.1 Mirror penetration depth

In a dielectric mirror with multiple layers, some light is reflected and some light is transmitted at each interface between layers. Mirror penetration depth is the distance into the mirror where light appears to reflect, or the energy falls to  $1/e$  of its initial value [17]. The smaller the refractive index difference is between each layer, the more transmitted light there will be and the larger the penetration depth is. Optical modeling is useful to determine the penetration depth for a given mirror structure.

With the intention to compliment experimental work, mirror structures include the experimental mirrors themselves along with extreme structures that have index contrast values larger and smaller than the experimental mirrors. The first experimental mirror is  $\text{HfO}_2/\text{SiO}_2$  layers on borosilicate glass and was fabricated by a commercial vendor. The other mirror is  $\text{SiN}_x/\text{SiO}_2$  layers on sapphire glass and was fabricated in-house. Due to the higher quality of the vendor mirror, only it will be used as the experimental mirror for optical modeling.

The transmission spectrum of the  $\text{HfO}_2/\text{SiO}_2$  mirror is provided by the vendor and is seen digitized in Fig. 3.15. The minimum of the transmission spectra indicates the mirror center wavelength is 880nm. This value is important as it will be the reference for a quarter-wavelength. Another method to determine the center wavelength is to use the next two valleys of the transmission spectrum at wavelengths  $\lambda_1$  and  $\lambda_2$ . These secondary valleys are narrower, such that the wavelengths are easier to determine. The center wavelength is then given by  $\lambda = 2(1/\lambda_1 + 1/\lambda_2)^{-1}$  and also returns 880nm.

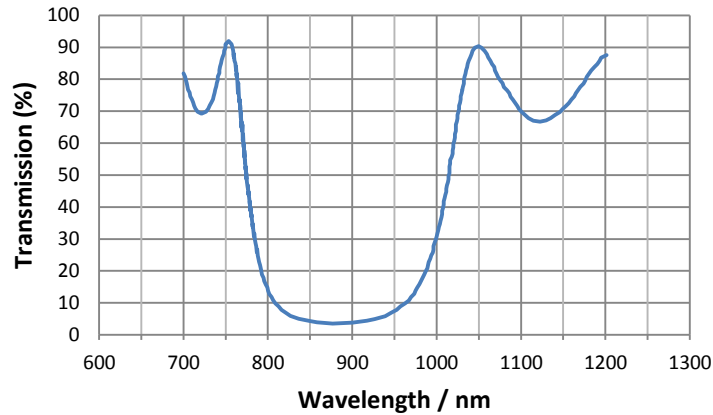


Figure 3.15 Digitized reflection spectra provided by the mirror vendor. The center wavelength occurs at the minimum transmission, which results in a center wavelength of 880nm.

In addition to the center wavelength, the composition of the experimental mirror needs to be known. Information is provided that states the mirror contains 13 quarter-wavelength layers of  $\text{HfO}_2/\text{SiO}_2$  where the first and last layers are  $\text{HfO}_2$ . This choice is intended to maximize the reflectivity of the mirror, since it creates the largest index contrast between the medium and the first layer of the mirror. The commercial simulation package TFCalc already has pre-defined  $\text{HfO}_2$  and  $\text{SiO}_2$  materials such that their refractive indices versus wavelength are given (Appendix F). The thickness of the borosilicate glass is 1mm, but unfortunately TFCalc does not have this material in its database. Borosilicate glass is mostly composed of silica so  $\text{SiO}_2$  will be used instead.

The two additional mirrors with index contrast values larger and smaller than the experimental mirror need to be designed. For notational simplicity, the larger index contrast is called the “hard” mirror, the smaller index contrast is called the “soft” mirror, and the experimental mirror itself is called “our” mirror. A simulation is first performed to find the maximum reflection of our mirror. Then, the hard and soft mirrors are designed to have the

necessary number of layers and refractive indices to obtain the same maximum reflection as our mirror. A disadvantage of the hard and soft mirror designs is the refractive indices of their layers are constant across all wavelengths. Hard and soft mirrors could be designed with wavelength dependence, but is considered unnecessary since these are arbitrary materials and the purpose of this modeling is for a conceptual understanding.

The resulting mirror structures and their TFCalc simulations of reflectivity and phase are presented in Fig. 3.16 to 3.18. All mirrors utilized SiO<sub>2</sub> as the substrate, since silicon dioxide has the closest refractive index as the experimentally used glass, Schott Nexterion Glass B. The bandwidth of the mirror decreases as the mirror becomes softer. Additionally, the slope of the phase within the bandwidth increases as the mirror becomes softer. One should note that TFCalc provides phase reflection for both S and P polarization, but only S polarization is shown in the figures. This is to reduce redundancy and because the S polarization is easier to display. The P polarization is centered about a reflection phase of 0 degrees, but often alternates with 360 degrees. The relation between S and P polarizations at normal incidence is noted by Hecht [18] with amplitude reflection coefficients:

$$[r_{\parallel}]_{\theta_i=0} = [-r_{\perp}]_{\theta_i=0} = \frac{n_t - n_i}{n_t + n_i} \quad (3.11)$$

where  $\perp$  indicates perpendicular (S) polarization,  $\parallel$  indicates parallel (P) polarization,  $n_i$  is refractive index in the incident medium, and  $n_t$  is refractive index in the transmitted medium. Since  $n_t > n_i$  for the dielectric mirrors, then  $r_{\parallel}$  is positive and  $r_{\perp}$  is negative, or in other words is a 180 degrees phase shift for S polarization.

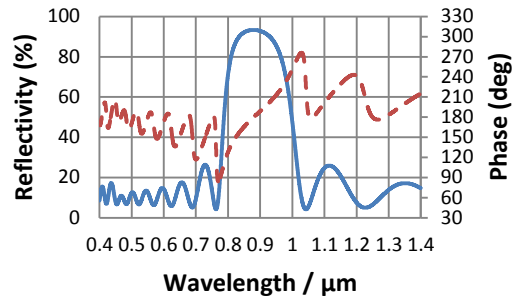
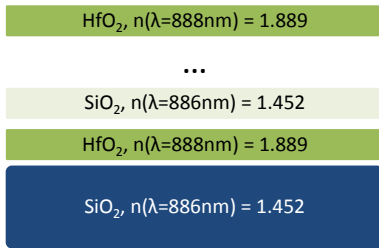


Figure 3.16 “Our” mirror composition, and a spectrum of its reflectivity (solid line) and phase (dashed line).

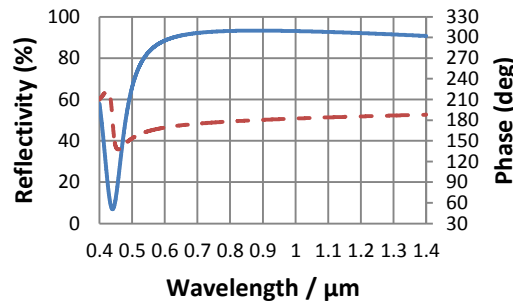
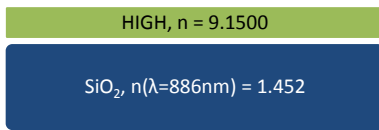


Figure 3.17 “Hard” mirror composition, and a spectrum of its reflectivity (solid line) and phase (dashed line).

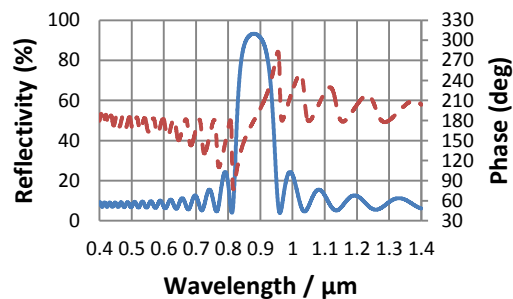
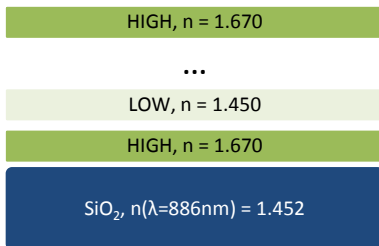


Figure 3.18 “Soft” mirror composition, and a spectrum of its reflectivity (solid line) and phase (dashed line).

Analytical solutions to calculate mirror penetration depth have been derived by Babic and Corzine [17] and Garmire [19]. Garmire includes mirror penetration depth for an odd number of layers, or  $N+1/2$  layered pairs, and is reproduced here:

$$L_r = \frac{\left[ 1 - \frac{n_1 n_2}{n_f^2} \left( \frac{n_1}{n_2} \right)^{2(N+1/2)} \right] \left[ 1 - \left( \frac{n_1}{n_2} \right)^{2(N+1/2)} \right] \left[ \frac{n_1 n_2}{n_i (n_2 - n_1)} \frac{\lambda_0}{4} \right]}{1 - \left( \frac{n_2 n_1}{n_f n_{FP}} \right)^2 \left( \frac{n_1}{n_2} \right)^{4(N+1/2)}} \quad (3.12)$$

where  $n_1$  and  $n_2$  are the refractive indices of the alternating mirror layers,  $N$  is the number of layer pairs,  $n_f$  is the refractive index of the glass,  $n_{FP}$  is the refractive index of the medium, and  $\lambda_0$  is the center wavelength of the mirror. Garmire notes that “for  $N+1/2$  layer pairs the last layer will have a refractive index  $n_1$ .” In Fig. 3.19, Eq. 3.12 is plotted as a function of  $n_{FP}$  for fixed values of  $n_1$  and  $n_2$  that represent the  $\text{HfO}_2/\text{SiO}_2$  mirror. The penetration depth increases with increasing medium refractive index, as the index contrast reduces between the medium and the first layer. Additional plots are shown in Fig. 3.20(a) where  $n_2$  is kept constant, and in Fig. 3.20 (b) where  $n_1$  is kept constant.

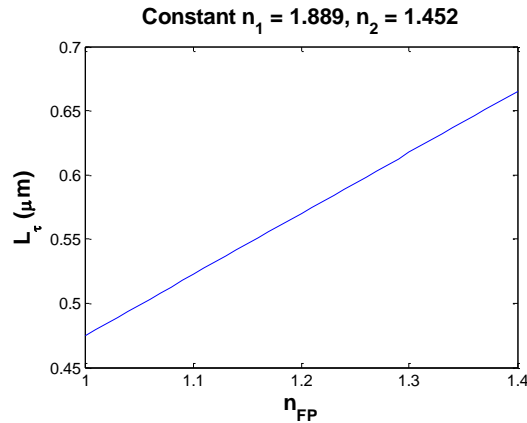


Figure 3.19 Mirror penetration depth for fixed mirror layers  $n_1$  and  $n_2$ , and varying cavity refractive index,  $n_{FP}$ . The figure indicates that mirror penetration depth is about  $0.48\mu\text{m}$  for air and  $0.64\mu\text{m}$  for water.

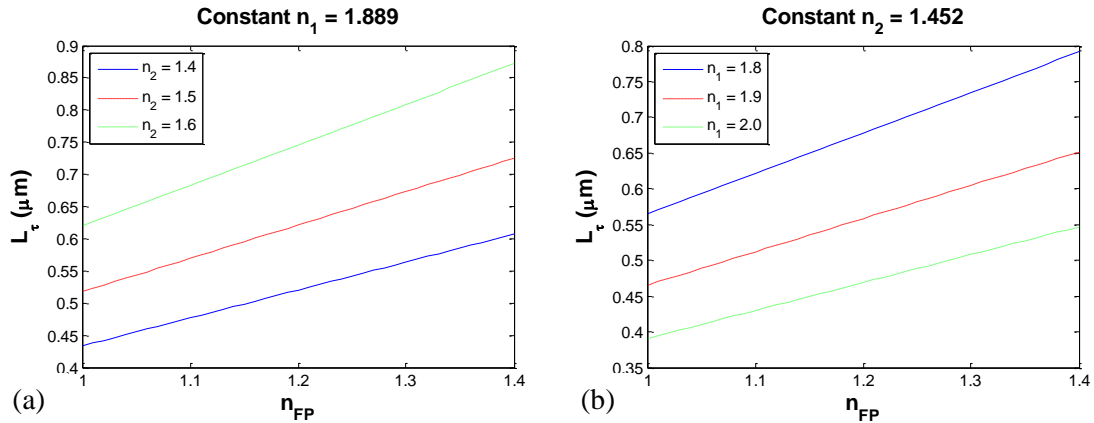


Figure 3.20 Mirror penetration depth for various parameters, where (a)  $n_1$  is fixed and (b)  $n_2$  is fixed.

### 3.3.2 F-P spectra with mirror penetration

In an optical cavity, mirror penetration depth will cause the cavity length to appear larger than the actual physical separation between the mirrors. Figure 3.21 presents simulations of transmission spectra using TFCalc, which is designing software for optical thin-films. The previously defined mirrors created the optical cavity. Thus, the cavity notation is “hard”, “soft”, and “our” for each of the respective mirror types. The FP equation represents mirrors that do not have any mirror penetration, which is closest to the hard cavity. The resonant modes of both soft and our cavities are off from the FP equation, and become further off at wavelengths further from the mirror center wavelength of 880nm.

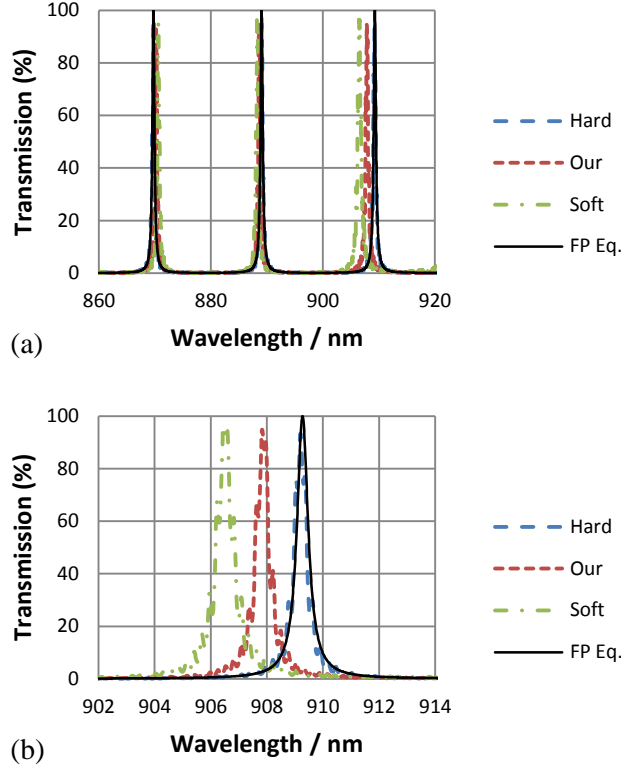


Figure 3.21 Simulated Fabry-Pérot transmission spectra and calculated transmission using the FP equation. Simulations utilize a 20 $\mu\text{m}$  cavity length and air as the medium in the cavity. Wavelength ranges are (a) 860nm to 920nm and (b) 900nm to 916nm.

The mirror penetration can be accounted for using the round-trip phase in the Fabry-Pérot cavity. The sum of phase terms in the cavity round-trip is provided by Eq. (28) in [17] and is reproduced here:

$$2\beta_m(L_{FP} + 2L_\tau) - 2\omega_o\tau = 2\pi m \quad (3.13)$$

where  $\beta_m = n_{FP}\omega_m/c$  is the propagation constant of the  $m$ th mode,  $L_{FP}$  is the cavity length,  $L_\tau$  is the mirror penetration depth,  $\omega_o$  is the mirror center frequency, and  $\tau = 2n_{FP}L_\tau/c$  is the reflection delay. The mirror penetration depth will cancel when the resonant wavelength equals

the mirror center frequency, or  $\omega_m = \omega_0$ . This agrees with the TFCalc simulations as indicated in Fig. 3.21(b).

Some confusion arises in Eq. 3.13 because the propagation constant  $\beta_m$ , which is for the cavity material  $n_{FP}$ , is multiplied by the physical length  $L_\tau$ , which represents the dielectric mirror materials. It is also curious why the mirror penetration depth is given by  $L_\tau = (c\tau)/(2n_{FP})$ . When values for penetration depth are calculated as  $L_\tau = c\tau/2$  with the reflection delay  $\tau$  given by Eq. (21) in Babic and Corzine [17], they will equal the same penetration depth for N+1/2 layered pairs given by Garmire [19]. Consequently, a modified version of Eq. 3.13 is proposed:

$$2\beta_m(n_{FP}L_{FP} + 2L_\tau) - 2\omega_o\tau = 2\pi m \quad (3.14)$$

where  $\beta_m = \omega_m/c$  is the propagation constant of the  $m$ th mode and  $\tau = 2L_\tau/c$  is the reflection delay. The mirror penetration depth will still cancel when the resonant wavelength equals the mirror center frequency.

Both round-trip phase equations can be tested for accuracy by comparing them to TFCalc simulated transmission spectra. Eq. 3.13 is referred as the original round-trip phase equation, whereas Eq. 3.14 is the modified equation. These equations are practically identical when the refractive index of the cavity is air ( $n_{FP} = 1.0002$ ). Therefore, a cavity material besides air is necessary, such as water ( $n_{FP} = 1.326$ ). The simulation is designed without the dispersion of water. This is a reasonable assumption since  $dn/d\lambda = -1.5 \times 10^{-5}$  RIU nm<sup>-1</sup> for water, so over a wavelength range of 60nm the refractive index only changes by  $\Delta n = 0.0009$ . Figure 3.22 presents the simulated transmission spectra for the different cavity types. As seen in the figure, the modified round-trip phase equation better matches the simulated transmission spectra, justifying the use of Eq. 3.14.

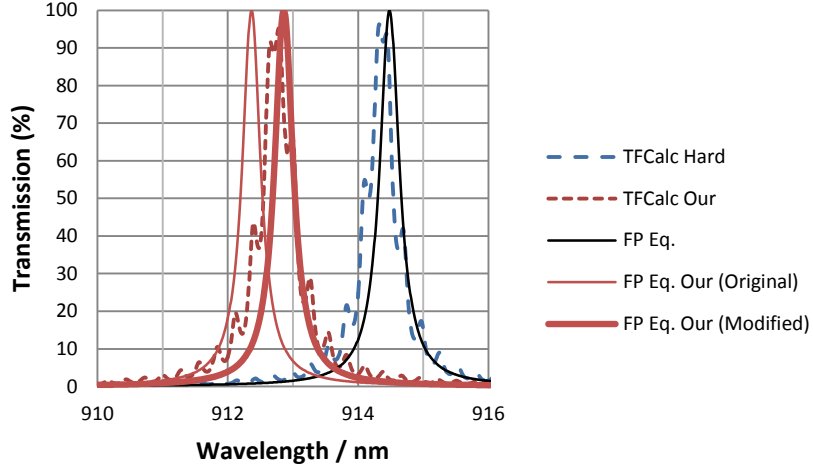


Figure 3.22 Simulated Fabry-Pérot transmission spectra and calculated transmission. Simulations utilize a 20 $\mu\text{m}$  cavity length and water ( $n_{FP} = 1.326$ ) as the medium in the cavity. The FP Eq. is with no mirror penetration, and the notation is such that (Original) is for the round-trip phase of Eq. 3.13, and (Modified) is for the round-trip phase of Eq. 3.14.

The round-trip phase can now be manipulated to calculate the cavity length and index of refraction of the cavity. From Eq. 3.14, the resulting equations are:

$$L_{FP} = \frac{m\lambda_m}{2n_{FP}} + \frac{2L_\tau}{n_{FP}} \left( \frac{\lambda_m}{\lambda_0} - 1 \right) \quad (3.15)$$

$$n_{FP} = \frac{m\lambda_m}{2L_{FP}} + \frac{2L_\tau}{L_{FP}} \left( \frac{\lambda_m}{\lambda_0} - 1 \right) \quad (3.16)$$

Both Eq. 3.15 and 3.16 demonstrate the importance that resonant modes  $\lambda_m$  of the Fabry-Pérot transmission spectra need to be considered relative to the center wavelength of the mirror to accurately calculate the cavity length or the refractive index in the cavity. In the rare case that the resonant mode equals the mirror center wavelength, there is no longer a mirror penetration depth term.

### 3.3.3 Method to obtain GRIN lens focal length

A consequence of joule heating is a non-uniform temperature distribution, which then results in a non-uniform refractive index distribution. If the spatial gradient of the refractive index distribution is significant, then a gradient index (GRIN) lens can form. The relationship of refractive index of water as a function of temperature and wavelength is addressed in Chapter 2. Considering only the peak wavelength of the experimental IR LED at 900nm, the refractive index of water is:  $n(T) = -1.2016 \times 10^{-6} T^2 + 6.1153 \times 10^{-4} T + 1.2510$ , where  $T$  is in Kelvin. This equation is entered into the temperature distribution of Fig. 3.13(a) to obtain the refractive index distribution of Fig. 3.23. One should note that PBS is necessary to create the non-uniform temperature distribution, but the relation between refractive index and temperature is for water. It is assumed that  $n(T)$  for PBS has similar coefficients for the quadratic and linear terms, and the constant term is different by about +0.15%. This difference will be addressed later in the focal length calculation.

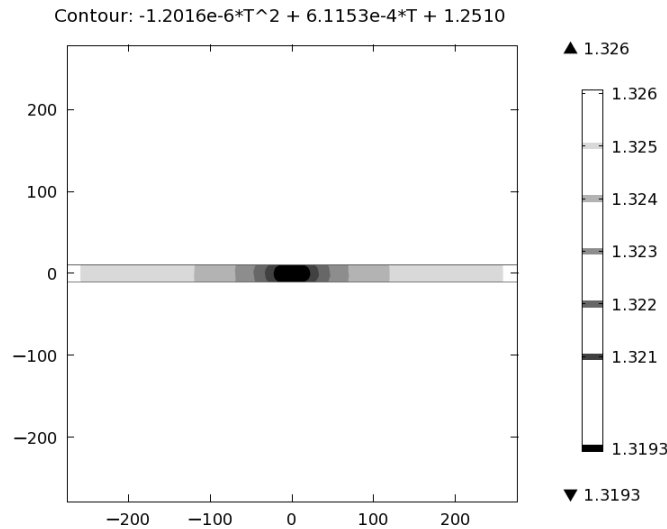


Figure 3.23 Borosilicate dipole in z-x plane using  $n(T)$  of water to obtain refractive index distribution at 900nm. The distribution should be scaled by about +0.15% for PBS.

Light from the LED propagates in the z-direction, causing the refractive index distribution to appear averaged in the z-direction and a gradient index (GRIN) to form in the x-direction. Figure 3.24 presents refractive index profile in the z-direction at x=0. Because this profile is parabolic, the average refractive index is given by:  $\bar{n}_z = n(z=0) + (1/3)[n(z = \pm L_{cav}/2) - n(z=0)]$ . The z-coordinate that corresponds to the average refractive index is  $z_{avg}$ , such that  $n(z_{avg}) = \bar{n}_z$ . This coordinate in the microfluidic channel becomes where the refractive index profile is taken in the x-direction, or  $n(x, z = z_{avg})$ . A complication arises when the microfluidic channel is an optical cavity. The ray will first propagate only in the z-direction, but then the ray will be reflected off the top mirror at some angle. Thus, this averaging method is only valid before the ray is reflected off the top mirror.

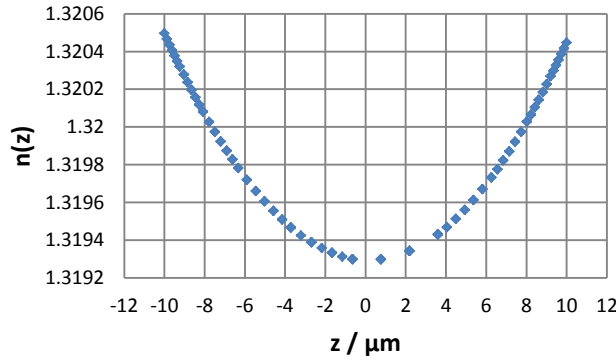


Figure 3.24 n(z) at x=0. The average of the parabola occurs at z=±6μm.

An expression is needed for  $n(x, z = z_{avg})$  in order to derive a ray matrix equation for the inhomogeneous medium in the microfluidic channel. Since the refractive index profile resulted from a simulation, the best way to obtain an expression is with a statistical fit. Pieces of the profile can be fit with elementary functions, or the entire profile can be fit with one function. The profile is separated into pieces with inflection points as provided in Fig. 3.25. Figure 3.26(a)

illustrates a parabolic fit between the inflection points, and Fig. 3.26(b) is a power fit from the inflection point to 300 $\mu\text{m}$ . Both of these elementary fits are limited over small spatial domains and do not fully describe light propagation within the refractive index profile.

The entire refractive index profile has the appearance of a negative Lorentz or Gaussian distributions. To fit these distributions,  $n(x, z = z_{avg})$  was shifted, reflected over the x-axis, and then normalized. An attempt was made to fit the profile with a Lorentz distribution using shared Matlab script. However, the tails of the Lorentz fit flattened out too soon. The entire refractive index profile was also fit with multiple Gaussian terms with Matlab's exclusive curve fitting tool. Using a sum of three Gaussian terms in the following form:

$$f_{Gauss}(x) = a_1 \exp\left(-\left(\frac{x-b_1}{c_1}\right)^2\right) + a_2 \exp\left(-\left(\frac{x-b_2}{c_2}\right)^2\right) + a_3 \exp\left(-\left(\frac{x-b_3}{c_3}\right)^2\right) \quad (3.17)$$

a fit was obtained with an R-square value of 0.9995. This fit was reflected back over the x-axis, scaled, and shifted to fit the refractive index profile. Figure 3.27 illustrates the fit  $n_{fit}(x) = -Af_{Gauss}(x) + B$  and Table 3.5 lists the fitting parameters of  $f_{Gauss}(x)$ .

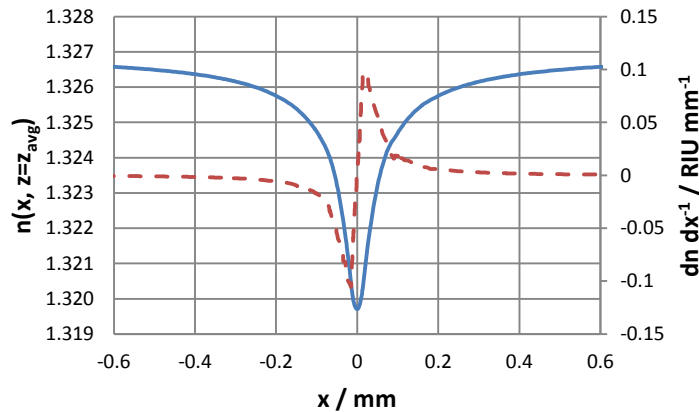


Figure 3.25 The refractive index profile (solid line) and its derivative (dashed line).

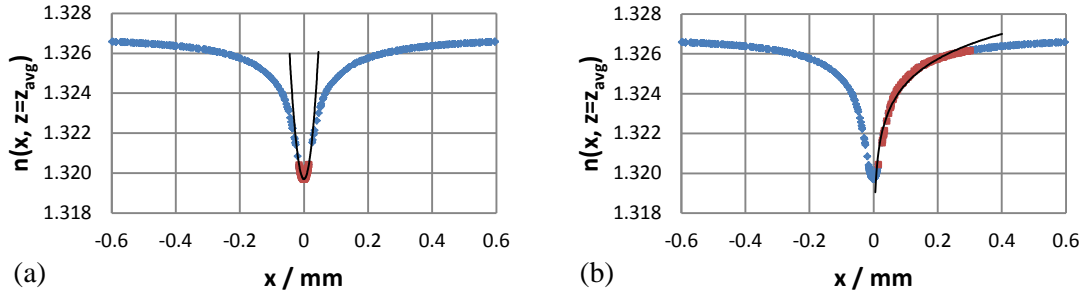


Figure 3.26 Red squares indicate fitted data using (a) parabolic fit between inflection points, and (b) power fit from inflection point to 300 $\mu$ m.

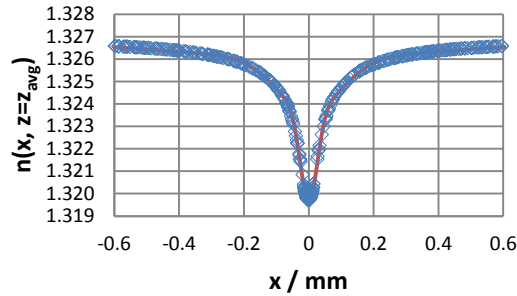


Figure 3.27 Fit of RI profile with  $n(x) = -Af_{Gauss}(x) + B$ .

Table 3.5 List of the fitting parameters for  $f_{Gauss}(x)$  provided in Eq. 3.17.

		<b>95% confidence intervals</b>
<b>a1 =</b>	0.5602	(0.5549, 0.5655)
<b>b1 =</b>	2.545e-05	(-0.0001392, 0.0001901)
<b>c1 =</b>	0.03731	(0.03692, 0.0377)
<b>a2 =</b>	0.3282	(0.3232, 0.3332)
<b>b2 =</b>	0.001219	(0.0004896, 0.001949)
<b>c2 =</b>	0.1408	(0.1387, 0.1429)
<b>a3 =</b>	0.1086	(0.1062, 0.111)
<b>b3 =</b>	-0.001042	(-0.006051, 0.003967)
<b>c3 =</b>	0.6131	(0.6036, 0.6225)

Ray propagation in an inhomogeneous medium is nicely presented by Verdeyen [20] and will be reproduced in this work. Using the paraxial ray approximation, the basic equation for the propagation of a ray in an inhomogeneous medium is the following [20]:

$$\frac{d^2 r}{dz^2} = \frac{1}{n(r)} \frac{dn(r)}{dr} \quad (3.18)$$

where  $n(r)$  is the refractive index profile with spatial coordinate  $r$ . The refractive index profile  $n_{fit}(x)$  becomes difficult to analytically solve with Eq. 3.17. Parabolic refractive index profiles are more common and easier to analytically solve, such that only the parabolic part of the refractive index profile between inflection points will be of interest going forward.

Focal length is a useful parameter to characterize a lens. The focal length with a parabolic refractive index resulting in a positive GRIN rod lens is commonly found [21, 22, 23], whereas the focal length of a negative GRIN rod lens is not often found. Additionally, focal length equations assume an interface between the rod lens and air, which is not the case for the focal length within the microfluidic channel. The focal length of a negative GRIN rod lens within the microfluidic channel will now be derived in detail. The general index distribution is sometimes seen as [22]:

$$n^2(r) = n_0^2(1 - \alpha^2 r^2) \quad (3.19)$$

Using the binomial series expansion:  $(1 - x^2)^{1/2} = 1 - (x^2/2) - (x^4/8) - (x^6/16)...$  and ignoring higher order terms, the refractive index profile for a positive lens becomes:

$$n(r) = n_0 \left( 1 - \frac{r^2}{2l^2} \right) \quad (3.20)$$

where  $\alpha = l^{-1}$ . Verdeyen claims that values of  $l$  are much larger than  $r$ , so Eq. 3.18 is determined by  $n(r) = n_0$  and the derivative is taken on  $n(r) = -n_0 r^2 / 2l^2$ . This claim will be checked in the next section. Thus, Eq. 3.18 becomes:

$$\frac{d^2 r}{dz^2} = -\frac{r}{l^2} \quad (3.21)$$

The result of this second order differential equation is:

$$r(z) = r_1 \left[ \cos\left(\frac{z}{l}\right) \right] + r_1' \left[ l \sin\left(\frac{z}{l}\right) \right] \quad (3.22)$$

where the position  $r_1$  and slope  $r_1'$  are known. With differentiation the position at any position  $z$  is obtained:

$$r'(z) = r_1 \left[ -\frac{1}{l} \sin\left(\frac{z}{l}\right) \right] + r_1' \left[ \cos\left(\frac{z}{l}\right) \right] \quad (3.23)$$

The ray matrix for the positive lens with distance  $z = d$  is:

$$\mathbf{T}_p = \begin{bmatrix} \cos\left(\frac{d}{l}\right) & l \sin\left(\frac{d}{l}\right) \\ -\frac{1}{l} \sin\left(\frac{d}{l}\right) & \cos\left(\frac{d}{l}\right) \end{bmatrix} \quad (3.24)$$

The focal length is given by the 'C' parameter, where  $f_p = -1/C$ :

$$f_p = \frac{1}{-\frac{1}{l} \sin(d/l)} = \frac{1}{\alpha \sin(\alpha l)} \quad (3.25)$$

The focal lengths of a GRIN lens often include refraction at a flat interface, such that the overall matrix is:

$$\mathbf{T}_{p\_big} = \begin{bmatrix} 1 & 0 \\ 0 & \frac{n_1}{n_2} \end{bmatrix} \begin{bmatrix} \cos\left(\frac{d}{l}\right) & l \sin\left(\frac{d}{l}\right) \\ -\frac{1}{l} \sin\left(\frac{d}{l}\right) & \cos\left(\frac{d}{l}\right) \end{bmatrix} = \begin{bmatrix} \text{(not needed)} & \text{(not needed)} \\ -\frac{n_1}{n_2} \frac{1}{l} \sin\left(\frac{d}{l}\right) & \text{(not needed)} \end{bmatrix} \quad (3.26)$$

where the initial refractive index is  $n_1 = n_0$  and the final refractive index is air, or  $n_2 = 1$ .

Therefore, the focal length is given by:

$$f_{p\_big} = \frac{1}{-\frac{n_1}{n_2} \frac{1}{l} \sin(d/l)} = \frac{1}{n_0 \alpha \sin(\alpha l)} \quad (3.27)$$

Equation 3.27 is commonly seen as the focal length of a positive GRIN lens [21, 22, 23]. Now, let  $l = iL$  so that the quadratic term of the refractive index profile becomes positive. This results in a negative GRIN lens with the following refractive index profile:

$$n(r) = n_0 \left( 1 - \frac{r^2}{2(iL)^2} \right) = n_0 \left( 1 + \frac{r^2}{2L^2} \right) \quad (3.28)$$

When  $L \rightarrow \infty$ , the refractive index profile becomes uniform. Utilizing hyperbolic functions the ray matrix for the negative lens is:

$$\mathbf{T}_n = \begin{bmatrix} \cos\left(\frac{d}{iL}\right) & \sin\left(\frac{d}{iL}\right) \\ -\frac{1}{iL} \sin\left(\frac{d}{iL}\right) & \cos\left(\frac{d}{iL}\right) \end{bmatrix} = \begin{bmatrix} \cosh\left(\frac{d}{L}\right) & L \sinh\left(\frac{d}{L}\right) \\ \frac{1}{L} \sinh\left(\frac{d}{L}\right) & \cosh\left(\frac{d}{L}\right) \end{bmatrix} \quad (3.29)$$

where  $i^{-1} = -i$ ,  $\cos(-x) = \cos(x)$ ,  $\sin(-x) = -\sin(x)$ . The focal length is given by the ‘C’ parameter, such that:

$$f_n = -\frac{1}{\frac{1}{L} \sinh(d/L)} = -\frac{1}{\alpha \sinh(d\alpha)} \quad (3.30)$$

Equations 3.25 and 3.30 will be used to calculate focal lengths in the next section.

### 3.3.4 Positive and negative GRIN lenses

Both converging (positive) and diverging (negative) gradient index lenses can be created in the microfluidic channel based on the electrode configuration. A dipole electrode configuration causes a lower refractive index between the top and bottom electrodes and changes to a higher refractive index away from the electrodes. This results in a negative GRIN lens, and was illustrated in the previous section. A positive GRIN lens is created by utilizing the phenomenon of the negative lens with a circle electrode configuration. In this case, the aperture of the circle electrodes has a higher refractive index and changes to a lower refractive index

between the electrodes. Dipole and circle electrodes are illustrated in Fig. 3.28(a) and Fig 3.28(b), respectively.

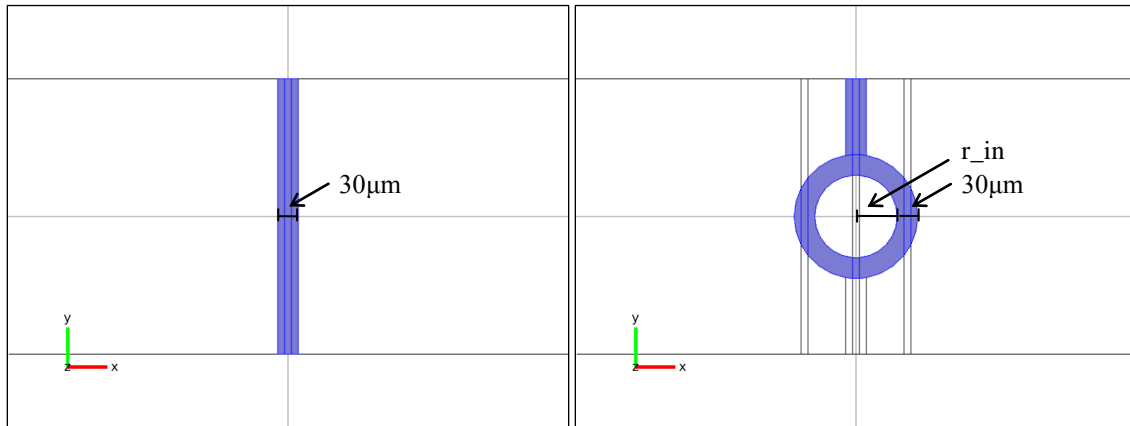


Figure 3.28 Screenshots in COMSOL Multiphysics of (a) dipole electrodes and (b) circle electrodes with inner radius  $r_{in}$ . The filled-in color represents the top electrode of the electrode pair. The additional lines in the y-direction indicate the boundary y-z planes to create boundary meshes.

Joule heating simulations with the dipole and circle electrode configurations are performed at selected applied voltages. The refractive index profile is obtained as described earlier: at a wavelength of 900nm, at the z-coordinate corresponding to the average refractive index  $z_{avg}$ , and between inflection points. Figure 3.29 presents the refractive index profile for the dipole electrodes along with fitting parameters for the polynomial  $n(x) = ax^2 + bx + c$  in Table 3.6. The linear term ‘ $b$ ’ was included because Microsoft Excel automatically uses all three terms in a 2<sup>nd</sup> order polynomial fit. The linear term is not actually part of the refractive index distributions as seen in Eq. 3.20 and Eq. 3.28, and its impact will be noted later. Furthermore, Microsoft Excel was chosen to fit the polynomial as it could fit data at the lower applied voltages. The data is repeated for the circle electrodes, as seen in Fig. 3.29 and Table 3.7.

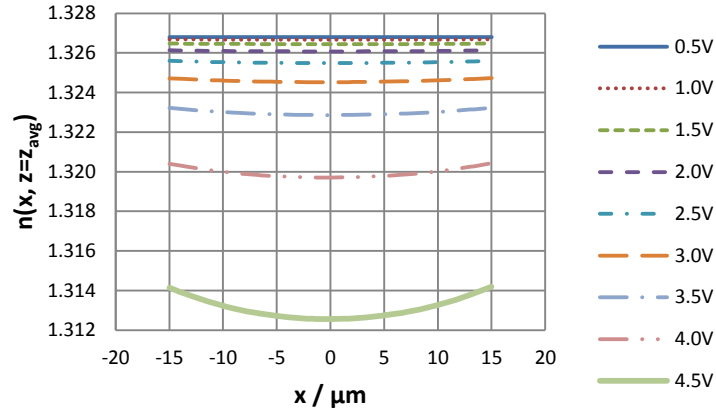


Figure 3.29 Refractive index profile between inflection points of dipole electrodes. Since the electrodes are 30μm wide, this profile is actually blocked by the opaque electrodes.

Table 3.6 Fitting parameters using  $n(x) = ax^2 + bx + c$  for dipole electrodes in Fig. 3.29.

Voltage / V <sub>rms</sub>	a / RIU mm <sup>-2</sup>	b / RIU mm <sup>-1</sup>	c / RIU	R <sup>2</sup>
<b>0.5</b>	1.1937E-2	5.0841E-6	1.3268	1.0174
<b>1.0</b>	5.0485E-2	2.1209E-5	1.3267	0.99906
<b>1.5</b>	1.2488E-1	5.1356E-5	1.3264	0.99816
<b>2.0</b>	2.5450E-1	1.0148E-4	1.3261	0.99854
<b>2.5</b>	4.7749E-1	1.8300E-4	1.3255	0.99870
<b>3.0</b>	8.7117E-1	3.1808E-4	1.3245	0.99888
<b>3.5</b>	1.6054E+0	5.5300E-4	1.3229	0.99908
<b>4.0</b>	3.1191E+0	9.9917E-4	1.3197	0.99929
<b>4.5</b>	7.1187E+0	1.9807E-3	1.3125	0.99960

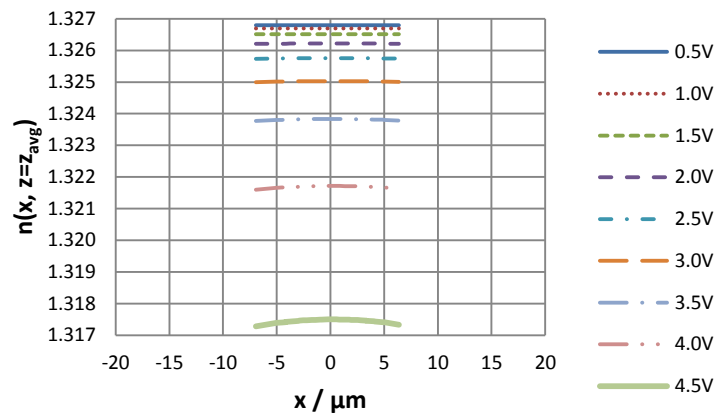


Figure 3.30 Refractive index profile between inflection points of circle electrodes with 20μm inner radius.

Table 3.7 Fitting parameters using  $n(x) = ax^2 + bx + c$  for circle electrodes in Fig. 3.30.

Voltage / $V_{rms}$	a / RIU $mm^{-2}$	b / RIU $mm^{-1}$	c / RIU	$R^2$
0.5	-1.1595E-2	4.8049E-6	1.3268	-1.4626
1.0	-4.8468E-2	2.0111E-5	1.3267	0.99134
1.5	-1.1751E-1	4.8886E-5	1.3265	0.99180
2.0	-2.3262E-1	9.7211E-5	1.3262	0.99940
2.5	-4.2007E-1	1.7690E-4	1.3258	0.99723
3.0	-7.2859E-1	3.1052E-4	1.3250	0.99765
3.5	-1.2560E+0	5.4509E-4	1.3238	0.99745
4.0	-2.2209E+0	9.8832E-4	1.3217	0.99755
4.5	-4.2581E+0	1.9413E-3	1.3175	0.99744

Focal lengths can now be calculated using the quadratic term of the fitting polynomial and the previously derived focal length equations. For the negative GRIN lens as described by Eq. 3.30, the term  $\alpha = \sqrt{2a/n_0}$ , where  $n_0$  is the minimum of the parabola. For the positive GRIN lens described by Eq. 3.25, the term  $\alpha = \sqrt{-2a/n_0}$ , where  $n_0$  is the maximum of the parabola. The value of  $n_0$  should be +0.15% larger for PBS, but this has negligible effect in calculating focal length. The fitting term ‘ $b$ ’ is ignored and its impact will be noted later on. In both focal length equations the distance is chosen to be  $d = 20\mu m$ . The resulting positive and negative focal lengths are plotted in Figure 3.31.

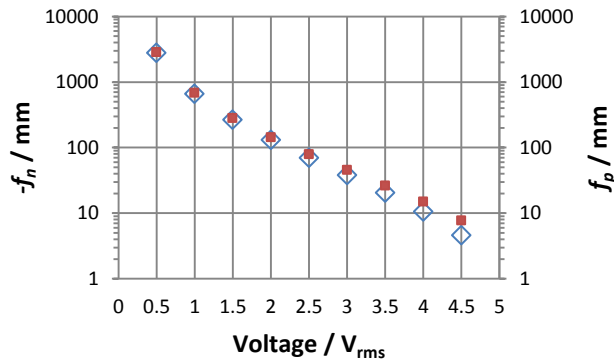


Figure 3.31 Focal length of dipole (open diamond) and circle (filled square) electrodes. The dipole electrodes result in a negative focal length as described by Eq. 3.30, and the circle electrodes with  $20\mu m$  inner radius result in a positive focal length as given by Eq. 3.25.

Joule heating simulations with circle electrode configurations are performed at selected inner radius values and a fixed applied voltage of  $4V_{\text{rms}}$ . The refractive index profile is again obtained with the following method: at a wavelength of 900nm, at the z-coordinate corresponding to the average refractive index  $z_{\text{avg}}$ , and between inflection points. Figure 3.32 presents the refractive index profile for the circle electrodes. One should note the parabola offset does not change monotonically with the inner circle radius. This is because the mesh resolution is not fine enough to keep it from being a variable within that spatial area. As mentioned in the Joule heating section, the computer has a limited computational resources and this was the best attempted mesh. Using Excel, the fitting parameters for the polynomial  $n(x) = ax^2 + bx + c$  are found in Table 3.8. Utilizing the curve fitting tool in Matlab, the fitting parameters for the custom polynomial  $n(x) = ax^2 + c$  are found in Table 3.9.

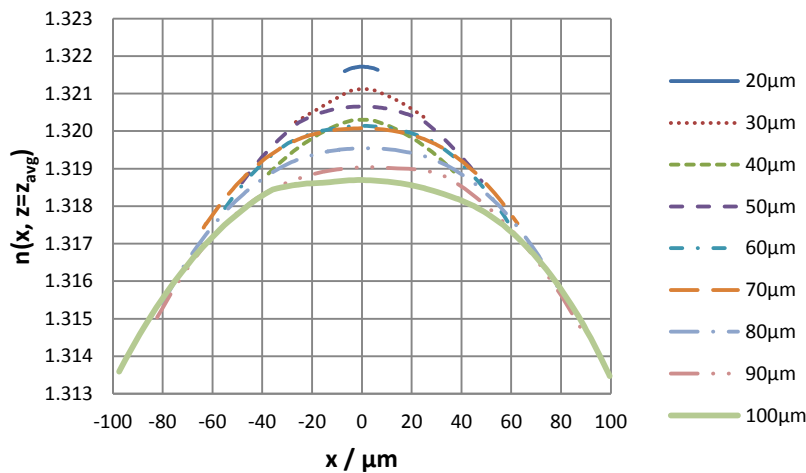


Figure 3.32 Refractive index profile between inflection points of circle electrodes for selected inner radius values.

Table 3.8 Fitting parameters of  $n(x) = ax^2 + bx + c$  for circle electrodes in Fig. 3.32.

Inner radius / $\mu\text{m}$	a / RIU $\text{mm}^{-2}$	b / RIU $\text{mm}^{-1}$	c / RIU	R <sup>2</sup>
20	-2.2209E0	9.8832E-4	1.3217	0.99755
30	-1.2452E0	1.9133E-3	1.3211	0.97959
40	-1.0349E0	3.7129E-4	1.3203	0.99523
50	-8.6349E-1	1.7265E-4	1.3207	0.99482
60	-7.1227E-1	-8.3666E-5	1.3202	0.99236
70	-6.3598E-1	1.1821E-4	1.3202	0.99441
80	-5.9970E-1	1.8759E-3	1.3196	0.99391
90	-5.5308E-1	1.7368E-3	1.3191	0.99198
100	-5.1314E-1	6.9164E-4	1.3189	0.98701

Table 3.9 Fitting parameters of  $n(x) = ax^2 + c$  for circle electrodes in Fig. 3.32. The R-square value is lower for inner radii of 20 and 30  $\mu\text{m}$  because the curve fitting tool in Matlab does not have a high enough precision for the RI data.

Inner radius / $\mu\text{m}$	a / RIU $\text{mm}^{-2}$	95% confidence intervals	c / RIU	95% confidence intervals	R <sup>2</sup>
20	-2.268	(-2.387, -2.148)	1.322	(1.322, 1.322)	0.9645
30	-1.257	(-1.335, -1.178)	1.321	(1.321, 1.321)	0.971
40	-1.036	(-1.061, -1.01)	1.32	(1.32, 1.32)	0.9948
50	-0.8634	(-0.8771, -0.8497)	1.321	(1.321, 1.321)	0.9948
60	-0.7135	(-0.7281, -0.6989)	1.32	(1.32, 1.32)	0.9925
70	-0.6367	(-0.6462, -0.6271)	1.32	(1.32, 1.32)	0.9944
80	-0.6019	(-0.6125, -0.5912)	1.32	(1.32, 1.32)	0.9896
90	-0.5603	(-0.5734, -0.5472)	1.319	(1.319, 1.319)	0.9885
100	-0.5113	(-0.5224, -0.5003)	1.319	(1.319, 1.319)	0.9864

Focal lengths from the circle electrodes are calculated using the quadratic term of the fitting polynomials  $n(x) = ax^2 + bx + c$  and  $n(x) = ax^2 + c$ . The focal length of Eq. 3.25 is then determined by the term  $\alpha = \sqrt{-2a/n_0}$ , where  $n_0$  is the maximum of the parabola. Figure 3.33 presents the focal length of the positive GRIN lens for each of the fitting polynomials. From the figure, it is implied that ignoring the 'b' term from the fit  $n(x) = ax^2 + bx + c$  has a negligible effect. The 95% confidence interval on the polynomial  $n(x) = ax^2 + c$  is also explored. Even though there are confidence intervals on both fitting terms, there is not enough arithmetic precision on the 'c' term so only the 'a' term is investigated. Figure 3.34 shows the focal length

of the positive GRIN lens for the polynomial  $n(x) = ax^2 + c$  as well as the 95% confidence intervals on the 'a' term.

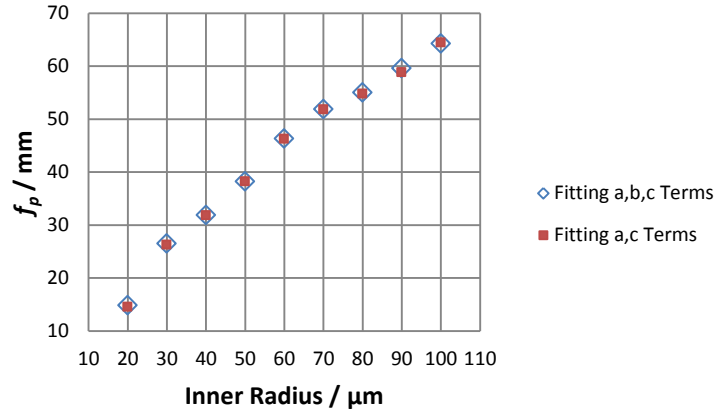


Figure 3.33 Focal length of circle electrodes at selected inner radius values. The open diamonds are from fitting the polynomial  $n(x) = ax^2 + bx + c$ , and the filled squares are from fitting the polynomial  $n(x) = ax^2 + c$ .

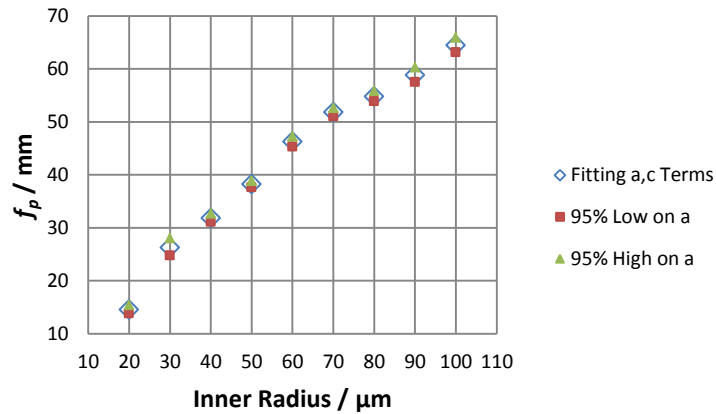


Figure 3.34 Focal length of circle electrodes at selected inner radius values. The open diamonds are from fitting the polynomial  $n(x) = ax^2 + c$ , the filled squares are based on the lower 95% confidence level on term 'a', and the filled triangles are based on the upper 95% confidence level on term 'a'.

### 3.3.5 Cavity stability with GRIN lenses

The stability of an optical cavity depends on the mirror geometry and whether there are any lenses inside of the cavity. Ray tracing provides a simple tool to analyze the stability. If the ray stays “close” to the optical axis after many transits between the mirrors, it is stable. If the ray “walks off” one of the mirror surfaces, then the cavity is unstable. If the mirrors are perfectly aligned to keep the ray near the axis, then it is conditionally stable. Cavity stability is determined by constructing an equivalent lens-waveguide. The equivalent of the cavity mirrors are lenses, and the equivalent of a lens inside a cavity is also a lens. The lens-waveguide is then made of an infinite sequence of lenses that redirect the ray in the same manner as the cavity. A unit cell is the spatial distance before the sequence of lenses repeats itself.

The stability of both positive and negative gradient index lenses in an optical cavity is presented in Table 3.10. An optical cavity is stable for the following condition:  $0 \leq (A + D + 2)/4 \leq 1$ , where  $A$  and  $D$  are from the ABCD matrix of the unit cell. Both of the gradient lenses are conditionally stable with a uniform refractive index distribution. The positive GRIN lens is also conditionally stable for  $2d/l = n\pi$ , where  $n$  is odd multiples. This arises during the confocal optical cavity case. The negative GRIN lens is not stable for any values of  $2d/l$  besides when it is conditionally stable.

Table 3.10 Positive and negative GRIN lens summary.

	Negative GRIN Lens	Positive GRIN Lens
Unit cell:		
RI profile:	$n(r) = n_0 \left( 1 + \frac{r^2}{2L^2} \right)$	$n(r) = n_0 \left( 1 - \frac{r^2}{2l^2} \right)$
Unit cell matrix:	$\begin{bmatrix} \cosh\left(\frac{2d}{L}\right) & L \sinh\left(\frac{2d}{L}\right) \\ \frac{1}{L} \sinh\left(\frac{2d}{L}\right) & \cosh\left(\frac{2d}{L}\right) \end{bmatrix}$	$\begin{bmatrix} \cos\left(\frac{2d}{l}\right) & l \sin\left(\frac{2d}{l}\right) \\ -\frac{1}{l} \sin\left(\frac{2d}{l}\right) & \cos\left(\frac{2d}{l}\right) \end{bmatrix}$
Stability: $S = \frac{A + D + 2}{4}$	$S = \frac{1}{2} \left\{ \cosh\left(\frac{2d}{L}\right) + 1 \right\}$	$S = \frac{1}{2} \left\{ \cos\left(\frac{2d}{l}\right) + 1 \right\}$
Conditionally stable when:	$L \rightarrow \infty$ (uniform RI), then $S = 1$	$l \rightarrow \infty$ (uniform RI), then $S = 1$ $2d/l = m\pi, m = 0, 2, 4, \dots$ then $S = 1$ $2d/l = m\pi, m = 1, 3, 5, \dots$ then $S = 0$ . This is the confocal optical cavity case.
Stable when: $0 \leq S \leq 1$	Besides being conditionally stable when $L \rightarrow \infty$ , cavity is not stable for any values of $2d/L$	Besides being conditionally stable when $l \rightarrow \infty$ , or $2d/l = m\pi$ , the cavity is stable

An analytic problem arises with instability. The accuracy of Gaussian beam theory degenerates rapidly as one approaches the edges of the stability diagram, and is totally inapplicable in the unstable regime [20]. Consequently, the optofluidic intracavity spectroscopy (OFIS) method for analyzing biological cells becomes complicated when electrodes are used to trap the cell with DEP forces. The resulting gradient index lenses and optical cavity stability needs to be considered while analyzing the cell with Gaussian theory.

## References

- [1] A. Ramos, H. Morgan, N.G. Green, and A. Castellanos, "Ac electrokinetics: a review of forces in microelectrode structures," *J. Phys. D: Appl. Phys.* vol. 31, no. 18, pp. 2338-2352, 1998.
- [2] G. H. Markx and C. L. Davey, "The dielectric properties of biological cells at radiofrequencies: applications in biotechnology," *Enzyme and Microbial Technology*, vol. 25, no. 3-5, pp. 161-171, 1999.
- [3] L. A. MacQueen, M. D. Buschmann, and M. R. Wertheimer, "Gene delivery by electroporation after dielectrophoretic positioning of cells in a non-uniform electric field," *Bioelectrochemistry*, vol. 72, no. 2, pp. 141-148, 2008.
- [4] W. J. Ellison, "Permittivity of pure water, at standard atmospheric pressure, over the frequency range 0-25 THz and the temperature range 0-100°C," *J. Phys. Chem. Ref Data*, vol. 36, no. 1, pp.1-18, 2007.
- [5] <http://www.technicalglass.co.uk/pdf/borosilicate-glass.pdf>
- [6] <http://www.matweb.com/search/DataSheet.aspx?MatGUID=7546f96147b847a5ab00091f3c36b8ce&ckck=1>
- [7] A. Rosenthal and J. Voldman, "Dielectrophoretic traps for single-particle patterning," *Biophysical Journal*, vol. 88, no. 8, pp. 2193-2205, Mar. 2005.
- [8] X. He and J. C. Bischof, "The kinetics of thermal injury in human renal carcinoma cells," *Annals of Biomedical Engineering*, vol. 33, no. 4, pp. 502-510, May 2005.

- [9] U. Seger-Sauli, M. Panayiotou, S. Schnydrig, M. Jordan, and P. Renaud, "Temperature measurements in microfluidic systems: heat dissipation of negative dielectrophoresis barriers," *Electrophoresis*, vol. 26, no. 11, pp. 2239-2246, 2005.
- [10] T. Schnelle, T. Müller, G. Gradl, S. G. Shirley, G. Fuhr, "Paired microelectrode system: dielectrophoretic particle sorting and force calibration," *Journal of Electrostatics*, vol. 47, no. 3, pp. 121-132, 1999.
- [11] M. S. Jaeger, T. Mueller, and T. Schnelle, "Thermometry in dielectrophoresis chips for contact-free cell handling," *Journal of Physics D: Applied Physics*, vol. 40, no. 1, pp. 95-105, Jan. 2007.
- [12] <http://www.technicalglass.co.uk/pdf/sapphire.pdf>
- [13] [http://global.kyocera.com/prdct/fc/product/pdf/s\\_c\\_sapphire.pdf](http://global.kyocera.com/prdct/fc/product/pdf/s_c_sapphire.pdf)
- [14] <http://www.microchem.com/pdf/SU-8-table-of-properties.pdf>
- [15] <http://www.microchem.com/pdf/SU-8%203000%20Data%20Sheet.pdf>
- [16] T. Sikanen, "SU-8-Based Microchips for Capillary Electrophoresis and Electrospray Ionization Mass Spectrometry," Academic dissertation, Univ. of Helsinki, Finland, p. 44, 2007.
- [17] D. I. Babic, and S. W. Corzine, "Analytic expressions for the reflection delay penetration depth, and absorptance of quarter-wave dielectric mirrors," *IEEE Journal of Quantum Electronics*, vol. 28, no. 2, pp. 514-524, 1992.
- [18] E. Hecht, *Optics*, 4th ed. Addison Wesley, 2001.
- [19] E. Garmire, "Theory of a quarter-wave-stack dielectric mirrors used in a thin Fabry-Perot filter," *Applied Optics*, vol. 42, no. 27, pp. 5442-5449, 2003.

[20] J. T. Verdeyen, *Laser Electronics*, 2nd ed. Englewood Cliffs, NJ: Prentice-Hall, 1989.

[21] M. J. Riedl, *Optical Design Fundamentals for Infrared Systems*, 2nd ed. Bellingham, WA: SPIE Press, 2001, pp. 95-97.

[22] S. Sinzinger and J. Jahns, *Microoptics*, Weinheim: Wiley-VCH, 1999, pp. 104-108.

[23] N. F. Borrelli, *Microoptics Technology*, 2nd ed. New York, NY: Marcel Dekker, 2005, pp. 69-110.

## Chapter 4: Materials and methods

This chapter provides the materials and methods used for experimental work on the optofluidic intracavity spectroscopy (OFIS) chip. The general sections of this chapter include the OFIS chip and details of the experimental methods. Many different methods were implemented, as one observation led to the design of other experiments. First, a concern was raised that joule heating caused by the DEP electrodes was reducing the cell viability. An experimental observation was also made around the same time in which energizing the electrodes causes the resonant wavelengths near the electrodes to blue-shift. The shift to lower wavelengths is consistent with the phenomenon that water at higher temperatures will have a lower index of refraction, which lowers the resonant wavelengths.

An idea was then proposed that the OFIS chip could be used for optical thermometry. The optical thermometry method is quantitative only when the refractive index is known for a given temperature. This  $n(T)$  relationship is already well-known for water, but needs to be known for phosphate buffered saline (PBS) as it is the solution used with our biological cells. However, also measuring the  $n(T)$  relationship of water and comparing it to the known relationships will help to determine how good the optical thermometer is. To determine the refractive index as a function of temperature, an isothermal apparatus was built to control the temperature of the OFIS chip. The accuracy of the optical thermometry method is further improved by considering the wavelength dependence, or  $n(T,\lambda)$ .

### 4.1 OFIS chip

The OFIS chip is created by combining a microfluidic channel with Fabry-Perot interferometer. The microfluidic channel is formed in SU-8 with cross-sectional dimensions of 200-400 $\mu\text{m}$  wide by 20-25 $\mu\text{m}$  tall. The top and the bottom of the microfluidic channel consist of

1mm thick pieces of glass with dielectric mirrors. Glass pieces are either borosilicate or sapphire. The mirrors, facing in towards the microfluidic channel, form the interferometer. The mirrors are fabricated by multiple thin layers of quarter-wavelength material. One should note there are sometimes no mirrors on the chip, for the case that only a microfluidic channel is needed and optical interferometry is not necessary.

Gold electrodes are deposited onto the mirrors or directly onto the glass if there are no mirrors. These electrodes are designed with different configurations as mentioned in the modeling chapter and are used to create dielectrophoretic forces on biological cells. At each end of the microfluidic channel, a hole is drilled to create the inlet and outlet. Nanoports are attached with crystal bond to the inlet and sometimes to the outlet in order to connect with a nanotube. Nanotubes can easily connect with a syringe, which contains the fluid of interest. Figure 4.1 illustrates a typical OFIS chip.

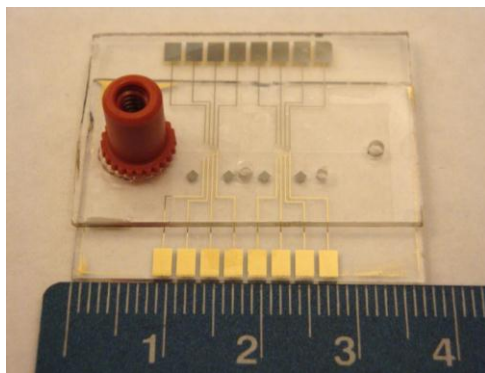


Figure 4.1 An OFIS chip next to a ruler numbered in centimeters.

In order to connect the electrodes with a function generator, a card-edge connector typically used for PC boards is implemented. This works out nicely because the PCB thickness dimension is usually 0.062" (1.57mm) and can accommodate the 1mm thick piece of glass while maintaining electrical connection. Wires are soldered onto the card-edge connector's outside

pins that connect with the AC source. Figure 4.2 shows the connection made with the OFIS chip as well as the binder clip used to hold the card-edge connector to the microscope stage.

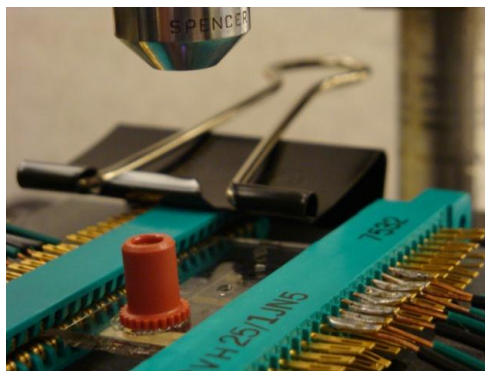


Figure 4.2 The OFIS chip with electrical connections made using the card-edge connectors.

## 4.2 Experimental methods

In this section, the methods for all experimental work are described. The first three sections are necessary for refractive measurements with both the isothermal apparatus and joule heating temperature sources. Section 4.2.4 is used for obtaining the refractive index with the isothermal apparatus, whereas Section 4.2.5 is needed to obtain refractive index measurements with joule heating.

### 4.2.1 Transmission spectrum collection

Fabry-Perot (FP) transmission spectrum is collected by illuminating the OFIS chip from the bottom by a high power infrared LED centered at 900nm. The interest in near-infrared wavelengths is because they are within the optical window of biological tissue and fluids. Transmitted light is collected by a 3X microscope objective lens focused on a 62.5 $\mu$ m core diameter multimode optical fiber. The lens and the fiber act as a spatial filter in the object plane, so optical information collected by the fiber is only from a spot approximately 21 $\mu$ m in diameter. A spectrometer alignment LED is used to back-light the fiber and reflect off the mirrors to align

where the FP spectrum is spatially collected. The OFIS system apparatus is seen in Fig. 4.3. A typical FP transmission spectrum is presented in Fig. 4.4, where the multiple peaks are the resonant wavelengths of the optical cavity. The peak wavelengths are found with a custom made Microsoft Excel program that uses a full-width at half-max method to avoid noise around the peak maximums.

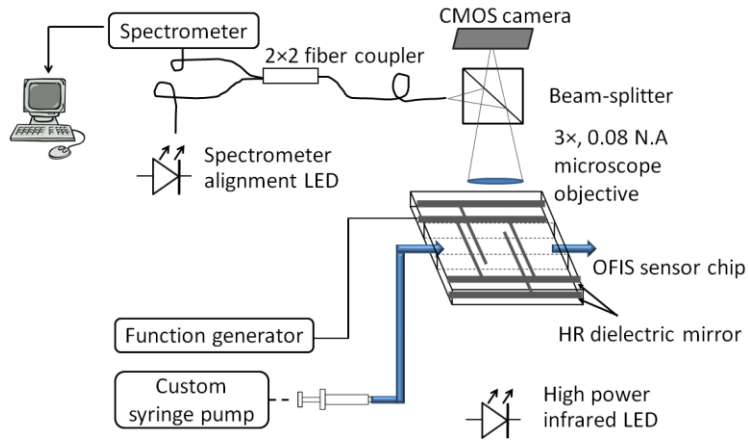


Figure 4.3 OFIS system apparatus.

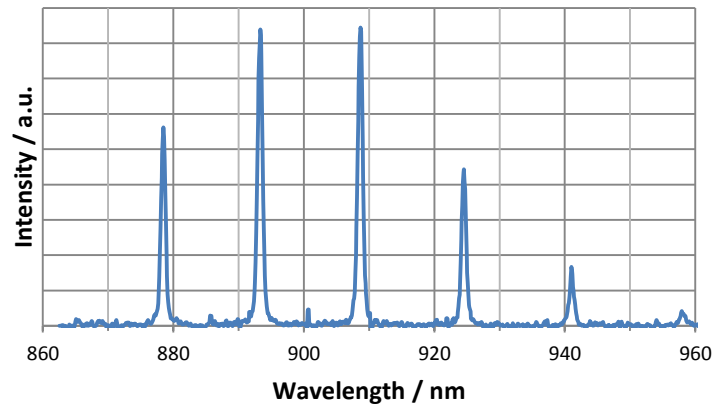


Figure 4.4 Typical FP transmission spectra.

#### 4.2.2 Mirror penetration depth consideration

Phase penetration into the mirrors needs to be considered when determining the optical path length of the cavity [1, 2]. The sum of phase terms in the cavity round-trip is provided by Eq. (28) in [1], modified here as discussed in Chapter 3:

$$2\beta_m(n_{FP}L_{FP} + 2L_\tau) - 2\omega_o\tau = 2\pi m \quad (4.1)$$

where  $\beta_m = \omega_m/c$  is the propagation constant of the  $m$ th mode,  $L_{FP}$  is the cavity length,  $L_\tau$  is the mirror penetration depth,  $\omega_o$  is the mirror center frequency, and  $\tau = 2L_\tau/c$  is the reflection delay. Solving Eq. 4.1 in terms of the cavity length and the refractive index of the cavity:

$$L_{FP} = \frac{m\lambda_m}{2n_{FP}} + \frac{2L_\tau}{n_{FP}} \left( \frac{\lambda_m}{\lambda_o} - 1 \right) \quad (4.2)$$

$$n_{FP} = \frac{m\lambda_m}{2L_{FP}} + \frac{2L_\tau}{L_{FP}} \left( \frac{\lambda_m}{\lambda_o} - 1 \right) \quad (4.3)$$

One observation is the mirror penetration term cancels when the resonant wavelength is equal to the center wavelength of the mirror. The cavity penetration depth for a mirror with an odd number of layers is provided by Eq. (36) in [2] and is reproduced here:

$$L_\tau = \frac{\left[ 1 - \frac{n_1 n_2}{n_f^2} \left( \frac{n_1}{n_2} \right)^{2(N+1/2)} \right] \left[ 1 - \left( \frac{n_1}{n_2} \right)^{2(N+1/2)} \right] \left[ \frac{n_1 n_2}{n_{FP} (n_2 - n_1)} \frac{\lambda_o}{4} \right]}{1 - \left( \frac{n_2 n_1}{n_f n_{FP}} \right)^2 \left( \frac{n_1}{n_2} \right)^{4(N+1/2)}} \quad (4.4)$$

where  $n_1$  and  $n_2$  are the refractive indices of the alternating QWS layers,  $N$  is the number of layer pairs,  $n_f$  is the refractive index of the glass,  $n_{FP}$  is the refractive index inside the FP cavity, and  $\lambda_o$  is the center wavelength of the mirror. Garmire notes [2] that “for  $N+1/2$  layer pairs the last layer will have a refractive index  $n_1$ .” A self-dependency arises because Eq. 4.3 is a function of

the mirror penetration depth  $L_\tau$ , which itself depends on the refractive index  $n_{FP}$ . Eq. 4.3 is manipulated in Appendix A.5 to solve for refractive index in the cavity, resulting in a cubic function with the form:  $0 = a_1 n_{FP}^3 + a_2 n_{FP}^2 + a_3 n_{FP} + a_4$ . A linear assumption can be made for  $n_{FP}$  on the range between 1 and 2 such that the cubic and quadratic terms are dropped. The cavity length and the refractive index of the cavity with mirror penetration become:

$$L_{FP} = \frac{m\lambda_m}{2n_{FP}} + \left[ \frac{2A \left( \frac{\lambda_0}{\lambda_m} - 1 \right)}{n_{FP}^2 - B \left( \frac{n_2 n_1}{n_f} \right)^2} \right] \quad (4.5)$$

$$n_{FP} = \frac{\frac{1}{2} m \lambda_m B \left( \frac{n_2 n_1}{n_f} \right)^2}{L_{FP} B \left( \frac{n_2 n_1}{n_f} \right)^2 + 2A \left( \frac{\lambda_m}{\lambda_0} - 1 \right)} \quad (4.6)$$

where:

$$A = \left[ 1 - \frac{n_1 n_2}{n_f^2} \left( \frac{n_1}{n_2} \right)^{2(N+1/2)} \right] \left[ 1 - \left( \frac{n_1}{n_2} \right)^{2(N+1/2)} \right] \left[ \frac{n_1 n_2}{(n_2 - n_1)} \frac{\lambda_0}{4} \right] \quad (4.7)$$

$$B = \left( \frac{n_1}{n_2} \right)^{4(N+1/2)} \quad (4.8)$$

When the resonant wavelength is equal to the center wavelength of the mirror, Eq. 4.5 reduces to  $L_{FP} = m\lambda_m / 2n_{FP}$  and Eq. 4.6 reduces to  $n_{FP} = m\lambda_m / 2L_{FP}$ . Both Eq. 4.5 and 4.6 are necessary since resonant modes  $\lambda_m$  need to be considered relative to the center wavelength of the mirror.

The composition of the dielectric mirrors depends on whether borosilicate or sapphire glass is being used. If the chip is made with borosilicate glass, the mirrors are deposited by a

commercial vendor and consist of alternating layers of SiO<sub>2</sub> and HfO<sub>2</sub>. For chips made with sapphire glass, the mirrors are deposited in-house and consist of alternating layers of SiO<sub>2</sub> and SiN<sub>x</sub>. Due to the higher quality of the vendor mirror, only it will be used as the experimental mirror.

The parameters for the vendor mirrors are given by  $N = 6$  pairs,  $n_1 = 1.889$  for HfO<sub>2</sub>,  $n_2 = 1.452$  for SiO<sub>2</sub>, and  $n_f = 1.452$  for the borosilicate glass that is composed mostly of silica. HfO<sub>2</sub> is the first and last layer in order to maximize the reflectivity of 96%. The center wavelength of the mirror is  $\lambda_0 = 880\text{nm}$  as mentioned in Chapter 3. One concern is the center wavelength of a QWS mirror is temperature dependent as observed by Dudley *et al.* [3]. However, our values for SiO<sub>2</sub>/HfO<sub>2</sub> result in a maximum shift of  $\Delta\lambda_0 = 0.4\text{nm}$  over a temperature range of  $\Delta T = 40^\circ\text{C}$ . This shift results in a negligible change in both Eq. 4.5 and Eq. 4.6 when added to  $\lambda_0$ .

### 4.2.3 Cavity length interpolation

The resonant modes of the spectrum are determined by the optical path length inside the optofluidic cavity, or the product of the physical length and refractive index. Consequently, refractive index needs to be distinguished from cavity length. The idea presented in this work is that cavity length can be measured in multiple air pockets outside the microfluidic channel, and then cavity length is interpolated versus spatial position in one dimension to determine the cavity length within the microfluidic channel. The advantage of using air pockets is the RI of air is well known, is non-dispersive, and negligibly changes with temperature. Air pockets are used on each side of the microfluidic channel and are seen in Fig. 4.5. Electrodes on the top and bottom of the channel are useful for aligning spatial locations in the microfluidic channel with the air pockets, though were not energized in the isothermal experiments.

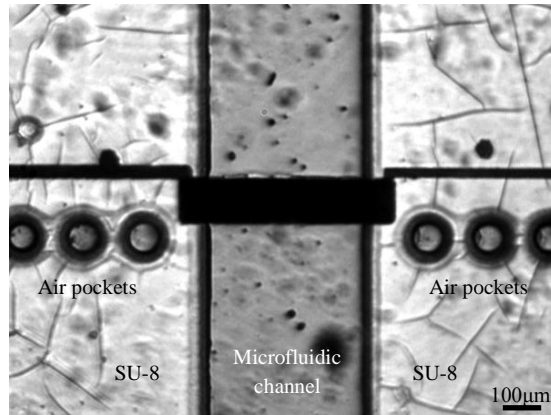


Figure 4.5 Microscope image where a microfluidic channel has been developed in SU-8. Air pockets are on either side of the channel, and a pair of top and bottom electrodes is used to help align spatial locations in the microfluidic channel with the air pockets.

An overview of the algorithm to compute the refractive index in the microfluidic channel is presented in Fig. 4.6. The method is indeed complicated compared to commercial refractometers. However, this method allows one to calculate refractive index in a microfluidic channel with a spatial resolution of  $21\mu\text{m}$  and obtain wavelength dependence. The process begins by acquiring spectral data in the air pockets as well as in 3 locations in the microfluidic channel. Next, the cavity length is calculated for each resonant wavelength by choosing sequential mode integers  $m$  that minimize the standard deviation of Eq. 4.5. The cavity length for one air hole is calculated by averaging the cavity lengths of each resonant wavelength. A second-order polynomial fits the averaged cavity length of all the air pockets and is interpolated versus position in order to determine the cavity length within the microfluidic channel. With knowledge of the cavity length, the index of refraction in the microfluidic channel is then determined for each resonant wavelength by choosing sequential mode integers  $m$  that minimize the standard deviation of Eq. 4.6.

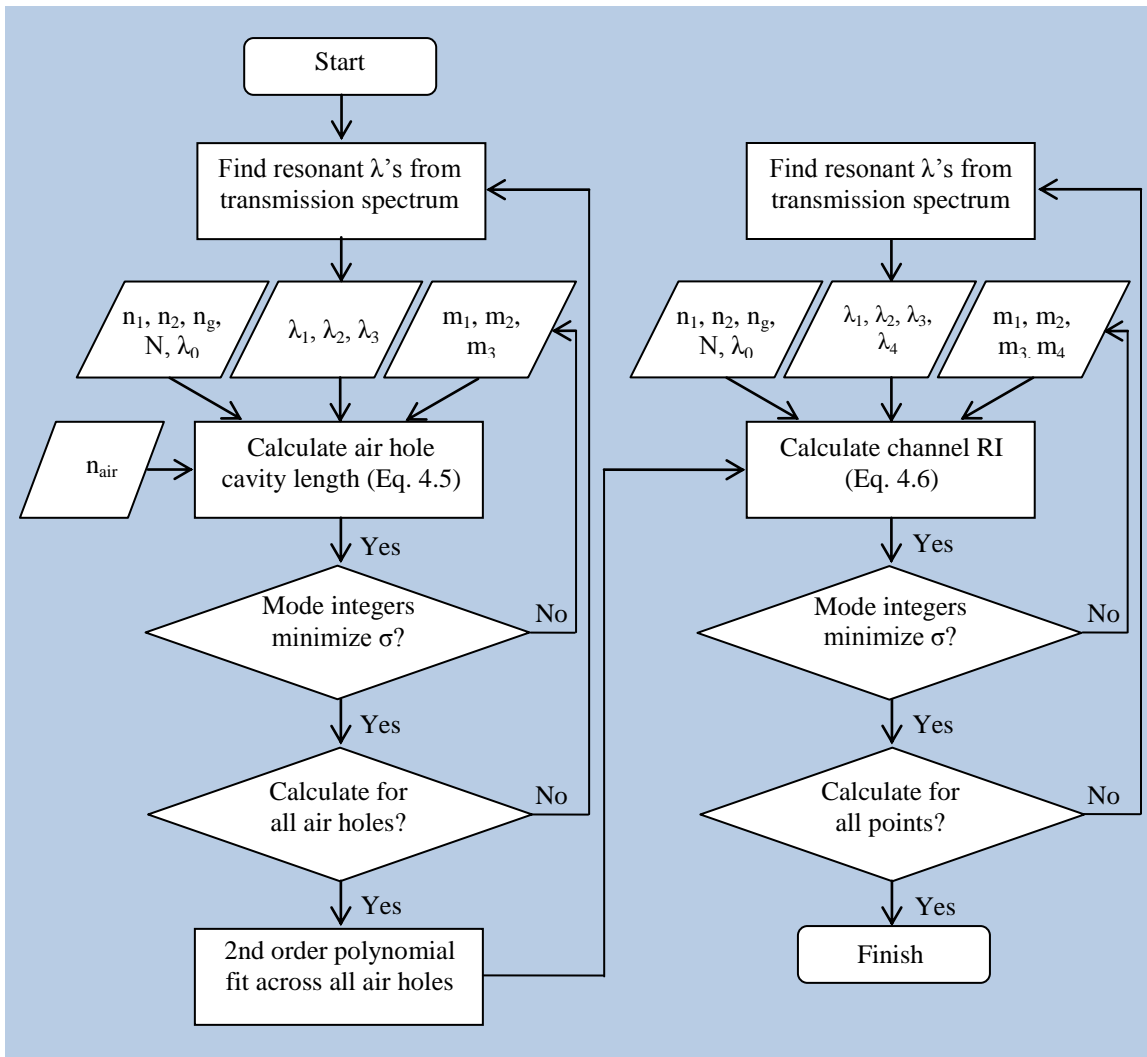


Figure 4.6 Data processing algorithm to compute refractive index in the microfluidic channel.

#### 4.2.4 Refractive index measurements with isothermal apparatus

An isothermal apparatus is needed to find the temperature dependence of refractive index. A diagram of the custom-built apparatus is illustrated in Fig. 4.7 and a picture is seen in Fig. 4.8. The OFIS chip was submerged in a water box connected to a circulating water bath. Nanotubes are connected from the microfluidic channel to outside of the water box, such that no bath water will enter the microfluidic channel. Furthermore, silicone sealant is placed around the nanoports to help prevent water from entering the channel. The plastic water box has a valve on

the outlet that allows the volume of the water to be controlled within the box. A partial lid covers the water box in order for air bubbles to escape while keeping the surface of the water smooth within the microscope field of view. The temperature of the water is controlled on the circulating water bath and is measured by three thermometers inserted into the plastic box. Before measuring the spectra within the cavity, the temperature in the box is waited to stabilize, allowing the OFIS chip to reach thermal equilibrium.

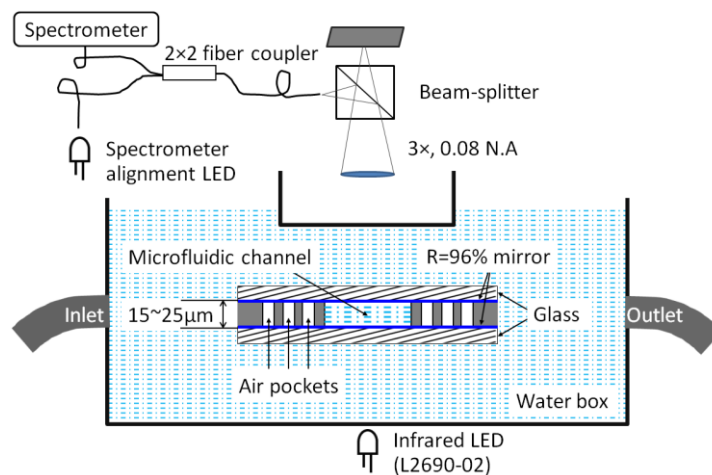


Figure 4.7 Cross-sectional diagram of the OFIS chip submerged in a custom-built isothermal apparatus and the optics to measure the FP spectra.

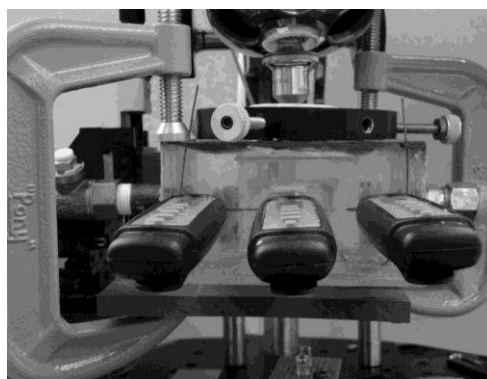


Figure 4.8 Picture of the OFIS chip submerged in the isothermal apparatus.

#### **4.2.5 Refractive index measurements with joule heating**

The combination of energizing the electrodes and the high electrical conductivity solution PBS results in joule heating. Electrodes are energized by applying an AC sinusoidal signal with a HP 8116A Pulse/Function Generator to the wires on the card-edge connector, seen in Fig. 4.2. All electrical signals were at 50MHz and various voltage magnitudes were applied. In these experiments, fluid in the microfluidic channel was not flowing or nearly stagnant. It turns out that liquid cooling can be neglected for a fluid velocity approaching  $1\text{mm s}^{-1}$  because of the small dimensions [4].

## References

- [1] D. I. Babic, and S. W. Corzine, “Analytic expressions for the reflection delay penetration depth, and absorptance of quarter-wave dielectric mirrors,” *IEEE Journal of Quantum Electronics*, vol. 28, no. 2, pp. 514-524, 1992.
- [2] E. Garmire, “Theory of a quarter-wave-stack dielectric mirrors used in a thin Fabry-Perot filter,” *Applied Optics*, vol. 42, no. 27, pp. 5442-5449, 2003.
- [3] J. J. Dudley, D. L. Crawford, and J. E. Bowers, “Temperature dependence of the properties of DBR mirrors used in surface normal optoelectronic devices,” *IEEE Photonics Technology Letters*, vol. 4 no. 4, pp. 311-314, 1992.
- [4] A. Ramos, H. Morgan, N.G. Green, and A. Castellanos, “Ac electrokinetics: a review of forces in microelectrode structures,” *J. Phys. D: Appl. Phys.* vol. 31, no. 18, pp. 2338-2352, 1998.

## **Chapter 5: Experimental results**

In this chapter, experimental results are presented based on the materials and methods described in Chapter 4. Many experiments were performed, and can be grouped into categories: (1) cavity length interpolation observations, (2) RI measurements with isothermal apparatus, (3) RI measurements with joule heating, and (4) GRIN lens imaging. In the first three categories, the data is based on the resonant wavelengths of the Fabry-Pérot cavity. The data is then processed to be either a cavity length measurement or a refractive index measurement. In the fourth category, data is obtained by images and then quantified with pixel intensity. The major sections in this chapter will be the same as the above categories.

One point to make early is how the experiments were documented. The spectra software automatically provides information within the digital spectrum file, including the date and time of when the spectrum is saved, as well as the integration time. Furthermore, experimental files were organized carefully in digital files labeled by their respective OFIS chip name. The OFIS chips are named by the date the chip was fabricated (done by other students). A table listing all of the experiments is presented in Appendix C.3, which includes the date of the experiment, the experiment number, the name of the chip, and other comments.

### **5.1 Cavity length interpolation observations**

#### **5.1.1 Position, size, and number of air holes**

The position and size of the air holes for the cavity length interpolation needed to be determined. Intuition provides the thought that the closer air pockets are to the microfluidic channel, the more accurate the interpolation will be inside the channel. Next, the air holes need to be wide enough to fit the spectra spot diameter of  $21\mu\text{m}$ , as well as wide enough so that SU-8

or UV-glue will not fill in the air holes during fabrication. The first SU-8 photolithography mask contained air holes with different diameters. It was discovered the air holes need to be at least 100 $\mu\text{m}$  in diameter on the photolithography mask so the air holes will not be filled in. The center-to-center distance between air holes was chosen to be 150 $\mu\text{m}$  on the basis that it provided a comfortable enough distance. With the same reasoning, the distance between the center of the air hole closest to the channel and the edge of the channel was chosen to be 150 $\mu\text{m}$ .

Along with position and size, the number of the air holes needs to be determined for the cavity length interpolation. Intuitively, the more air holes there are, the better the interpolation accuracy will be. A quantity of six air holes on each side of the channel was arbitrarily chosen. However, a few discoveries were made during the experimental work. The first was the air holes next to the channel on either side did not fit a 2<sup>nd</sup> order polynomial interpolation very well as seen in Fig. 5.1. These two air holes are the most important to fit accurately.

The second discovery was that a 4<sup>th</sup> order polynomial did fit the air holes next to the channel, but then refractive index was not consistent at multiple points in the microfluidic channel. The refractive index at multiple points was consistent when a 2<sup>nd</sup> order polynomial was fit with three air holes on each side of the microfluidic channel. Even though two air holes on each side of the microfluidic channel are possible for a 2<sup>nd</sup> order fit, it is recommended to use three to allow for the possibility of an air hole optically blocked with debris (any air hole) or being filled with water (for air holes nearest the channel). Thus, three air holes on each side of the channel is the empirically determined choice.

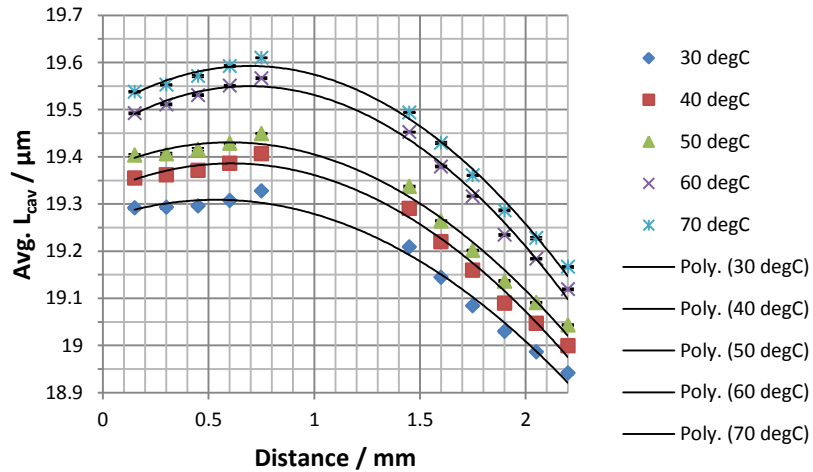


Figure 5.1 DI Water Chip 20-Aug-2011. The microfluidic channel is between the distances of 0.8mm and 1.4mm. Six air holes are measured on one side of the microfluidic channel, and five air holes are measured on the other side as one of the air holes was obstructed. The 2<sup>nd</sup> order polynomials do not fit the air holes closest to the microfluidic channel, which are the points that are most important to fit.

### 5.1.2 Air hole dynamics

Figure 5.1 generates curiosity as to why the air holes next to the microfluidic channel have a relatively larger cavity length. One way to explore this question is to measure the temporal response of the air holes. Experiments were performed at room temperature in which fluid was kept in the microfluidic channel and cavity length measurements were taken over time. Water and PBS were tested and produced similar results, but data was collected for PBS at more time intervals such that only it will be presented. Figure 5.2 is the dynamic cavity length for an air pocket next to the microfluidic channel. At time intervals of 0, 3, and 24 hrs, the cavity length was measured in all air pockets and is seen in Fig. 5.3. The cavity length was also measured in the microfluidic channel at 0 and 24 hrs when there was no fluid. This acts as a calibration method of the interpolation fit.

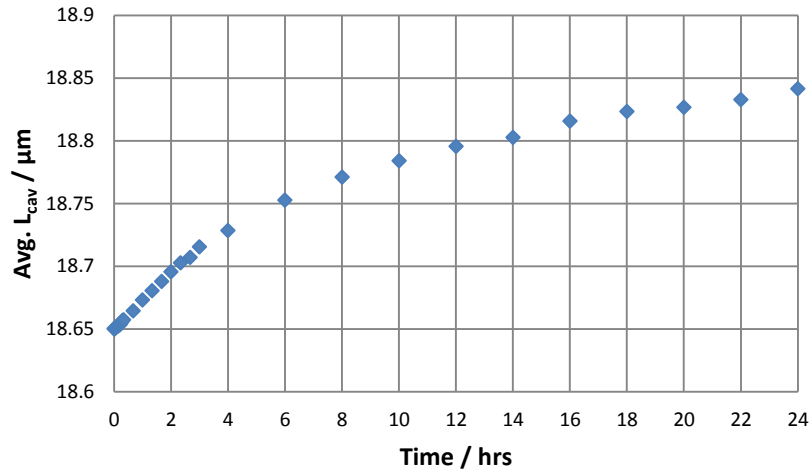


Figure 5.2 PBS for Chip 05-Apr-2011, air hole next to channel vs. time.

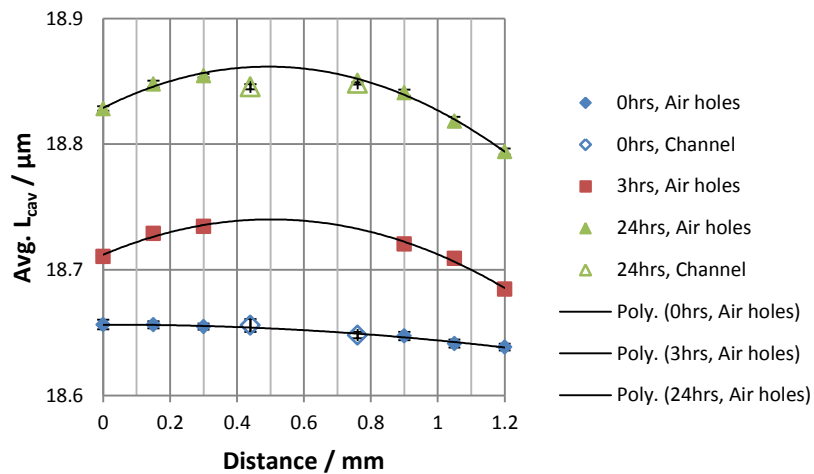


Figure 5.3 PBS for Chip 05-Apr-2011, profile vs. time.

### 5.1.3 Hypotheses for air hole dynamics

The only thing that is changing during the room temperature measurements is that water or PBS is entering the microfluidic channel. Therefore, it is likely the water or PBS causing the cavity length to increase. An observation was made in which “veins” developed in the SU-8/UV-glue that forms the microfluidic channel. This indicates the fluid once diffused into the SU8/UV-glue and then eventually dried up. When fluid enters the channel, the veins disappear,

indicating the fluid is back in the veins. Figure 5.4 presents images of this phenomenon. There are two different documented cases in which the veins disappear quickly and very slowly.

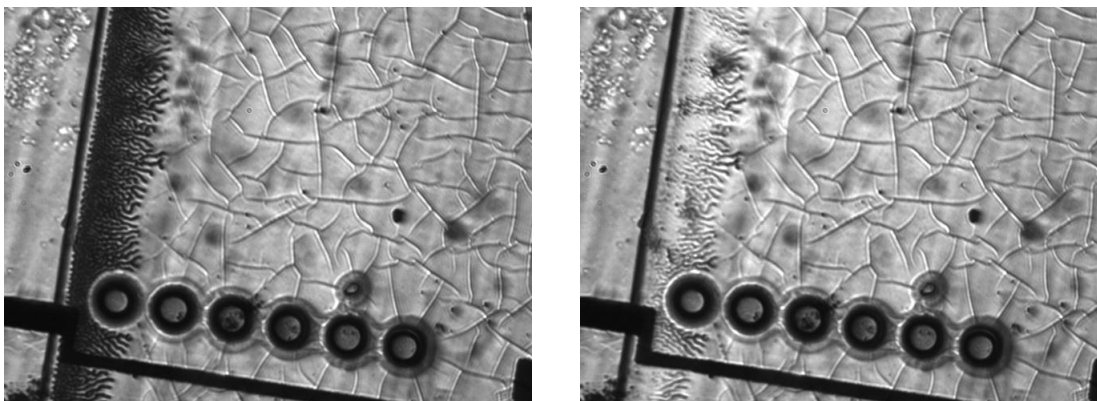


Figure 5.4 Chip 30-Sep-2011 where (a) fluid has just entered the microfluidic channel at 0 min, and (b) 3 hrs later.

Two hypotheses are proposed to explain why the cavity lengths are increasing in the air holes. The first is the fluid is entering into the air holes and creating a longer optical path length, which becomes interpreted as a larger cavity length since the refractive index is presumed to only be air. However, imaging at IR and blue wavelengths indicate that “veins” do not go near the air holes, making this hypothesis unlikely. These imaging results are presented in Fig. 5.5. Furthermore, this hypothesis is doubtful because the dynamic behavior seems to saturate, which is not expected for water filling the air holes. The second hypothesis is the fluid could be causing the SU-8 or UV-glue to swell. A literature search provides that polymers can swell when exposed to aqueous solutions, especially when SU-8 is exposed to water. One of the authors [1] presents a similar dynamic response with SU-8. Table 5.1 summarizes the literature search.

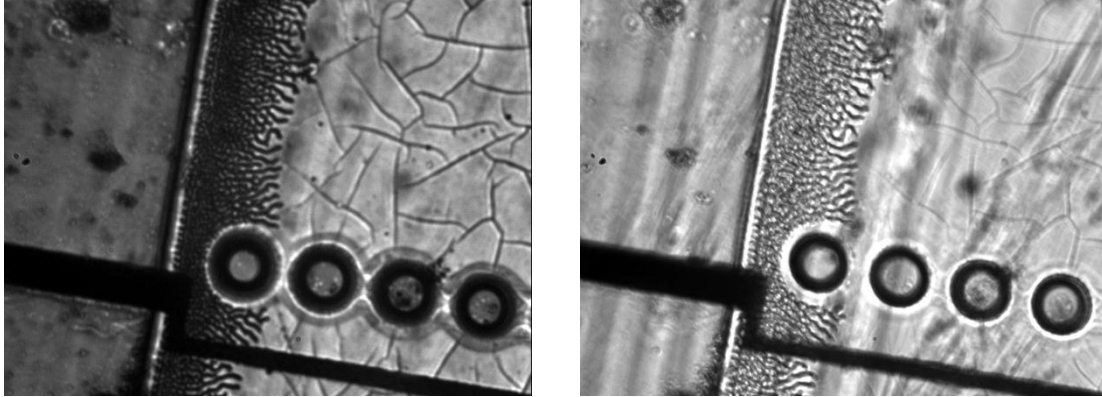


Figure 5.5 Imaging veins with (a) IR LED and (b) blue LED.

Table 5.1 Summary of literature search on polymer swelling.

First author, year	Polymer	Solvent	Swelling detection mechanism
Hill, 2007 [1]	SU-8	Water	Cavity length change of Fabry Perot pressure sensor
Wouters, 2010 [2]	SU-8	Water, IPA, PGMEA	Imaging a stress indicator structure
Liquin, 2010 [3]	SU-8	Electroforming solution	Dimension measurements of SU-8 moulds
Liu, 2010 [4]	SU-8	Water	Laser reflected off micro-cantilever and position measured with photodetector
Gervinskas, 2011 [5]	PMMA	Water, ethanol, methanol	Wavelength shift of Fabry Perot cavity

An explanation is given in the literature to why SU-8 swells when exposed to water and its fabrication dependence [2]. In summary, SU-8 is a poro-elastic solid that contains a polymer network. When there is residual solvent in the SU-8, which occurs from less soft baking exposure, there is more polymerization or cross-linking. It is known that polymers with a higher degree of cross-linking are more sensitive to swelling caused by water. This is due to the presence of more hydroxyl groups in the polymer matrix, which create strong hydrogen bonds with the water molecules. Furthermore, the occurrence of cracking and delamination is related to

polymer cross-linking. If there is more cross-linking, then the SU-8 is stronger and fewer cracks are formed. Cracks are indeed observed back in Fig. 5.4. Thus, this particular chip has less cross-linking and the SU-8 does not swell as much as it potentially could.

## **5.2 RI measurements with isothermal apparatus**

### **5.2.1 Isothermal apparatus details**

As described in Chapter 4, the temperature of the isothermal apparatus is controlled on the circulating water bath. The temperature is increased using the heating element on the water bath, and is decreased by adding cups of cold water to the water bath reservoir. The temperature changes by about 1°C per minute in both directions. Even though the water bath has its own thermometer, the temperature was determined and adjusted to the values on the thermometers inserted into the water box. There are three thermometers in the water box and the standard deviation between them is  $\leq 0.3^\circ\text{C}$ . At low temperatures, the water bath and the inserted thermometers were within a degree of each other. At higher temperatures, the water bath often needed to be a few degrees higher to reach the desired temperature on the inserted thermometers. This makes some sense as heat could be lost between the water bath and the water box.

A temperature pattern is chosen in the following order: 30°C, 50°C, 40°C, 70°C, and 60°C. This order was chosen to avoid any possible systematic effects on the results. Furthermore, 30°C was selected as the first value because it is more time-consuming to reduce the temperature on the water bath to values close to room temperature ( $\sim 22^\circ\text{C}$ ). This temperature was also chosen as the lowest value because it is tricky to maintain an exact temperature close to room temperature. To save time, all spatial points are measured at one temperature before changing the temperature.

The time needed to measure all spatial points at one temperature is about 45min to one hour. One contribution to this number is that it takes about 1-2 minutes to measure the spectrum at one point. The integration time of the spectrometer is set at 10 seconds to improve the signal-to-noise ratio, and then three or more spectrum updates are allowed before saving the spectrum. Since there are 15 points measured in these experiments (12 air holes and 3 points in the channel), it takes up to 30 minutes to measure all the spatial points. In hindsight, it would have been better to measure only the total of six needed air holes to help avoid the relatively slow polymer swelling dynamic. Additional contributions to the 45min to one hour value are the time it takes to change the temperature, and sometimes the need to power cycle the water bath. The power cycling is necessary to remove bubbles that get caught underneath the optical chip, and is also needed when the water bath suddenly shuts off.

### **5.2.2 Chip 28-Jun-2011**

In this section, selected results for Chip 28-Jun-2011 is presented for both PBS and water in the microfluidic channel. Figure 5.6(a) is the measured cavity length in the air holes, as well as a 2<sup>nd</sup> order polynomial fit. Figure 5.6(b) is the refractive index of PBS versus wavelength at three discrete points in the microfluidic channel. As seen in this figure, the refractive indices at the different points are very close to each other, which is the expected result since there should not be a spatial dependence of refractive index. Figures 5.7 (a) and (b) are the equivalent results for water.

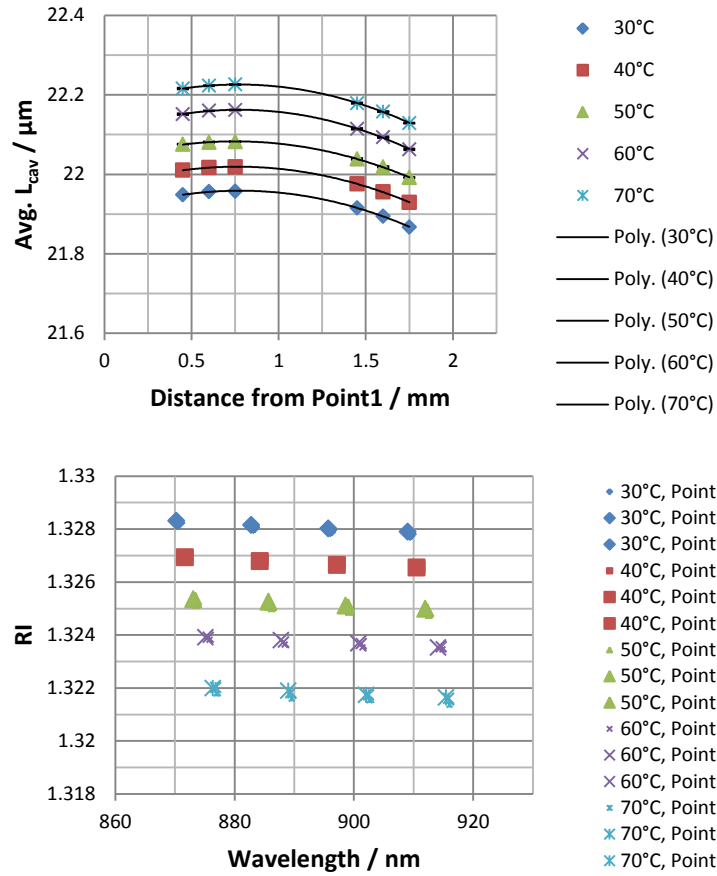


Figure 5.6 Chip 28-Jun-2011, PBS (a) cavity length interpolation and (b) refractive indices.

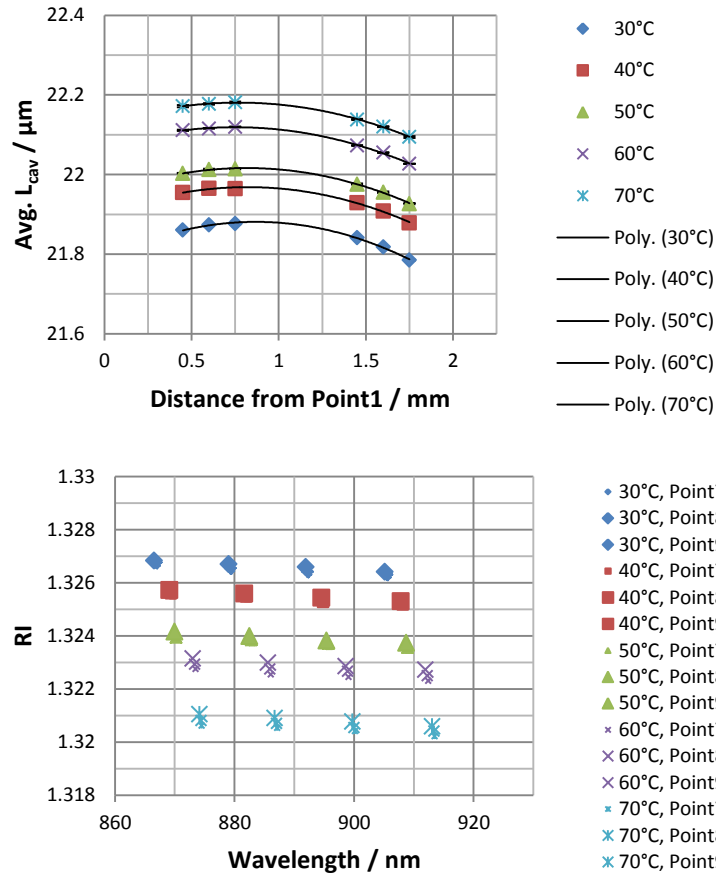


Figure 5.7 Chip 28-Jun-2011, DI water (a) cavity length interpolation and (b) refractive indices.

### 5.2.3 Chip 20-Aug-2011

In this section, selected results for Chip 20-Aug-2011 is presented for both water and PBS in the microfluidic channel. Figure 5.8(a) is the measured cavity length in the air holes, as well as a 2<sup>nd</sup> order polynomial fit. Figure 5.8(b) is the refractive index of water versus wavelength at three discrete points in the microfluidic channel. As seen in this figure the refractive indices at the different points are not very close to each other. This is likely due to the fact that the cavity length interpolation is steeper compared to Chip 28-Jun-2011, such that the refractive index is more sensitive to knowing the exact location of the spatial point.

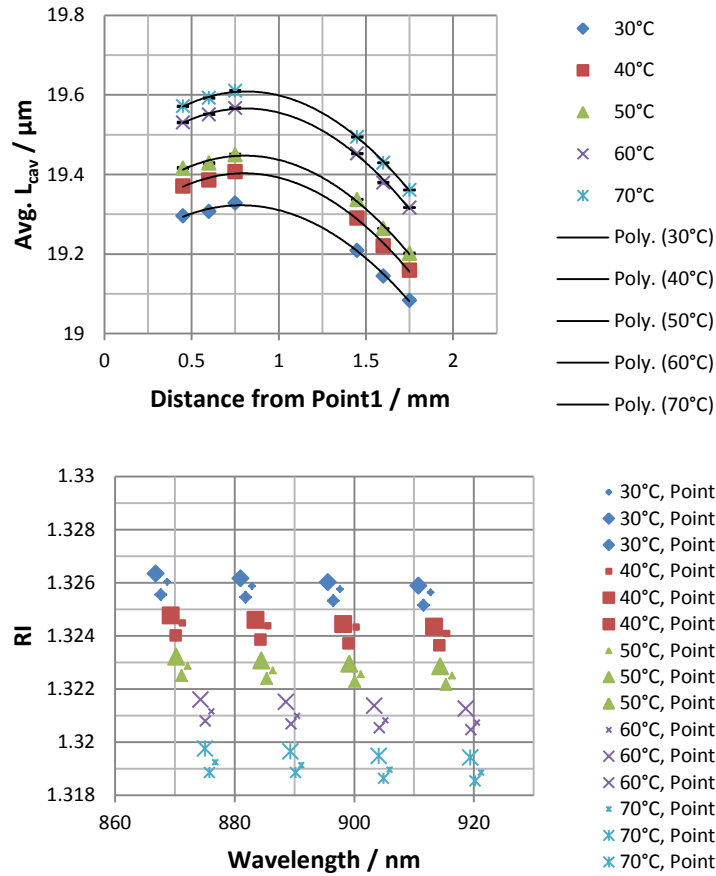


Figure 5.8 Chip 20-Aug-2011, DI water (a) cavity length interpolation and (b) refractive indices.

Figures 5.9 (a) and (b) are the equivalent results for PBS. As seen in Fig. 5.9(b), the refractive indices at the different points are not very close to each other. This is again likely due to the fact that the cavity length interpolation is steeper such that the refractive index is more sensitive to knowing the exact location of the spatial point. In all the experiments, there is about  $50\mu\text{m}$  of uncertainty where the spatial point is located. Future improvements could be made in which a scale bar is deposited with the electrodes to help improve the known location of the spatial point. However, the minimum resolution of the current photolithography mask for the gold electrodes is about  $20\mu\text{m}$ , and has the tendency to “bleed” to a bigger feature size.

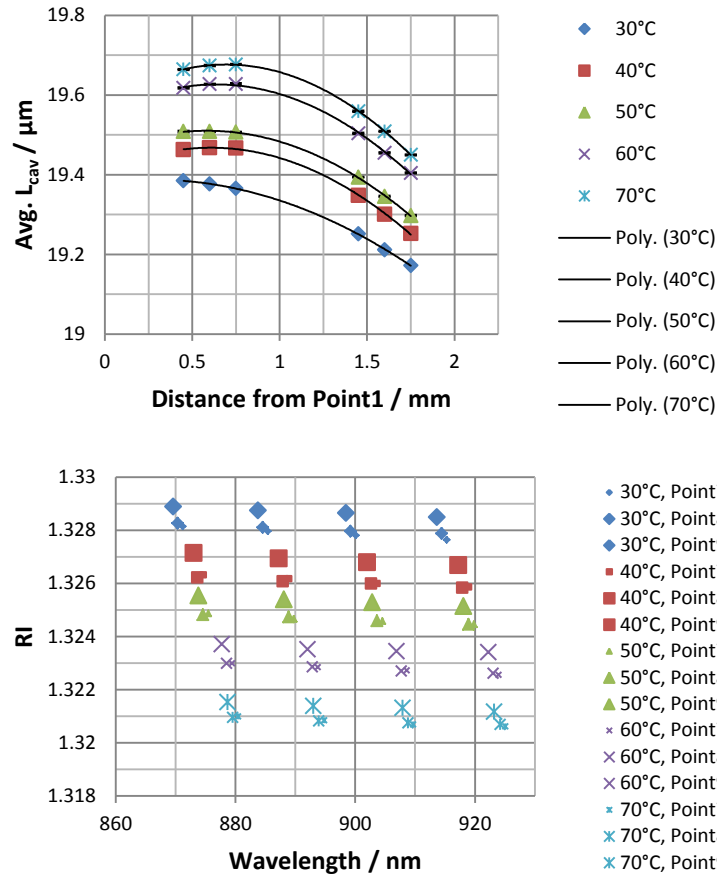


Figure 5.9 Chip 20-Aug-2011, PBS (a) cavity length interpolation and (b) refractive indices.

#### 5.2.4 H<sub>2</sub>O vs. NIST, PBS vs. H<sub>2</sub>O, and PBS average

The accuracy of the results can be established by comparing to the known  $n(T,\lambda)$  relationship for water. As presented in Chapter 2, a paper by Harvey *et al.* [6] presents a formula where refractive index is a function of wavelength, temperature, and density. The authors of this paper have affiliations to the National Institute of Standards and Technology, so their formula is often referred to as the NIST equation in this work. Figure 5.10 compares NIST to Chip 28-Jun-2011, and Fig. 5.11 compares NIST with Chip 20-Aug-2011. The average of the three different points in the microfluidic channel are calculated and plotted, where the error bars are the standard deviation. As expected, there are larger standard deviation bars for Chip 20-Aug-2011.

The data is fairly close to what is predicted by the NIST formula. Furthermore, one should note the uncertainty of the NIST formula is  $1 \times 10^{-3}$  for the wavelength range between 0.7 and 1.1  $\mu\text{m}$ .

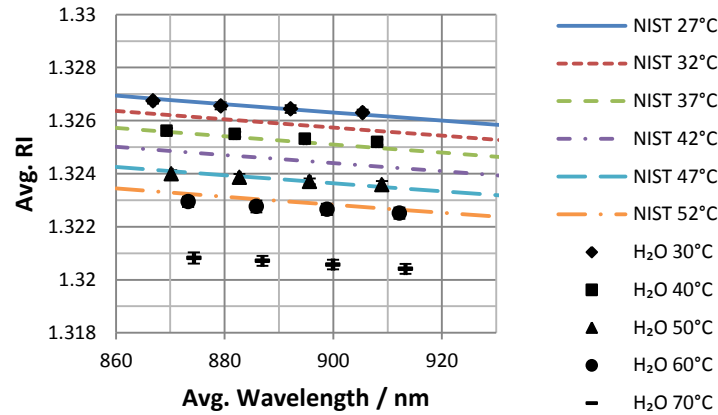


Figure 5.10 Chip 28-Jun-2011, H<sub>2</sub>O vs. NIST

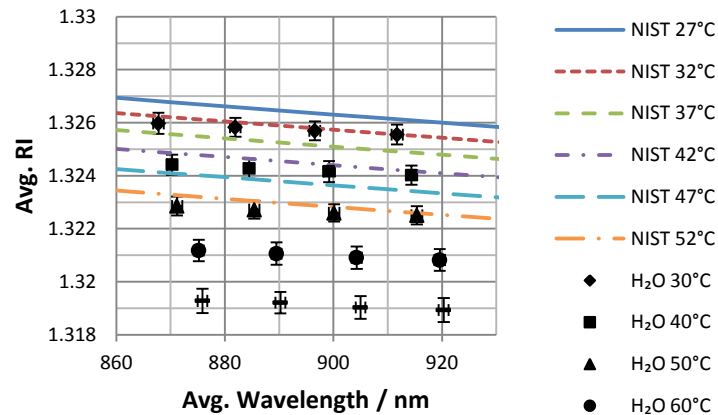


Figure 5.11 Chip 20-Aug-2011, DI water vs. NIST.

The accuracy of the water data when compared to NIST creates confidence in the PBS data. The PBS data is compared with the water data in Fig. 5.12. For viewing simplicity, the refractive index is averaged across the four wavelengths, which itself is the average across the different channel positions. Thus, Fig. 5.12 represents  $n(T, \lambda = \lambda_{\text{avg}})$ , and error bars are not included because of the mixed units. Looking back at Fig. 5.10 shows the refractive indices are higher than expected, such that the water data is likely high in Fig. 5.12 (a). Figure 5.11 shows

the refractive indices are lower than expected, such that the water data is likely low in Fig. 5.12

(b). PBS remains fairly consistent between the two different chips.

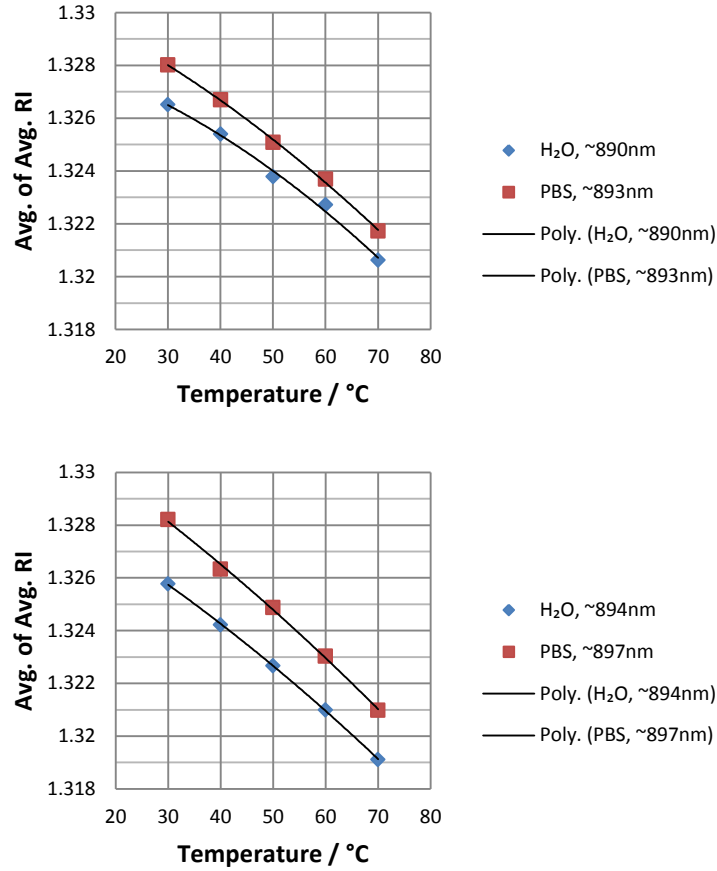


Figure 5.12 (a) Chip 28-Jun-2011 and (b) Chip 20-Aug-2011. Error bars are not included because of the mixed units of averaging spatial points and then averaging resonant wavelengths.

The consistency of  $n(T, \lambda)$  for PBS between the two chips is seen in Fig. 5.13. In addition, the average is taken between the two chips. This results in an average (between chips) of an average (across wavelengths) of an average (between spatial points). The 2<sup>nd</sup> order polynomial that fits the PBS Avg. data is given by:

$$n_{PBS}(T) = -6.4065 \times 10^{-7} T^2 - 1.0275 \times 10^{-4} T + 1.3317 \quad (5.1)$$

where  $T$  is in °C. More data should be collected to obtain more reliable coefficients.

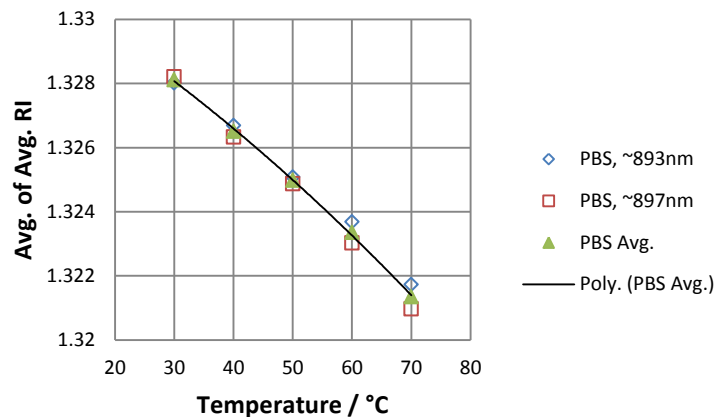


Figure 5.13 Refractive index of PBS for both chips, and the average between them.

### 5.2.5 Problem with data processing algorithm

There is a documented instance in which the sequential modes that minimize the standard deviation do not result in the expected refractive index. This documented case is for Chip 28-Jun-2011, with PBS, at 30°C, for Point7. The modes that minimize the standard deviation are 68, 67, 66, and 65, which provide a standard deviation of  $1.9890 \times 10^{-4}$ . The modes that do not minimize the standard deviation but result in the expected refractive index are 67, 66, 65, and 64, returning a standard deviation of  $2.0150 \times 10^{-4}$ . There is likely some noise in obtaining the resonant wavelengths that is causing the problem.

To get around this problem, a “majority” process can be added to the algorithm. The other two points in the microfluidic channel have modes that do result in the expected refractive index. Therefore, Point7 should also have the same mode sequence. This idea was implemented earlier with the data. Another way to get around the problem is by selecting an expected  $\pm 1\%$  window for the refractive indices. It turns out that by changing the modes, the refractive index will change by the percent change of the modes, or in this case  $(68-67)/67 = 1.5\%$ . By

implementing both the “majority” and  $\pm 1\%$  window methods, the data processing algorithm is more robust.

### 5.2.6 Justification of linear RI approximation

In Chapter 4, it was discussed that the refractive index of the cavity became a third order polynomial. This results in three different roots, or solutions for  $n_{FP}$ . A linear approximation was made to avoid calculating the three different roots. It is a good idea to check if the linear assumption is statistically close to the third order polynomial near the root. Figure 5.14 presents the third-order polynomial and the linear approximation, where the roots occur at  $y=0$ . This figure uses actual data from Chip 28-Jun-2011 with  $H_2O$ ,  $m=66$ , and  $\lambda_m=879nm$ . The linear approximation does indeed match the third order polynomial near one of the roots. The other roots are not physically possible.

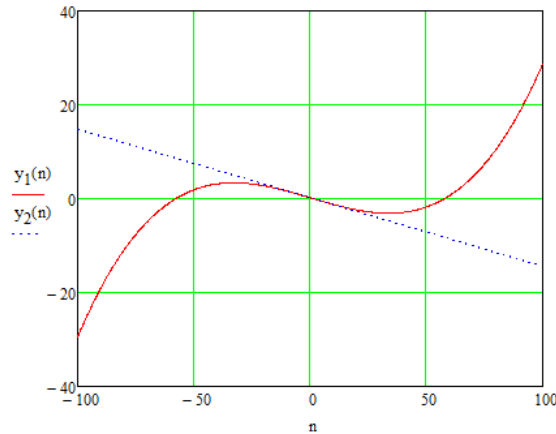


Figure 5.14 Chip 28-Jun-2011, roots for third order polynomial and linear approximation.

## 5.3 RI measurements with joule heating

Joule heating is possible with a high electrical conductivity solution, such as PBS. The refractive index of PBS was previously measured with the isothermal apparatus. Consequently,  $n(T, \lambda)$  is known for PBS, and the data is presented in Fig. 5.6(b), Fig. 5.9(b), and Fig. 5.13. By measuring a refractive index for a given resonant wavelength, the temperature can be

extrapolated. This is one of the original goals of the project to help understand the temperature rises that our biological cells are exposed to.

### 5.3.1 Chip 05-Apr-2011

In this section, results for Chip 05-Apr-2011 is presented at room temperature with joule heating. This experiment was actually done before any of the isothermal apparatus experiments, and was one of the inspirations to build an isothermal apparatus. Figure 5.15 is an image of the electrode structure and the air holes. The distances between the spatial points are determined with lines drawn on top of the image. The air hole on the left side of the microfluidic channel did not end up being used because it became filled with PBS. An example of a spectra spot resulting from the back-reflection is seen in Fig. 5.16. Each spatial point is measured with the electrodes off, turned on for 2 minutes, and then turned off for two minutes. This is repeated for each point. The resonant wavelengths nearly returned to the original position after the four minutes, as seen in both Fig. 5.17(a) and (b).

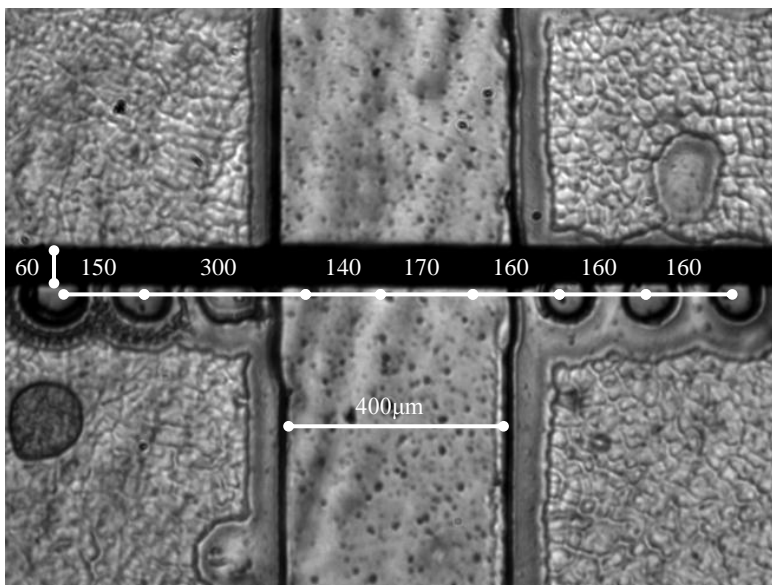


Figure 5.15. Microscope image of the microfluidic channel and distance between points.

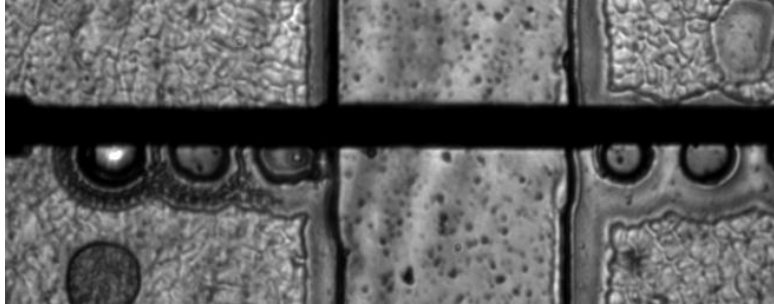


Figure 5.16. Microscope image and a spectra spot seen from back-reflection in one of the air-holes. The spectra spot is in Point1.

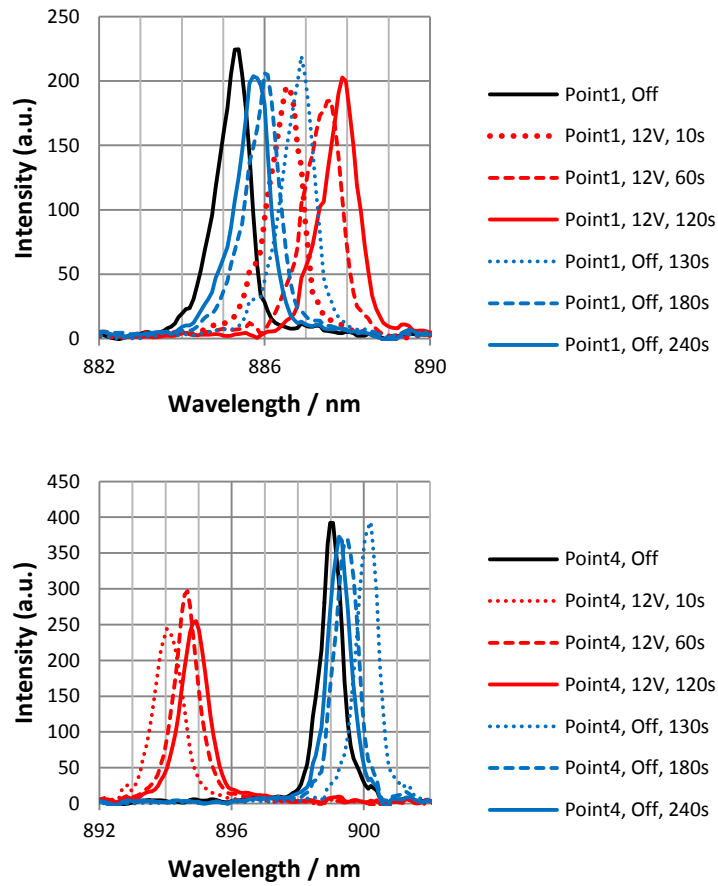


Figure 5.17 Resonant wavelengths with a temporal response. Electrodes are energized for 2min then off for 2min. (a) Point1 is the far left air hole and (b) Point4 is in the center of the microfluidic channel.

Figure 5.18 is the measured cavity length in the air holes as well as a 2<sup>nd</sup> order polynomial fit. It is observed the cavity length does not increase as much as the chips using the isothermal apparatus. Figure 5.19 is the refractive index of PBS at three discrete points in the microfluidic channel. From this figure, it is noticed that the refractive index distribution is fairly uniform when the electrodes are not energized. Furthermore, the refractive index at this “off” temperature is  $n=1.328$ , which corresponds to a temperature of 30°C when compared with Fig. 5.13. This is a little warmer than the expected room temperature. A lateral refractive index distribution is observed when the electrodes are energized. The refractive index at the center of the channel is 1.318, which results in a temperature greater than 70°C when compared with Fig. 5.13.

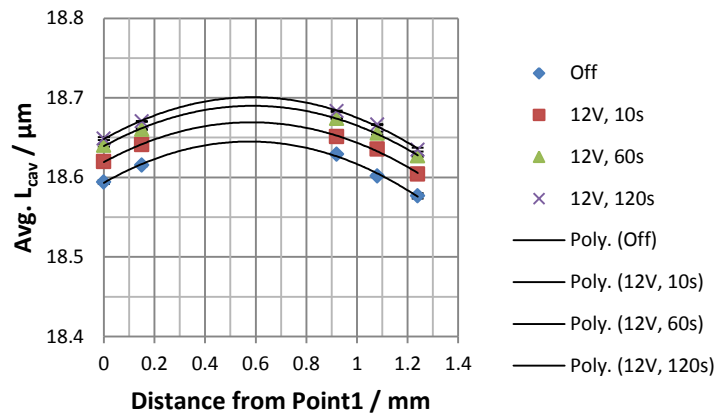


Figure 5.18 Chip 05-Apr-2011, PBS cavity length interpolation

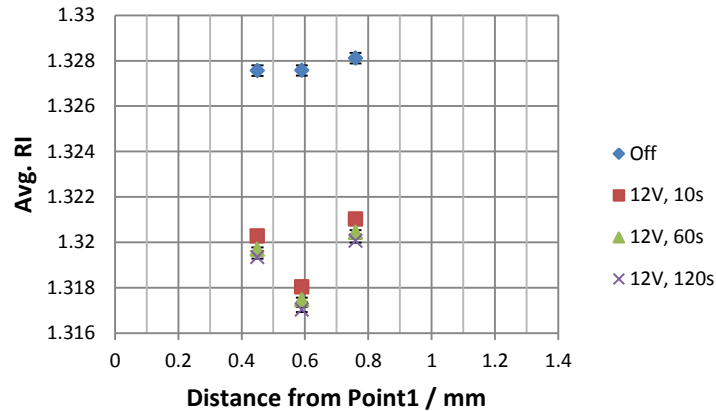


Figure 5.19. Chip 05-Apr-2011, refractive indices for different spatial positions in the microfluidic channel. The electrodes are energized for 2 minutes.

### 5.3.2 Experimental and simulated refractive index distributions

Experimental and simulated refractive index distributions can be compared to help validate each other. As performed Chapter 3, the refractive index distribution is obtained with a joule heating simulation and the resulting temperature distribution is converted to refractive index. The simulation attempted to match the experimental parameters, including:

- Three temperature dependent parameters as discussed in Chapter 3, where  $\sigma_0=1.25$  S/m
- Electrode width of  $60\mu\text{m}$  as determined from Fig. 5.15
- Channel height of  $18.6\mu\text{m}$  as roughly taken from Fig. 5.18
- An applied voltage of  $3.5V_{\text{rms}}$ , as approximately measured by the oscilloscope with 12V programmed on the function generator. This voltage easily varied by  $\pm 1V_{\text{rms}}$  when the leads from the coaxial cable were moved around.

The resulting temperature distribution in the x-y plane (looking down on the electrodes similar to microscope image) is presented in Fig. 5.20, where  $z=0\mu\text{m}$ .

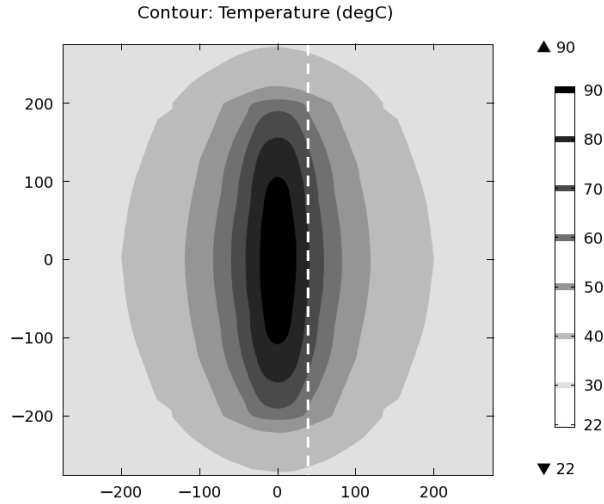


Figure 5.20 Temperature distribution in the x-y plane, at  $z=0\mu\text{m}$ . The dashed line is at  $x=40\mu\text{m}$ , which is the distance where spectra was taken.

The particular distribution of interest is a 1-D cut that is about where the spatial points are located. The x-coordinate is chosen to be at the distance where the spectra data was taken. Since the electrodes are  $30\mu\text{m}$  from the center, and the spectra spot of  $\sim 21\mu\text{m}$  is next to the electrode, a distance of  $x=40\mu\text{m}$  is selected. The z-coordinate is chosen to represent the average refractive index in the direction of the optical path, as first discussed in Chapter 3. This coordinate is determined to be at  $z=5\mu\text{m}$ . Using Eq. 5.1, the temperature profile is converted to be a refractive index profile and is seen in Fig. 5.21. A problem is seen that the COMSOL simulation is shifted above the data. However, the “off” data is pretty warm at  $30^\circ\text{C}$ . If the “off” data is shifted up by  $10^\circ\text{C}$  ( $=0.0016\text{RIU}$ ), and the rest of the data follows, then the COMSOL simulation and the data are in reasonable agreement. This problem of low refractive index values is due to a larger interpolated cavity length.

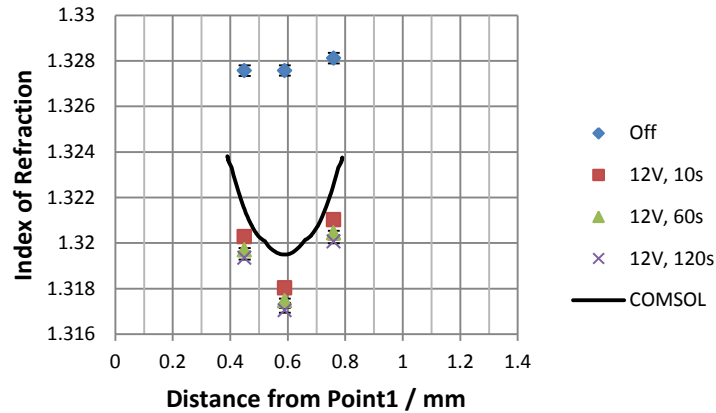


Figure 5.21. Chip 05-Apr-2011, refractive indices for different spatial positions in the microfluidic channel and COMSOL simulation.

### 5.3.3 Implication of experimental and simulated results

The reasonable agreement between experimental and simulation results present an interesting implication. If all of the experimental parameters are well-known, then only a 3D COMSOL joule heating simulation is needed to provide the experimental:

- (1) Temperature distribution
- (2) Refractive index distribution for a known  $n(T, \lambda)$  relation. The  $n(T, \lambda)$  relation could be obtained by the isothermal apparatus or a laboratory refractometer.

The COMSOL simulation should be contrasted with analytical solutions of temperature rises caused by DEP electrodes in a microfluidic channel [7, 8, 9]. None of the analytic equations have considered the entire combination of electrode geometry, spatial dependence, and all temperature dependent parameters. Truthfully, an analytic solution is difficult to obtain with all of the temperature dependent parameters. A 3D simulation will provide the most accurate possible solution, as it also includes heat transfer in all directions. However, the applied

experimental voltage is sensitive to losses at the given 50MHz. The experimental distribution is an exact response to the voltage losses, whereas the simulation is only a guess. A future improvement is to measure the voltage closest to the chip during the experiment.

## 5.4 GRIN lens imaging

A consequence of the temperature distribution from joule heating is a refractive index distribution. This results in either a positive or negative gradient index lens, which becomes more obvious in an optical cavity. Images are seen in Fig. 5.22 and 5.23. In Fig. 5.22(b), channel darkening is seen on the outside of the circle electrodes. This is due to a relatively low refractive index underneath the electrodes and a relatively high refractive index away from the electrodes. Light will bend towards higher refractive index, which is away from the electrodes. This causes cavity instability as mentioned in Chapter 3. A bright spot is seen within the circle electrodes. This is due to the same effect, as light will bend towards the higher refractive index in the center of the circle electrodes.

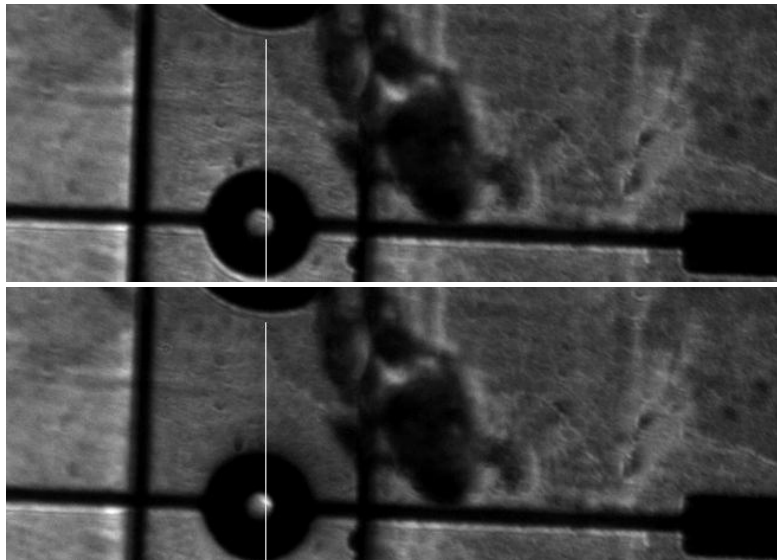


Figure 5.22. (a) Electrodes off and (b) electrodes energized, revealing darkening on the outside of the circle electrodes and a bright spot in the center of the electrodes. The white line going partially through each image is where pixel intensity data is taken.

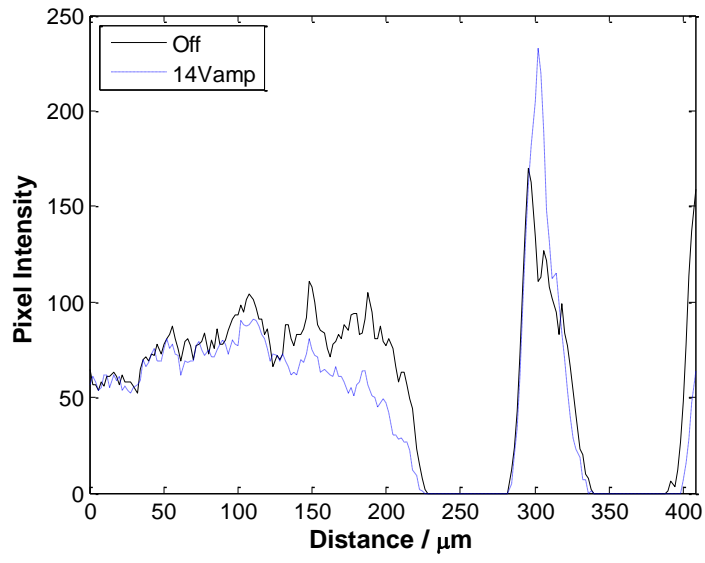


Figure 5.23. Pixel intensity from Fig. 5.22.

## References

- [1] G. C. Hill, R. Melamud, F. E. Declercq, A. A. Davenport, I. H. Chan, P. G. Hartwell, and B. L. Pruitt, "SU-8 MEMS Fabry-Perot pressure sensor," *Sensors and Actuators A*, vol. 138, no. 1, pp. 52-62, 2007.
- [2] K. Wouters and R. Puers, "Diffusing and swelling in SU-8: insight in material properties and processing," *J. Micromech. Microeng.*, vol. 20, 2010.
- [3] D. Liqun, Z. Benzhuang, and L. Yaping, "Reducing SU-8 hygroscopic swelling by ultrasonic treatment," *Nano-Micro Letters*, vol. 2, no. 3, pp. 197-203, 2010.
- [4] C. Liu, Y. Liu, M. Sokuler, D. Fell, S. Keller, A. Boisen, H. Butt, G. K. Auernhammer, and E. Bonaccorso, "Diffusion of water into SU-8 microcantilevers," *Physical Chemistry Chemical Physics*, vol. 12, pp. 10577-10583, 2010.
- [5] G. Gervinskas, D. Day, and S. Juodkazis, "High-precision interferometric monitoring of polymer swelling using a simple optofluidic sensor," *Sensors and Actuators B*, vol. 159, no. 1, pp. 39-43, 2011.
- [6] A. H. Harvey, J. S. Gallagher, and J. M. H. Levelt Sengers, "Revised formulation for the refractive index of water and steam as a function of wavelength, temperature and density," *J. Phys. Chem. Ref. Data*, vol. 27, no. 4, pp. 761-774, 1998.
- [7] A. Ramos, H. Morgan, N. G. Green, and A. Castellanos, "Ac electrokinetics: a review of forces in microelectrode structures," *J. Phys. D: Appl. Phys.* vol. 31, no. 18, pp. 2338-2353, 1998.
- [8] U. Seger-Sauli, M. Panayiotou, S. Schnydrig, M. Jordan, and P. Renaud, "Temperature measurements in microfluidic systems: heat dissipation of negative dielectrophoresis barriers," *Electrophoresis*, vol. 26, no. 11, pp. 2239-2246, 2005.

[9] M. S. Jaeger, T. Mueller, and T. Schnelle, “Thermometry in dielectrophoresis chips for contact-free cell handling,” *J. Phys. D: Appl. Phys.*, vol. 40, no. 1, pp. 95-105, 2007.

## **Chapter 6: Conclusions and future work**

In conclusion, this thesis demonstrates a microfluidic refractometer with spatial, temperature, and wavelength dependence. The method only provides lateral resolution since the refractive index distribution is optically averaged in the longitudinal direction. In our case, the longitudinal dimension is much smaller than the lateral dimensions in microfluidic channels. A refractive index measurement will indicate the temperature of the solution if the  $n(T, \lambda)$  relationship is known. To obtain this relationship for phosphate buffered saline solution, an isothermal apparatus was built with controllable temperature. Earlier parts of the work were presented at an SPIE conference [1].

Computer simulations were also performed to compliment experimental work. Electrostatic and joule heating simulations were solved with COMSOL Multiphysics (version 4.1). Electrostatic simulations in 2D resulted in electric field lines, magnitude distribution, as well as the  $\text{grad}(|E\text{-field}|^2)$ . Joule heating simulations were run to provide a temperature distribution, and accuracy was improved by including temperature dependent parameters. These simulations needed to be in three dimensions so heat transfer could be considered in all spatial directions. The temperature distribution was also converted to a refractive index distribution. Optical simulations were performed with TFCalc to find the reflection and phase spectra of different dielectric mirrors. Furthermore, optical cavities were made with the different dielectric mirrors and effects of light penetration into the mirrors could be observed in the transmission spectra. This helped to verify the round-trip phase equation used in experimental work.

### **6.1 Contributions and practical considerations of the thesis**

In this section, contributions of the thesis as well as practical considerations will be listed. The list method is chosen because it is more concise for the many different unrelated subjects.

One area of interest is refractive index measurements, with either the isothermal apparatus or joule heating as the temperature source. The other area of interest is gradient index (GRIN) lenses.

### **6.1.1 RI measurements**

Contributions:

- A novel data processing algorithm was demonstrated that includes mirror penetration depth and a statistical choice of mode numbers.
- A novel technique was implemented with near-by air holes to calibrate out mechanical changes. Air holes are advantageous because they have negligible dispersion. Mechanical changes are inevitable for temperature dependence due to thermal expansion. Furthermore, a mechanical change due to polymer swelling was observed.
- Data were presented for  $n(T,\lambda)$  of phosphate buffered saline at our LED wavelength range (860nm – 940nm), which is useful because not much data is published yet for PBS at that range. Data for PBS is particularly helpful because it is commonly used in biological research, and the wavelength range is of interest because it is within the optical window of biological tissue.
- With an  $n(T,\lambda)$  relationship, temperature can be obtained from refractive index and vice-versa. The experiments measure refractive index, while joule heating simulations provide temperature.
- Spectra were measured with a lateral spatial resolution of about  $21\mu\text{m}$ , which is useful for non-uniform temperature/RI distributions caused by DEP electrodes.
- The method might have next best spatial resolution behind Rhodamine B. Rhodamine B can be toxic to biological cells and is used exclusively to measure temperature. However,

a refractive index cannot easily be converted from this temperature, as it will be the refractive index of the medium + Rhodamine B.

Practical considerations:

- Need to know precise dielectric mirror parameters for penetration into the mirrors.
- Should calibrate parabolic fit with air-filled channel (inconsistent data so far).
- Need to know precise spatial location of spectra spot. Otherwise, parabolic fit will over- or under- estimate the cavity length. This becomes more crucial with a steeper parabola.
- SU-8 expands with temperature over a ~2min time. This is a minor disadvantage using the isothermal apparatus because of slow temperature rises and the 5min wait before first measurement. This is a disadvantage in the joule heating case because spectra will need to be taken in one air hole at a time to measure ~2min of dynamic changes. By the time all points are measured (2min on, 2min off  $\times$  8 points = 32min); SU-8 swelling may have a significant impact.
- SU-8 swells with water over a >20min time and is dependent on baking time/intensity.
- Rhodamine B has a spatial resolution up to the diffraction limit. After the temperature distribution is understood, one can remove Rhodamine B from channel and then add biological cells.
- DEP is not likely practical for high-throughput cell analysis systems.

### 6.1.2 Gradient index lenses

Contributions:

- To the best of the author's knowledge, this work was the first to suggest that channel darkening was caused by a negative gradient index lens effect. A GRIN lens effect is likely enhanced by the fact it is within an optical cavity.
- The GRIN lenses have controllable focal length with voltage or inner radius of circle electrodes.
- Intensity images were provided that demonstrate both positive and negative GRIN lenses.
- The work provided focal lengths and stability in an optical cavity for positive and negative gradient index lenses. However, focal lengths and stability were only for the parabolic part of the refractive index distribution, as that is the distribution with well-established optical theory.
- A joule heating simulation was used to obtain refractive profile and calculate focal length.

Practical considerations:

- Even though temperature was converted to refractive index using  $n(T,\lambda)$  literature data for water, it can be assumed the RI \*gradient\* is similar between water and PBS.
- Difficult to experimentally measure focal length without noticeable transverse modes. This might be due to long focal length (~10mm) predicted by simulations. Could measure lateral refractive index distribution with 21 $\mu$ m resolution for quantification purposes instead. In this case, air holes will be needed.

## 6.2 Future work

As mentioned in Chapter 5, a problem was noticed that a sequence of modes which minimized the standard deviation did not result in the expected refractive index. The data processing algorithm can be improved by implementing both the “majority” and  $\pm 1\%$  window methods. In addition, it would help if a Matlab script was written, with only the need to input spectrum files. This would save a lot of manual data processing in Microsoft Excel. Another point of improvement would be depositing a ruler or scale in the microfluidic channel. This allows the spatial points to be known more accurately and reduces error for steeper cavity length interpolations. In addition, more data should be taken to give better statistical confidence in the method.

A final possibility is to use the method at different wavelengths with different high-powered LEDs. This requires designing other dielectric mirrors with a bandwidth that matches the LED and obtaining a spectrometer with an appropriate wavelength range. A concern with lower wavelengths is the steepness of the  $n(\lambda)$  curve of water (Appendix F). The data processing algorithm might need to be modified, such that the modes of interest do not minimize the standard deviation. An additional concern at lower wavelengths is the quickly changing refractive index with wavelength of the dielectric mirrors. The dispersion of the mirrors was not considered in this work because of the relatively flat  $dn/d\lambda$  in the near infrared wavelengths (Appendix F). Consequently, the method is easier to implement at other infrared wavelengths.

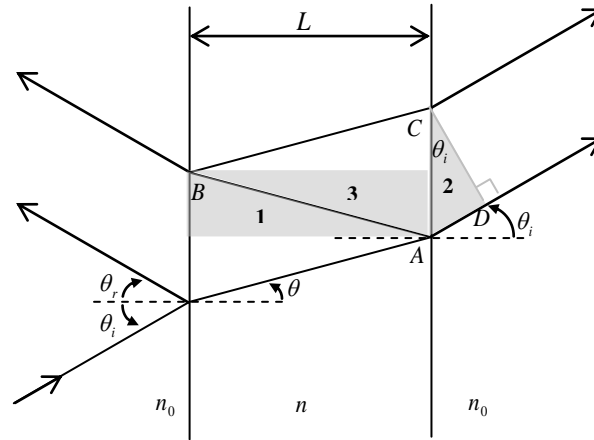
## References

- [1] J. Kindt, M. Naqbi, T. Kiljan, W. Fuller, W. Wang, D. W. Kisker and K. L. Lear, “Automated optical cell detection, sorting, and temperature measurements,” Proc. SPIE 7902, 790222 (2011).

## Appendix A: Derivations

### A.1 Fabry-Pérot transmission

The transmission spectrum is found starting with the path difference between two successive rays:



$$\Delta = n(\overline{AB} + \overline{BC}) - n_0 \overline{AD}$$

Using triangle 1:

$$\cos \theta = \frac{L}{\overline{AB}} \Rightarrow \overline{AB} = \frac{L}{\cos \theta} = \overline{BC}$$

Using triangle 2:

$$\sin \theta_i = \frac{\overline{AD}}{\overline{AC}} \Rightarrow \overline{AD} = \overline{AC} \sin \theta_i$$

Using triangle 3:

$$\sin \theta = \frac{1/2 \overline{AC}}{\overline{AB}} \Rightarrow \overline{AC} = 2 \overline{AB} \sin \theta = 2 \left( \frac{L}{\cos \theta} \right) \sin \theta$$

Going back to first Eq.

$$\Delta = n \left( \frac{L}{\cos \theta} + \frac{L}{\cos \theta} \right) - n_0 \overline{AC} \sin \theta_i$$

$$\Delta = 2n \left( \frac{L}{\cos \theta} \right) - n_0 \left[ 2 \left( \frac{L}{\cos \theta} \right) \sin \theta \right] \sin \theta_i$$

Using Snell's Law,  $n_0 \sin \theta_i = n \sin \theta$

$$\Delta = 2n \left( \frac{L}{\cos \theta} \right) - n_0 \left[ 2 \left( \frac{L}{\cos \theta} \right) \sin \theta \right] \left[ \frac{n}{n_0} \sin \theta \right]$$

$$\Delta = 2n \left( \frac{L}{\cos \theta} \right) - \left[ 2n \left( \frac{L}{\cos \theta} \right) \sin \theta \right] \sin \theta$$

$$\Delta = 2n \left( \frac{L}{\cos \theta} \right) [1 - \sin^2 \theta]$$

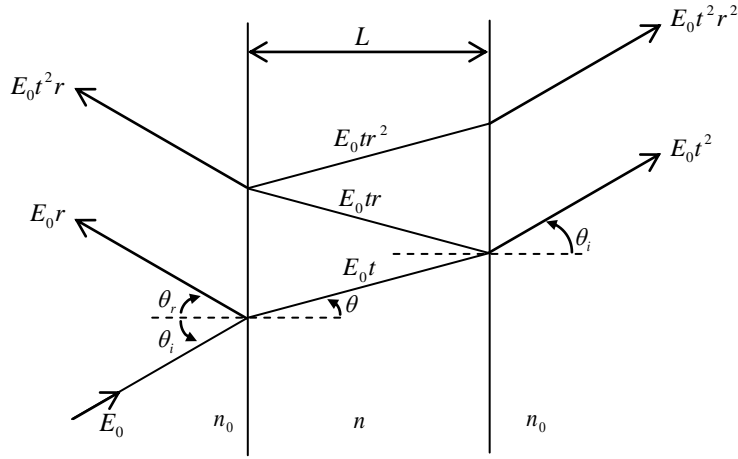
Using the trigonometric identity,  $\cos^2 \theta + \sin^2 \theta = 1$

$$\Delta = 2n \left( \frac{L}{\cos \theta} \right) [\cos^2 \theta] = 2nL \cos \theta$$

This path length leads to a phase shift of:

$$\delta = k\Delta = \frac{2\pi}{\lambda} \Delta = \frac{4\pi}{\lambda} nL \cos \theta$$

where  $k$  is the wave number, or propagation constant, and represents the change in phase per meter along the path travelled by the wave at any instant.



Taking the sum of all the transmitted amplitudes:

$$E_T = E_0 t^2 + E_0 t^2 r^2 e^{i\delta} + E_0 t^2 r^4 e^{i2\delta} + \dots$$

This is a geometric series with ratio  $r^2 e^{i\delta}$

$$E_T = E_0 t^2 \sum_{m=0}^{\infty} r^{2m} e^{im\delta} = \frac{E_0 t^2}{1 - r^2 e^{i\delta}}$$

The power of the transmittance and reflectance is given by:

$$R = |r|^2 = r r^*$$

$$T = |t|^2 = t t^*$$

in which the asterisk indicates the complex conjugate. Therefore,

$$E_T = \frac{E_0 T}{1 - R e^{i\delta}}$$

The intensity is given by:

$$I_T = |E_T|^2 = E_T E_T^* = I_0 \left( \frac{T}{1 - R e^{i\delta}} \right) \left( \frac{T}{1 - R e^{-i\delta}} \right)$$

$$\frac{I_T}{I_0} = \frac{T^2}{1 - R e^{i\delta} - R e^{-i\delta} + R^2 e^0} = \frac{T^2}{1 - R(e^{i\delta} + e^{-i\delta}) + R^2}$$

$$\frac{I_T}{I_0} = \frac{T^2}{1 - 2R \left( \frac{e^{i\delta} + e^{-i\delta}}{2} \right) + R^2} = \frac{T^2}{1 - 2R \cos \delta + R^2}$$

Using the identity:

$$\cos 2\theta = 1 - 2\sin^2 \theta$$

$$\cos \theta = 1 - 2\sin^2(\theta/2)$$

Therefore,

$$\frac{I_T}{I_0} = \frac{T^2}{1 - 2R(1 - 2\sin^2(\delta/2)) + R^2} = \frac{T^2}{1 - 2R + R^2 + 4R\sin^2(\delta/2)}$$

$$\frac{I_T}{I_0} = \frac{T^2}{(1-R)^2 + 4R\sin^2(\delta/2)} = \frac{T^2}{(1-R)^2 \left[ 1 + \frac{4R}{(1-R)^2} \sin^2(\delta/2) \right]}$$

Where the coefficient of finesse is defined as  $F = \frac{4R}{(1-R)^2}$ .

$$\frac{I_T}{I_0} = \frac{T^2}{(1-R)^2} \frac{1}{[1 + F \sin^2(\delta/2)]}$$

Where  $I_0 = |E_0|^2$  is the intensity of the incident light beam. In this work, the incident light beam was an LED with a spectral distribution that could be modeled as a Gaussian distribution.

If there is absorbance in the mirrors,  $T = 1 - R - A$

$$\frac{I_T}{I_0} = \left( \frac{1-R-A}{1-R} \right)^2 \frac{1}{[1 + F \sin^2(\delta/2)]}$$

$$\frac{I_T}{I_0} = \left( \frac{1-R}{1-R} - \frac{A}{1-R} \right)^2 \frac{1}{[1 + F \sin^2(\delta/2)]}$$

$$\frac{I_T}{I_0} = \left(1 - \frac{A}{1-R}\right)^2 \frac{1}{[1 + F \sin^2(\delta/2)]}$$

Assuming there is negligible absorbance in the mirrors,  $T = 1 - R$

$$\frac{I_T}{I_0} = \frac{1}{1 + F \sin^2(\delta/2)}$$

The transmission spectrum has a maximum value when  $\sin^2(\delta/2) = 0$ , or in other words when the argument is zero or multiples of  $\pi$ .

$$\delta/2 = \frac{2\pi}{\lambda_m} nL \cos \theta = m\pi$$

Where  $m$  is a longitudinal mode number and for  $\theta = 0$ :

$$\lambda_m = \frac{2nL}{m}$$

## A.2 Electrostatic equations

Electric field is defined as:

$$\mathbf{E} = -\nabla V$$

Gauss's Law:

$$\nabla \cdot \mathbf{D} = \rho$$

where the constitutive relation is given by:

$$\mathbf{D} = \varepsilon_0 \mathbf{E} + \mathbf{P}$$

where the polarization density is given by:

$$\mathbf{P} = \varepsilon_0 \chi_e \mathbf{E} = \varepsilon_0 (\varepsilon_r - 1) \mathbf{E} = \varepsilon_0 \varepsilon_r \mathbf{E} - \varepsilon_0 \mathbf{E}$$

Therefore, the electric displacement field is:

$$\mathbf{D} = \varepsilon_0 \mathbf{E} + (\varepsilon_0 \varepsilon_r \mathbf{E} - \varepsilon_0 \mathbf{E}) = \varepsilon_0 \varepsilon_r \mathbf{E}$$

$$\mathbf{D} = -\varepsilon_0 \varepsilon_r \nabla V$$

Therefore, Gauss's Law becomes:

$$-\nabla \cdot (\varepsilon_0 \varepsilon_r \nabla V) = \rho$$

Since electric permittivity is spatially independent, the following vector calculus identity can be used:

$$-\varepsilon_0 \varepsilon_r \nabla^2 V = \rho$$

In a space-charge region:

$$-\varepsilon_0 \varepsilon_r \nabla^2 V = 0$$

$$\nabla^2 V = 0$$

### A.3 Maxwell's equations to plane waves

Maxwell's Equations in regions with no charges ( $\rho = 0$ ) and no currents ( $\mathbf{J} = 0$ ):

$$\nabla \cdot \mathbf{E} = 0$$

$$\nabla \cdot \mathbf{B} = 0$$

$$\nabla \times \mathbf{E} = -\frac{\partial \mathbf{B}}{\partial t}$$

$$\nabla \times \mathbf{B} = \mu_0 \epsilon_0 \frac{\partial \mathbf{E}}{\partial t}$$

Taking the curl of Faraday's Law of Induction:

$$\nabla \times (\nabla \times \mathbf{E}) = \nabla \times \left( -\frac{\partial \mathbf{B}}{\partial t} \right) = -\frac{\partial}{\partial t} \nabla \times \mathbf{B}$$

Using Ampere's circuital law:

$$\nabla \times (\nabla \times \mathbf{E}) = -\frac{\partial}{\partial t} \left( \mu_0 \epsilon_0 \frac{\partial \mathbf{E}}{\partial t} \right) = -\mu_0 \epsilon_0 \frac{\partial^2 \mathbf{E}}{\partial t^2}$$

Using the vector identity:

$$\nabla \times (\nabla \times \mathbf{V}) = \nabla(\nabla \cdot \mathbf{V}) - \nabla^2 \mathbf{V}$$

$$\nabla(\nabla \cdot \mathbf{E}) - \nabla^2 \mathbf{E} = -\mu_0 \epsilon_0 \frac{\partial^2 \mathbf{E}}{\partial t^2}$$

Using Gauss's Law, the divergence of the electric field is zero:

$$-\nabla^2 \mathbf{E} = -\mu_0 \epsilon_0 \frac{\partial^2 \mathbf{E}}{\partial t^2}$$

$$\frac{\partial^2 \mathbf{E}}{\partial t^2} = \frac{1}{\mu_0 \epsilon_0} \nabla^2 \mathbf{E}$$

An analogous derivation can be done starting with Ampere's circuital law, resulting in the following:

$$\frac{\partial^2 \mathbf{B}}{\partial t^2} = \frac{1}{\mu_0 \epsilon_0} \nabla^2 \mathbf{B}$$

The above are both wave equations, which are in the general form of:

$$\frac{\partial^2 U}{\partial t^2} = v_p^2 \nabla^2 U$$

Where the speed of the wave is given by  $v_p$ . Therefore, the speed of the electromagnetic wave

is:

$$v_p = \sqrt{\frac{1}{\mu_0 \epsilon}} = \sqrt{\frac{1}{\mu_0 \epsilon_0 \epsilon_r}} = \sqrt{\frac{1}{\mu_0 \epsilon_0 n^2}} = \frac{c}{n}$$

One possible and common solution to the wave equation is the three-dimensional plane harmonic wave function:

$$U(x, y, z, t) = U_0 \cos(\mathbf{k} \cdot \mathbf{r} - \omega t)$$

Where the position vector  $\mathbf{r}$  and wave vector  $\mathbf{k}$  are defined by:

$$\mathbf{r} = x\mathbf{i} + y\mathbf{j} + z\mathbf{k}$$

$$\mathbf{k} = k_x\mathbf{i} + k_y\mathbf{j} + k_z\mathbf{k}$$

The plane harmonic wave function can also be written using Euler's identity:

$$e^{i\theta} = \cos \theta + i \sin \theta$$

$$U(x, y, z, t) = U_0 e^{i(\mathbf{k} \cdot \mathbf{r} - \omega t)}$$

While the exponential form also includes an imaginary part, it is understood the real part is the actual physical quantity being represented. Checking that the plane harmonic wave function is a solution in one-dimension  $\mathbf{k} \cdot \mathbf{r} = k_x x$ :

$$\frac{\partial^2 U}{\partial t^2} = \frac{\partial^2}{\partial t^2} U_0 e^{i(k_x x - \omega t)} = \frac{\partial}{\partial t} (-i\omega U_0 i\omega e^{i(k_x x - \omega t)}) = (-i\omega)^2 U_0 e^{i(k_x x - \omega t)} = -\omega^2 U_0 e^{i(k_x x - \omega t)}$$

$$\frac{\partial^2 U}{\partial x^2} = \frac{\partial^2}{\partial x^2} U_0 e^{i(k_x x - \omega t)} = \frac{\partial}{\partial t} \left( ik_x U_0 i \omega e^{i(k_x x - \omega t)} \right) = (ik_x)^2 U_0 e^{i(k_x x - \omega t)} = -k_x^2 U_0 e^{i(k_x x - \omega t)}$$

$$-\omega^2 U_0 e^{i(k_x x - \omega t)} = -v_p^2 k_x^2 U_0 e^{i(k_x x - \omega t)}$$

$$\omega^2 = v_p^2 k_x^2$$

The wave function in one-dimension is a solution when  $v_p = \frac{\omega}{k_x}$

## A.4 Thermal circuit model

Basic equation for parallel plate capacitor [1]:

$$k \frac{d^2 T}{dx^2} = -\sigma E^2$$

Solution to parallel plate capacitor ( $T_0$  referenced at electrodes, see circuit model for complete equation):

$$T - T_0 = \Delta T = \frac{\sigma V_{rms}^2}{8k}$$

Temperature dependence of electrical conductivity:

$$\sigma = \sigma_0 (1 + \alpha \Delta T)$$

Therefore,

$$\Delta T = \frac{\sigma_0 (1 + \alpha \Delta T) V_{rms}^2}{8k}$$

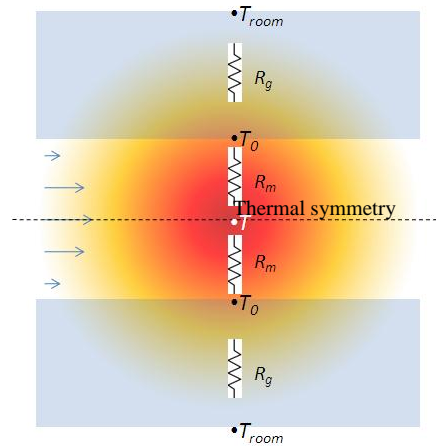
After algebra:

$$\Delta T = \left( \frac{\sigma_0 V_{rms}^2}{8k} \right) \left( 1 - \frac{\sigma_0 \alpha V_{rms}^2}{8k} \right)^{-1}$$

Asymptote at:

$$1 - \frac{\sigma_0 \alpha V_{rms}^2}{8k} = 0$$

$$V_{rms}^2 = \frac{8k}{\sigma_0 \alpha}$$



Nodal equation for temperature:

$$\frac{T_0 - T_{room}}{R_g} + \frac{T_0 - T}{R_m} = 0$$

Solving for node  $T_0$ :

$$T_0 = \frac{R_g T}{R_g + R_m} + \frac{R_m T_{room}}{R_g + R_m}$$

Substitute  $T_0$  into basic equation:

$$T = T_0 + \frac{\sigma V_{rms}^2}{8k}$$

$$T = \left( \frac{R_g T}{R_g + R_m} + \frac{R_m T_{room}}{R_g + R_m} \right) + \frac{\sigma V_{rms}^2}{8k}$$

After algebra:

$$T = \left( \frac{\sigma V_{rms}^2}{8k} + \frac{R_m T_{room}}{R_g + R_m} \right) \left( 1 - \frac{R_g}{R_g + R_m} \right)^{-1}$$

→ However, (spreading) resistances are difficult to calculate

→ Does not consider electrode width

## A.5 Round-trip phase to calculate $L_{FP}$ and $n_{FP}$

Modified round-trip phase as discussed in Chapter 3:

$$2\beta_m(n_{FP}L_{FP} + 2L_\tau) - 2\omega_o\tau = 2\pi m$$

Where:

$$\beta_m = \frac{2\pi}{\lambda_m}, \omega_o = \frac{2\pi c}{\lambda_o}, \tau = \frac{2L_\tau}{c}$$

Therefore,

$$2\left(\frac{2\pi}{\lambda_m}\right)(n_{FP}L_{FP} + 2L_\tau) - 2\left(\frac{2\pi c}{\lambda_o}\right)\left(\frac{2L_\tau}{c}\right) = 2\pi m$$

$$2\left(\frac{2\pi}{\lambda_m}\right)n_{FP}L_{FP} + 4\left(\frac{2\pi}{\lambda_m}\right)L_\tau - 4\left(\frac{2\pi L_\tau}{\lambda_o}\right) = 2\pi m$$

$$\frac{2n_{FP}L_{FP}}{\lambda_m} + \frac{4L_\tau}{\lambda_m} - \frac{4L_\tau}{\lambda_o} = m$$

Solving for  $L_{FP}$ :

$$\frac{2n_{FP}L_{FP}}{\lambda_m} + \frac{4L_\tau}{\lambda_m} - \frac{4L_\tau}{\lambda_o} = m$$

$$\frac{2n_{FP}L_{FP}}{\lambda_m} = m - \frac{4L_\tau}{\lambda_m} + \frac{4L_\tau}{\lambda_o}$$

$$L_{FP} = \left(\frac{\lambda_m}{2n_{FP}}\right)\left(m - \frac{4L_\tau}{\lambda_m} + \frac{4L_\tau}{\lambda_o}\right)$$

$$L_{FP} = \frac{m\lambda_m}{2n_{FP}} - \frac{2L_\tau}{n_{FP}} + \frac{2L_\tau\lambda_m}{n_{FP}\lambda_o}$$

$$L_{FP} = \frac{m\lambda_m}{2n_{FP}} + \frac{2L_\tau}{n_{FP}}\left(\frac{\lambda_m}{\lambda_o} - 1\right)$$

Solving for  $n_{FP}$  :

$$L_{FP} = \frac{m\lambda_m}{2n_{FP}} + \frac{2L_\tau}{n_{FP}} \left( \frac{\lambda_m}{\lambda_0} - 1 \right)$$

$$n_{FP}L_{FP} = \frac{m\lambda_m}{2} + 2L_\tau \left( \frac{\lambda_m}{\lambda_0} - 1 \right)$$

$$n_{FP} = \frac{m\lambda_m}{2L_{FP}} + \frac{2L_\tau}{L_{FP}} \left( \frac{\lambda_m}{\lambda_0} - 1 \right)$$

The penetration depth for N+1/2 pairs is provided by Garmire [2] as described in the text:

$$L_{N+1/2} = \frac{\left[ 1 - \frac{n_1 n_2}{n_f^2} \left( \frac{n_1}{n_2} \right)^{2(N+1/2)} \right] \left[ 1 - \left( \frac{n_1}{n_2} \right)^{2(N+1/2)} \right] \left[ \frac{n_1 n_2}{n_i (n_2 - n_1)} \frac{\lambda_0}{4} \right]}{1 - \left( \frac{n_2 n_1}{n_f n_i} \right)^2 \left( \frac{n_1}{n_2} \right)^{4(N+1/2)}}$$

Where:

$$L_\tau = L_{N+1/2}$$

$$n_{FP} = n_i$$

Simplifying the variables in the mirror penetration equation:

$$A = \left[ 1 - \frac{n_1 n_2}{n_f^2} \left( \frac{n_1}{n_2} \right)^{2(N+1/2)} \right] \left[ 1 - \left( \frac{n_1}{n_2} \right)^{2(N+1/2)} \right] \left[ \frac{n_1 n_2}{(n_2 - n_1)} \frac{\lambda_0}{4} \right]$$

$$B = \left( \frac{n_1}{n_2} \right)^{4(N+1/2)}$$

Therefore,

$$L_\tau = \frac{A}{n_{FP} \left[ 1 - \left( \frac{n_2 n_1}{n_f n_{FP}} \right)^2 B \right]}$$

$L_{FP}$  equation:

$$L_{FP} = \frac{m\lambda_m}{2n_{FP}} + \frac{2L_\tau}{n_{FP}} \left( \frac{\lambda_m}{\lambda_0} - 1 \right)$$

Where:

$$L_\tau = \frac{A}{n_{FP} \left[ 1 - \left( \frac{n_2 n_1}{n_f n_{FP}} \right)^2 B \right]}$$

Therefore,

$$L_{FP} = \frac{m\lambda_m}{2n_{FP}} + \frac{2}{n_{FP}} \left[ \frac{A}{n_{FP} \left[ 1 - \left( \frac{n_2 n_1}{n_f n_{FP}} \right)^2 B \right]} \right] \left( \frac{\lambda_m}{\lambda_0} - 1 \right)$$

$$L_{FP} = \frac{m\lambda_m}{2n_{FP}} + \left[ \frac{2A}{n_{FP}^2 \left[ 1 - \left( \frac{n_2 n_1}{n_f n_{FP}} \right)^2 B \right]} \right] \left( \frac{\lambda_m}{\lambda_0} - 1 \right)$$

$$L_{FP} = \frac{m\lambda_m}{2n_{FP}} + \left[ \frac{2A}{n_{FP}^2 - \left( \frac{n_2 n_1}{n_f} \right)^2 B} \right] \left( \frac{\lambda_m}{\lambda_0} - 1 \right)$$

When  $\lambda_m = \lambda_0$ :

$$L_{FP} = \frac{m\lambda_m}{2n_{FP}} + \left[ \frac{2A}{n_{FP}^2 - \left(\frac{n_2 n_1}{n_f}\right)^2} B \right] \left( \frac{\lambda_m}{\lambda_m} - 1 \right)$$

$$L_{FP} = \frac{m\lambda_m}{2n_{FP}}$$

Solving for  $n_{FP}$

$$L_{FP} = \frac{m\lambda_m}{2n_{FP}} + \left[ \frac{2A}{n_{FP}^2 - \left(\frac{n_2 n_1}{n_f}\right)^2} B \right] \left( \frac{\lambda_m}{\lambda_0} - 1 \right)$$

$$L_{FP} - \frac{m\lambda_m}{2n_{FP}} = \frac{2A \left( \frac{\lambda_m}{\lambda_0} - 1 \right)}{n_{FP}^2 - \left( \frac{n_2 n_1}{n_f} \right)^2} B$$

$$\frac{2n_{FP} L_{FP}}{2n_{FP}} - \frac{m\lambda_m}{2n_{FP}} = \frac{2A \left( \frac{\lambda_m}{\lambda_0} - 1 \right)}{n_{FP}^2 - B \left( \frac{n_2 n_1}{n_f} \right)^2}$$

$$\frac{2n_{FP} L_{FP} - m\lambda_m}{2n_{FP}} = \frac{2A \left( \frac{\lambda_m}{\lambda_0} - 1 \right)}{n_{FP}^2 - B \left( \frac{n_2 n_1}{n_f} \right)^2}$$

$$4n_{FP} A \left( \frac{\lambda_m}{\lambda_0} - 1 \right) = (2n_{FP} L_{FP} - m\lambda_m) \left[ n_{FP}^2 - B \left( \frac{n_2 n_1}{n_f} \right)^2 \right]$$

$$4n_{FP}A\left(\frac{\lambda_m}{\lambda_0}-1\right) = 2L_{FP}n_{FP}^3 - m\lambda_m n_{FP}^2 - 2n_{FP}L_{FP}B\left(\frac{n_2n_1}{n_f}\right)^2 + m\lambda_m B\left(\frac{n_2n_1}{n_f}\right)^2$$

$$0 = 2L_{FP}n_{FP}^3 - m\lambda_m n_{FP}^2 - 2n_{FP}L_{FP}B\left(\frac{n_2n_1}{n_f}\right)^2 - 4n_{FP}A\left(\frac{\lambda_m}{\lambda_0}-1\right) + m\lambda_m B\left(\frac{n_2n_1}{n_f}\right)^2$$

$$0 = 2L_{FP}n_{FP}^3 - m\lambda_m n_{FP}^2 - 2n_{FP}\left[L_{FP}B\left(\frac{n_2n_1}{n_f}\right)^2 + 2A\left(\frac{\lambda_m}{\lambda_0}-1\right)\right] + m\lambda_m B\left(\frac{n_2n_1}{n_f}\right)^2$$

Linear approximation:

$$0 = -2n_{FP}\left[L_{FP}B\left(\frac{n_2n_1}{n_f}\right)^2 + 2A\left(\frac{\lambda_m}{\lambda_0}-1\right)\right] + m\lambda_m B\left(\frac{n_2n_1}{n_f}\right)^2$$

$$2n_{FP}\left[L_{FP}B\left(\frac{n_2n_1}{n_f}\right)^2 + 2A\left(\frac{\lambda_m}{\lambda_0}-1\right)\right] = m\lambda_m B\left(\frac{n_2n_1}{n_f}\right)^2$$

$$n_{FP} = \frac{1}{2}m\lambda_m B\left(\frac{n_2n_1}{n_f}\right)^2\left[L_{FP}B\left(\frac{n_2n_1}{n_f}\right)^2 + 2A\left(\frac{\lambda_m}{\lambda_0}-1\right)\right]^{-1}$$

When  $\lambda_m = \lambda_0$ :

$$n_{FP} = \frac{1}{2}m\lambda_m B\left(\frac{n_2n_1}{n_f}\right)^2\left[L_{FP}B\left(\frac{n_2n_1}{n_f}\right)^2 + 2A\left(\frac{\lambda_m}{\lambda_m}-1\right)\right]^{-1}$$

$$n_{FP} = \frac{1}{2}m\lambda_m B\left(\frac{n_2n_1}{n_f}\right)^2\left[L_{FP}B\left(\frac{n_2n_1}{n_f}\right)^2\right]^{-1}$$

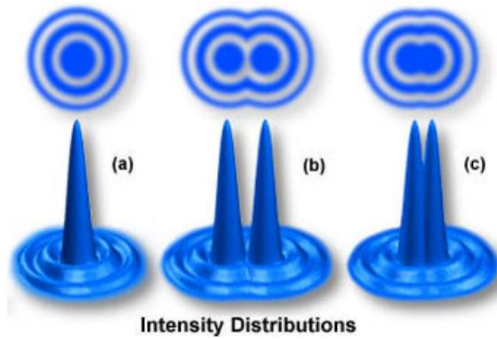
$$n_{FP} = \frac{1}{2}m\lambda_m [L_{FP}]^{-1}$$

## References

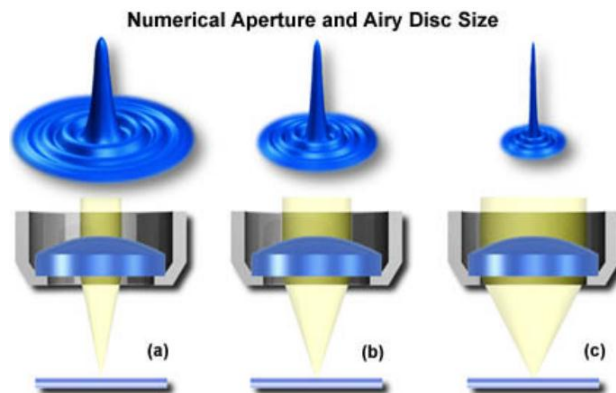
- [1] A. Ramos, H. Morgan, N.G. Green, and A. Castellanos, "Ac electrokinetics: a review of forces in microelectrode structures," *J. Phys. D: Appl. Phys.* vol. 31, no. 18, pp. 2338-2352, 1998.
- [2] E. Garmire, "Theory of a quarter-wave-stack dielectric mirrors used in a thin Fabry-Perot filter," *Applied Optics*, vol. 42, no. 27, pp. 5442-5449, 2003.

## Appendix B: Diffraction limit of microscope

The diffraction limit is the resolution of the microscope, determined by the ability to resolve two Airy disks.



This figure illustrates (a) a hypothetical Airy disk that consists of a diffraction pattern containing a central maximum (typically termed a zeroth order maximum) surrounded by additional order maxima in decreasing brightness that make up the intensity distribution. The Airy disk is resolvable in (b) but not resolvable in (c). Reproduced from [2]



The figure illustrates the effect of numerical aperture on the size of Airy disks imaged with a series of hypothetical objectives of the same focal length, but differing numerical apertures. With small numerical apertures, the Airy disk size is large. Reproduced from [2]

Resolution between point-spread functions:

$$R = \frac{1.22\lambda}{NA_{condenser} + NA_{objective}}$$

If both numerical apertures are the same:

$$R = \frac{1.22\lambda}{2NA} = \frac{0.61\lambda}{NA}$$

Magnification	Plan Achromat (NA)	Plan Fluorite (NA)	Plan Apochromat (NA)
0.5x	0.025	n/a	n/a
1x	0.04	n/a	n/a
2x	0.06	n/a	0.10
4x	0.10	0.13	0.20
10x	0.25	0.30	0.45
20x	0.40	0.50	0.75
40x	0.65	0.75	0.95
40x (oil)	n/a	1.30	1.00
60x	0.75	0.85	0.95
60x (oil)	n/a	n/a	1.40
100x (oil)	1.25	1.30	1.40
150x	n/a	n/a	0.90

Reproduced from [2]

Using a linear regression between 2x and 3x magnifications, a 3x lens has a NA of 0.08.

Therefore,

$$R_{blue} = \frac{0.61(450\text{nm})}{0.08} = 3.43\mu\text{m}$$

$$R_{IR} = \frac{0.61(880\text{nm})}{0.08} = 6.71\mu\text{m}$$

This is the best possible resolution, not considering other optical aberrations.

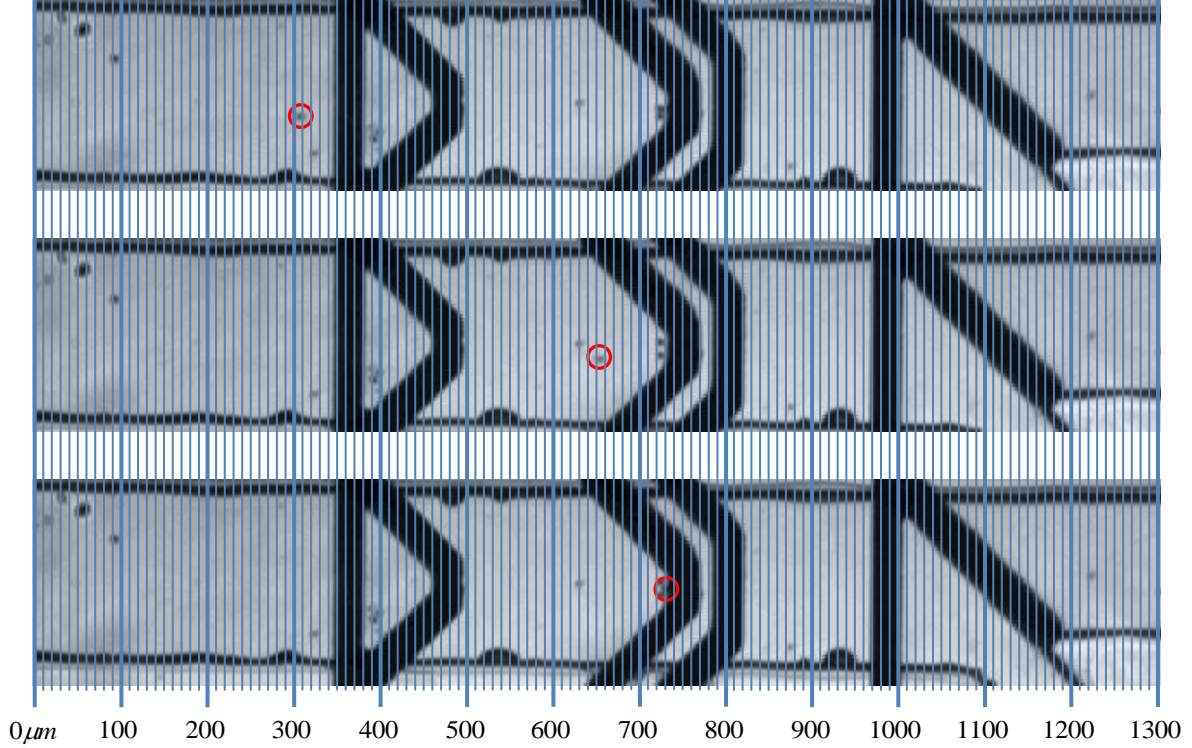
## References

[1] A. Ramos, H. Morgan, N.G. Green, and A. Castellanos, "Ac electrokinetics: a review of forces in microelectrode structures," *J. Phys. D: Appl. Phys.* vol. 31, no. 18, pp. 2338-2352, 1998.

[2] <http://www.olympusmicro.com/primer/anatomy/numaperture.html>

## Appendix C: Additional experimental work

### C.1 DEP force magnitude from particle velocity



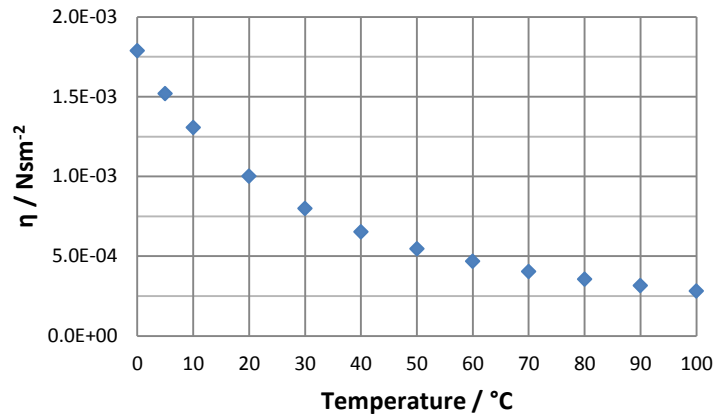
From the movie frames above, the velocity of the polystyrene sphere is the following:

$$v = \frac{655 \mu\text{m} - 310 \mu\text{m}}{(1\text{s} / 200 \text{ frames})(25 \text{ frames})} = 2760 \mu\text{m} / \text{s}$$

The magnitude of the DEP force is approximately equal to the magnitude of Stokes drag [1, 2]:

$$|F_{DEP}| = |F_{Stokes}| = 6\pi\eta Rv$$

where  $\eta$  is the viscosity of the fluid,  $R$  is the radius of the particle, and  $v$  is the velocity of the particle. The viscosity of the water is very temperature dependent [3], and is about  $0.5 \text{ mNs m}^{-2}$  at  $55^\circ\text{C}$ . This temperature was chosen by guessing that the temperature rise due to joule heating is about  $30^\circ\text{C}$ .



Viscosity of water with temperature dependence. Data from [3]

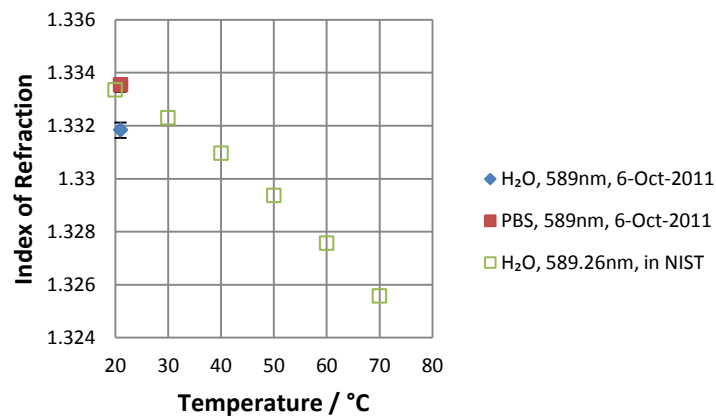
The radius of the particle is tricky to determine by imaging because of the diffraction limit. Since the polystyrene spheres are supposed to be  $7\mu\text{m}$ , then the radius is  $3.5\mu\text{m}$ . This results in a DEP force of about  $90\text{pN}$ .

## C.2 RI measurements using lab refractometer

The laboratory refractometer used in this experiment was the Bausch & Lomb Abbe-3L, available at CSU. An image of the refractometer is seen below.



Bausch & Lomb Abbe refractometer. (Reproduced from [4])



Water and PBS data from Bausch & Lomb Abbe refractometer, and NIST values for water.

As seen in the data, the water data is off compared to the NIST data [5]. The refractometer is likely out of calibration.

### C.3 Table of experiments

Experiment Date / Experiment #	Medium in Channel	Borosilicate Chip ID	Comments
<b>Joule heating experiments</b>			
09-Apr-2011	PBS	05-Apr-2011	
16-Apr-2011	PBS	05-Apr-2011	
<b>Isothermal apparatus experiments</b>			
28-Jun-2011 1 and 2	PBS		Begin implementation of sealing water box. Difficult of obtain data when air bubbles get trapped underneath lid of the water box.
07-Jul-2011 3	Air	28-Jul-2011	Begin implementation of <b>not</b> sealing the water box. Difficult to obtain data because of water surface fluctuations.
10-Jul-2011 4	Air	28-Jun-2011	Begin implementation of plastic window places in front of microscope objective to avoid water surface fluctuations.
10-Jul-2011 5	PBS	28-Jun-2011	
17-Jul-2011 6	Air	28-Jun-2011	Time measurement, temperature pattern: 30°C, 50°C, 40°C.
17-Jul-2011 7	PBS	28-Jun-2011	Time measurement, temperature pattern: 30°C, 50°C, 40°C. Shows signs of polymer swelling.
18-Jul-2011 8	Air	28-Jun-2011	Time measurement, temperature pattern: 30°C, 50°C, 40°C.
18-Jul-2011 9	PBS	28-Jun-2011	Time measurement, long wait time at 30°C, ramp up to 50°C.
22-Jul-2011 10	PBS	28-Jun-2011	Begin implementation of short nanotubes. Time measurement, temperature pattern: 30°C, 50°C, 40°C.

24-Jul-2011 11	Air	16-Nov-2010	Time measurement, temperature pattern: 30°C, 50°C, 40°C.
31-Jul-2011 12	PBS	28-Jun-2011	Temperature pattern: 30°C, 50°C, 40°C.
01-Aug-2011 13	PBS	28-Jun-2011	Temperature pattern: 30°C, 50°C, 40°C.
04-Aug-2011 14	PBS	28-Jun-2011	Temperature pattern: 30°C, 50°C, 40°C, 70°C, 60°C.
11-Aug-2011 15	DI H <sub>2</sub> O	28-Jun-2011	Temperature pattern: 30°C, 50°C, 40°C.
13-Aug-2011 16	DI H <sub>2</sub> O	28-Jun-2011	Temperature pattern: 30°C, 50°C, 40°C, 70°C, 60°C.
30-Aug-2011 17	DI H <sub>2</sub> O	20-Aug-2011	Temperature pattern: 30°C, 50°C, 40°C, 70°C, 60°C.
05-Sep-2011 18	DI H <sub>2</sub> O	20-Aug-2011	Temperature pattern: 30°C, 50°C, 40°C, 70°C, 60°C.
08-Sep-2011 19	PBS	20-Aug-2011	Temperature pattern: 30°C, 50°C, 40°C, 70°C, 60°C.
16-Oct-2011 20	DI H <sub>2</sub> O	30-Sep-2011	Temperature pattern: 30°C, 50°C, 40°C, 70°C, 60°C. Five air hole interpolation, difficult to fit 30°C.
19-Oct-2011 21	DI H <sub>2</sub> O	30-Sep-2011	Temperature pattern (new): 30°C, 60°C, 40°C, 70°C, 50°C. Five air hole interpolation, difficult to fit 30°C.
25-Oct-2011 22	Air	30-Sep-2011	Cannot interpolate air holes, but profile is consistent with temp.
<b>Polymer swelling experiments</b>			
26-Oct-2011 23	DI H <sub>2</sub> O	30-Sep-2011	
26-Oct-2011	DI H <sub>2</sub> O	30-Sep-2011	
14-Nov-2011	DI H <sub>2</sub> O	05-Apr-2011	
28-Nov-2011	PBS	05-Apr-2011	

## References

- [1] S. Ogata, T. Yasukawa, and T. Matsue, "Dielectrophoretic manipulation of a single chlorella cell with dual-microdisk electrode," *Bioelectrochemistry*, vol. 54, no. 1, pp. 33-37, 2001.
- [2] M. Dürr, J. Kentsch, T. Müller, T. Schnelle, and M. Stelzle, "Microdevices for manipulation and accumulation of micro- and nanoparticles by dielectrophoresis," *Electrophoresis*, vol. 24, no. 4, pp. 722-731, 2003.
- [3] [http://www.engineeringtoolbox.com/water-dynamic-kinematic-viscosity-d\\_596.html](http://www.engineeringtoolbox.com/water-dynamic-kinematic-viscosity-d_596.html)
- [4] [http://chemlab.truman.edu/CHEMLAB\\_BACKUP/PChemLabs/CHEM324Labs/LiquidVapor/Refractometer.htm](http://chemlab.truman.edu/CHEMLAB_BACKUP/PChemLabs/CHEM324Labs/LiquidVapor/Refractometer.htm)
- [5] A. H. Harvey, J. S. Gallagher, and J. M. H. Levelt Sengers, "Revised formulation for the refractive index of water and steam as a function of wavelength, temperature and density," *J. Phys. Chem. Ref. Data*, vol. 27, no. 4, pp. 761-774, 1998.

## Appendix D: COMSOL Multiphysics

This appendix presents basic information regarding COMSOL Multiphysics, which is commercial finite element analysis software program that can solve multi-physics problems. COMSOL Multiphysics version 4.1 is used in the short tutorial. Consequently, the reader is cautioned about differences in other versions of COMSOL. A lot of useful material is already provided in COMSOL via:

- User's Guide
- Introduction to COMSOL Multiphysics
- Support during the terms of the license
- An online discussion forum
- An online model gallery
- Free workshops in which one can obtain a free trial version
- Free webinars discussing particular models

### D.1 DEP force directional arrows

The DEP force in terms of  $\text{grad}(|E\text{-field}|^2)$  was presented with an Arrow surface plot.

COMSOL syntax for Eq. 3.2:

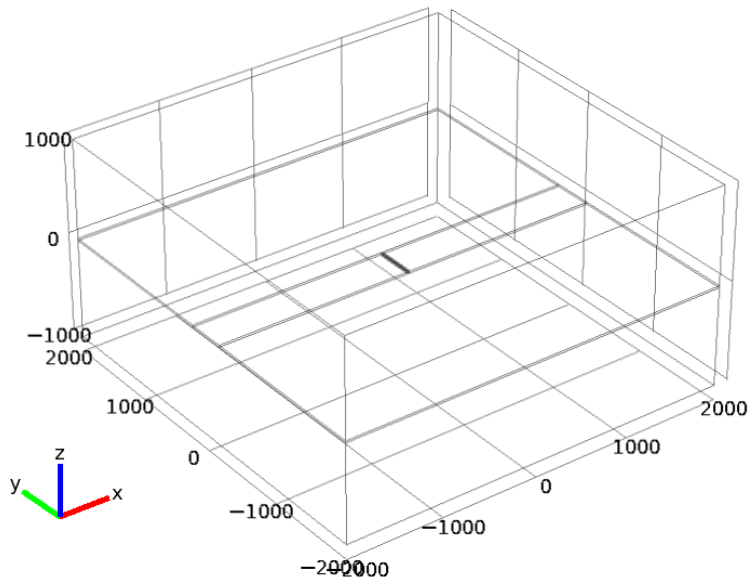
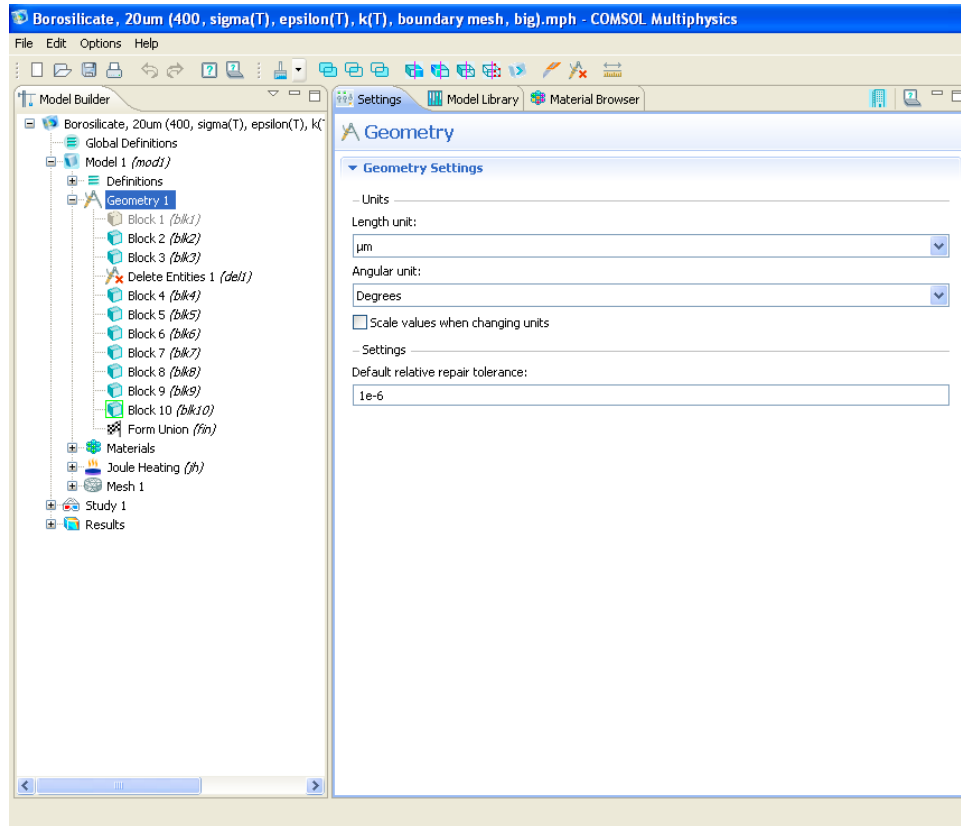
$$-d((\text{sqrt}(\text{es.Ex}^2 + \text{es.Ey}^2))^2, x)$$

COMSOL syntax for Eq. 3.3

$$-d((\text{sqrt}(\text{es.Ex}^2 + \text{es.Ey}^2))^2, y)$$

## D.2 Short tutorial to reproduce joule heating results

1. Define length unit and build geometry.



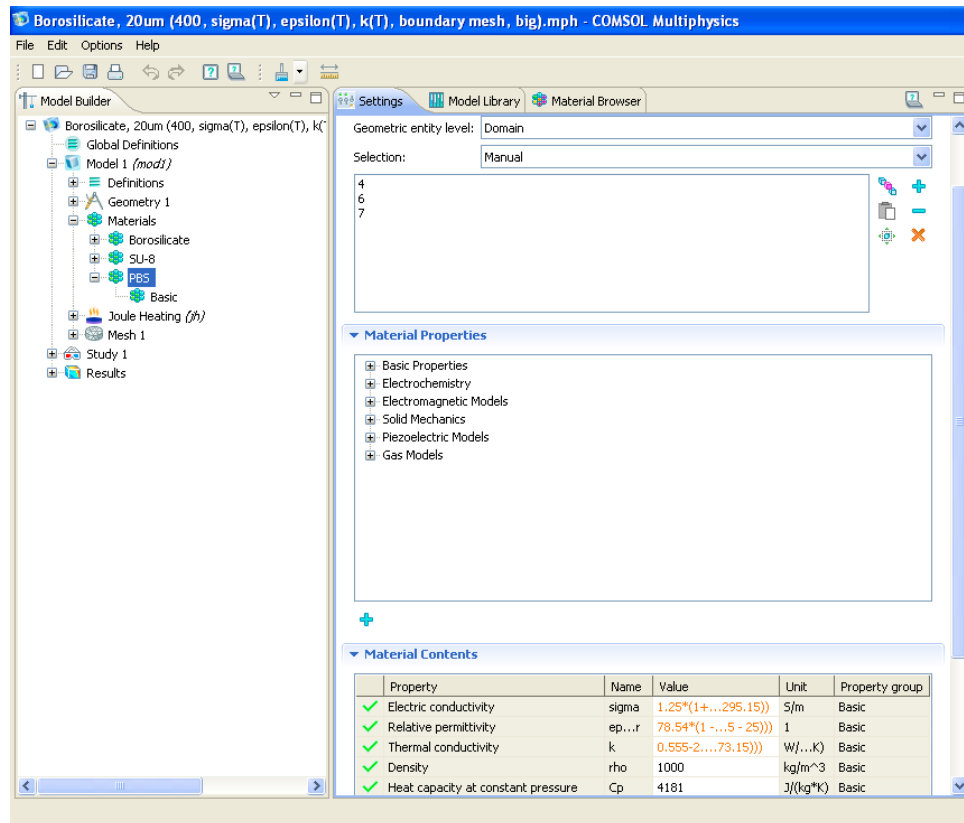
2. Add materials and choose domains for the materials. Note the temperature dependent equations are entered here for PBS and are reproduced from Chapter 3:

$$\sigma(T) = \sigma_0(1 + \alpha(T - T_0))$$

$$\epsilon(T) = 78.54(1 - (T - 25^\circ\text{C})(4.6 \times 10^{-3} - 8.86 \times 10^{-6}(T - 25^\circ\text{C})))$$

$$k(T) = 0.555 - 2.71 \times 10^{-5} \sqrt{T} - T(9.93 \times 10^{-5} - T(6.27 \times 10^{-5} - 4.9286 \times 10^{-7} T))$$

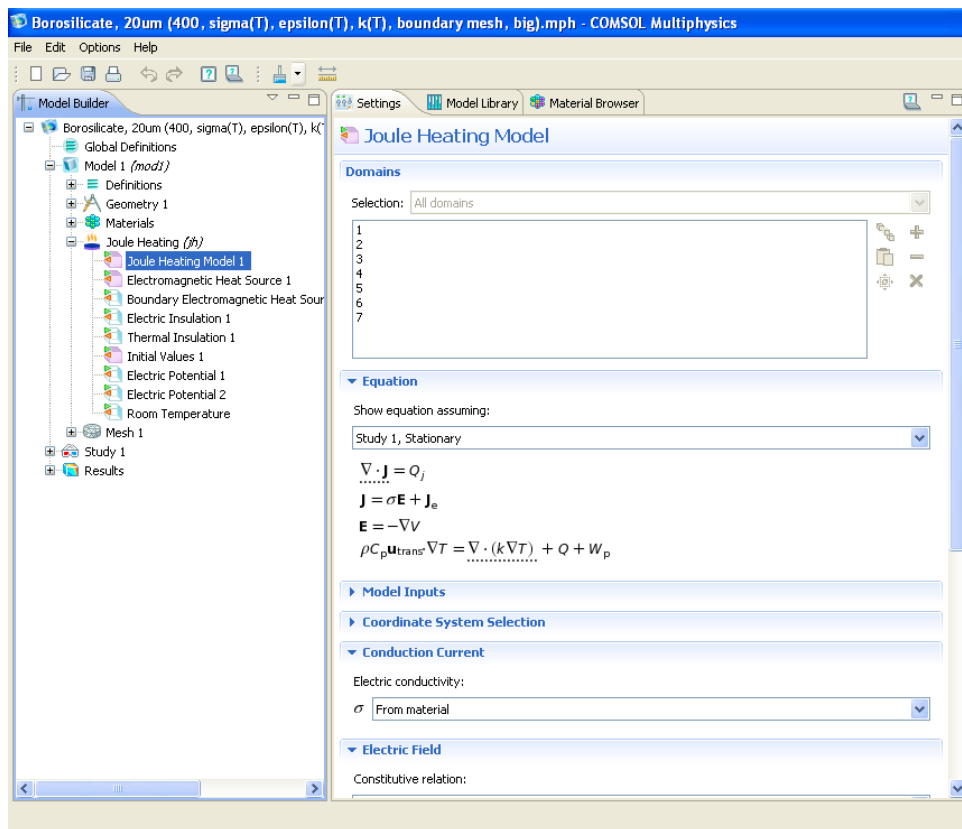
where  $T$  is the dependent variable for temperature,  $T_0$  is the reference temperature,  $\alpha$  is the conductivity temperature coefficient, and  $\sigma_0$  is the electrical conductivity at the reference temperature.



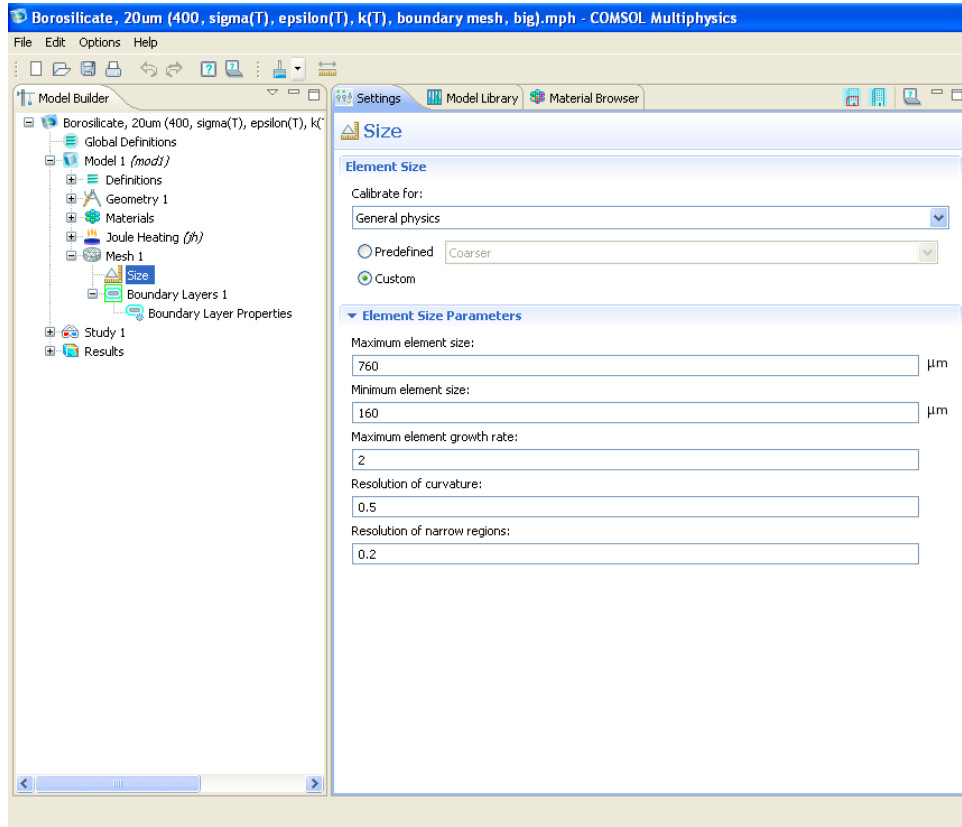
3. The Joule Heating (jh) physics should already be available from starting a new file. Here, one can right click and add boundary conditions, including voltage and room temperature. The joule heating equation is the following from the User's Guide:

$$\rho C_p \frac{\partial T}{\partial t} - \nabla \cdot (k \nabla T) = Q$$

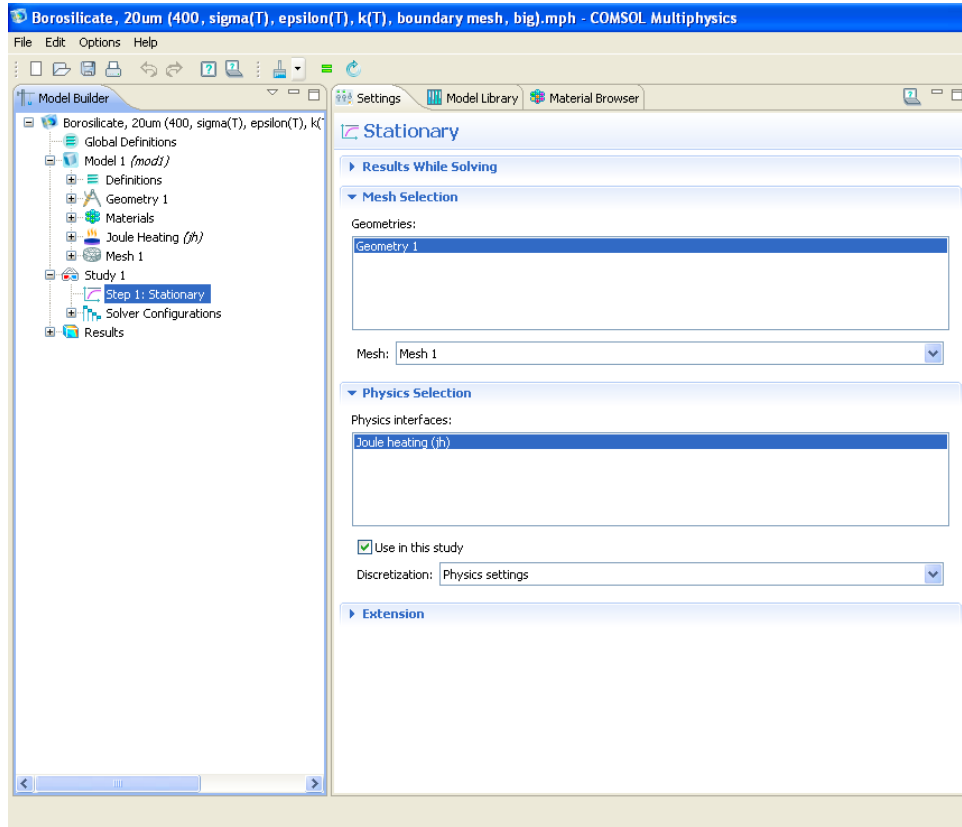
where  $\rho$  is the density,  $C_p$  is the heat capacity, and  $Q$  is the heat source. Consequently, in stationary simulations the density and heat capacity of the material are not considered.



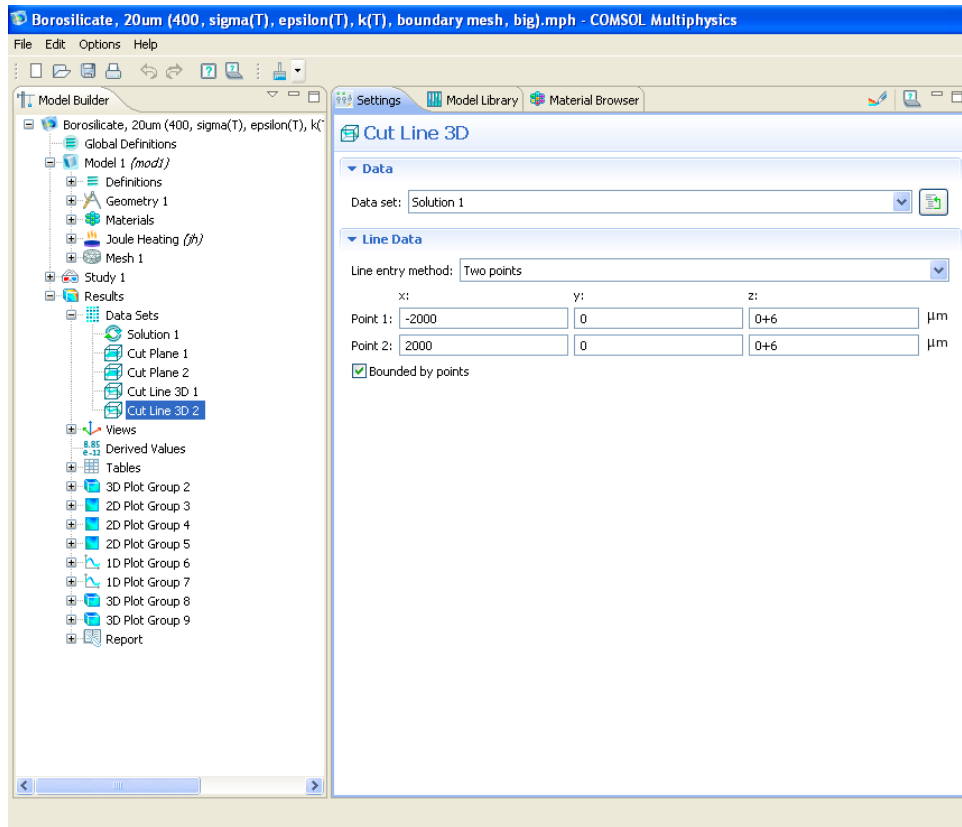
4. Create Mesh. A sensitive parameter is “Resolution of narrow regions”, which can be adjusted to change number of mesh elements. Boundary layers were added by right-clicking on Mesh 1 and adding boundary layers.



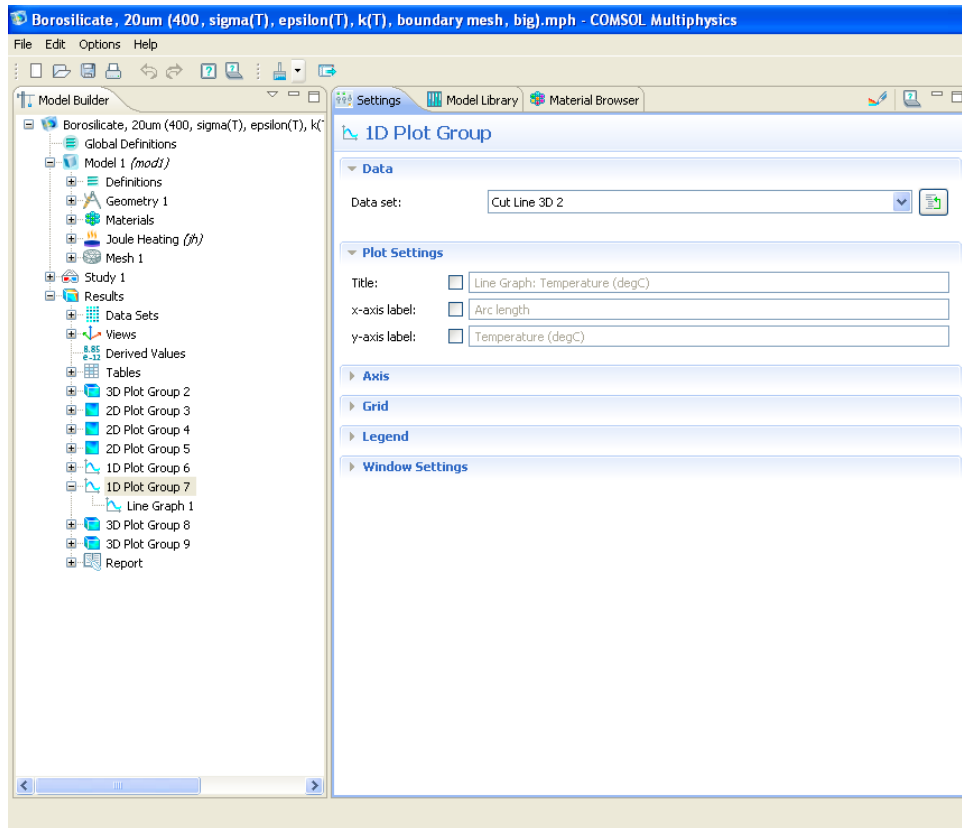
5. Confirm study and run simulation. In this case, a stationary (i.e. steady-state) simulation is desired. The simulation is run by clicking the green equals (=) sign in the toolbar or right-clicking the study and clicking the equals sign.



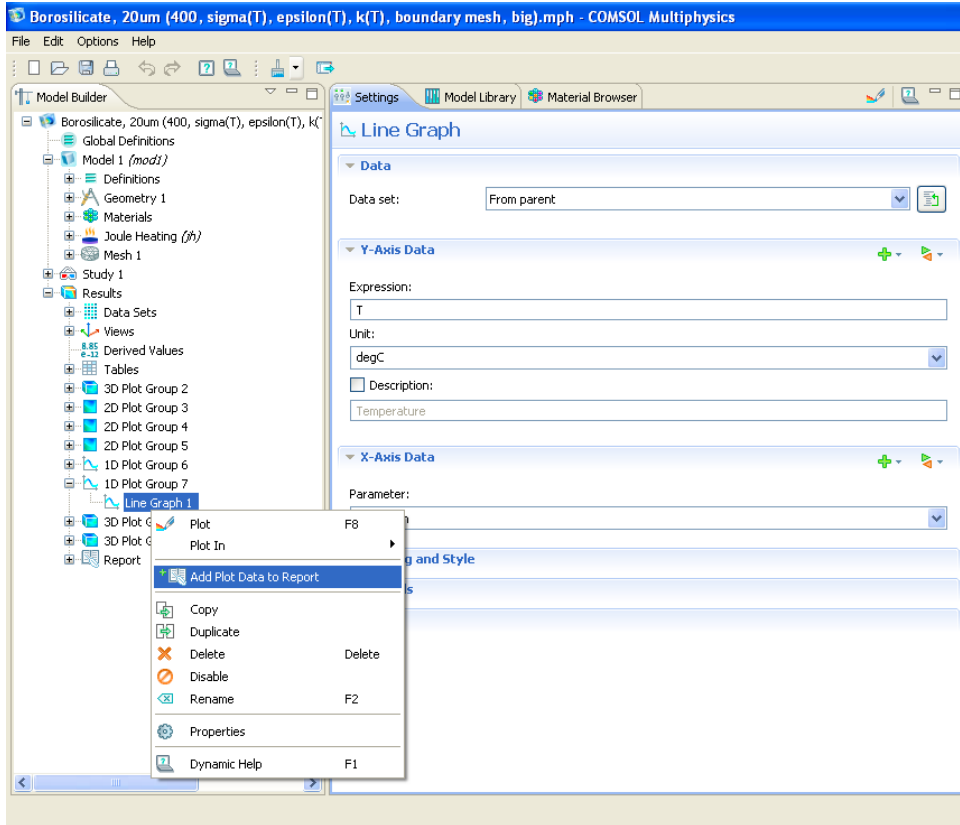
6. After some time, the simulation should be complete. Many different kinds of results can be chosen. In the following steps, a cut line will be chosen and the simulated data will be exported. Right-click on Data Sets and add a Cut Line 3D.



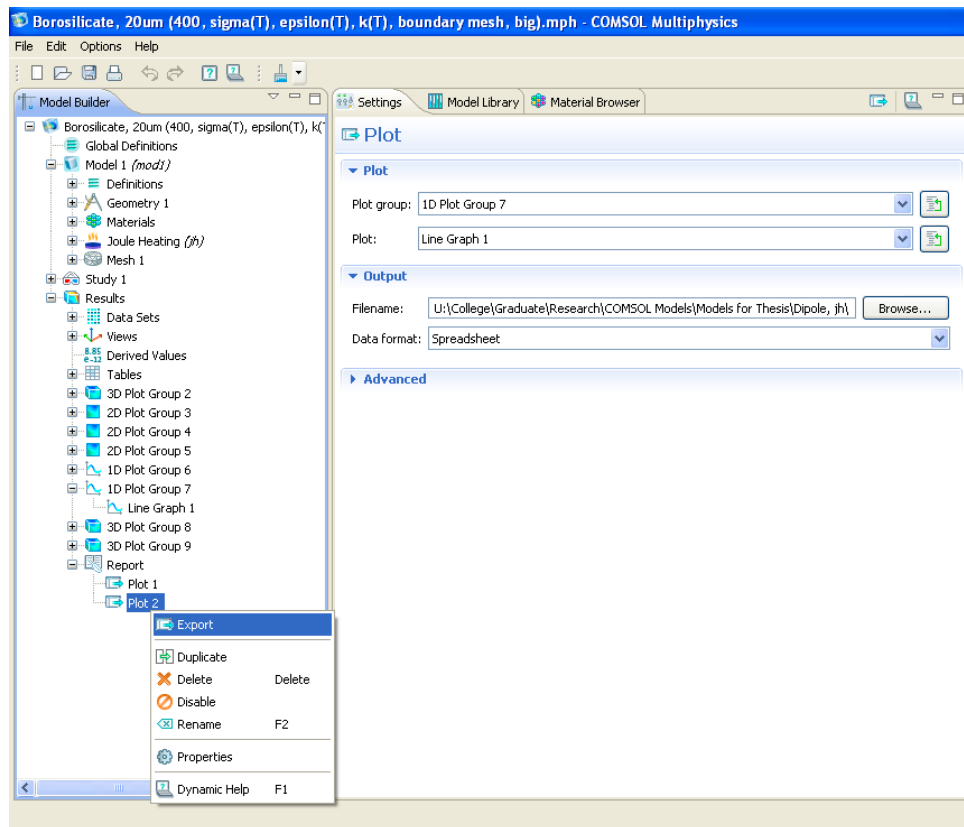
7. Right-click and add a 1D plot group, selecting the desired Data Set. Right-click again and add a Line Graph.



8. Right-click on the Line Graph and select “Add Plot Data to Report”.



9. Choose the output filename and export the data by right-clicking on the Plot and selecting Export.

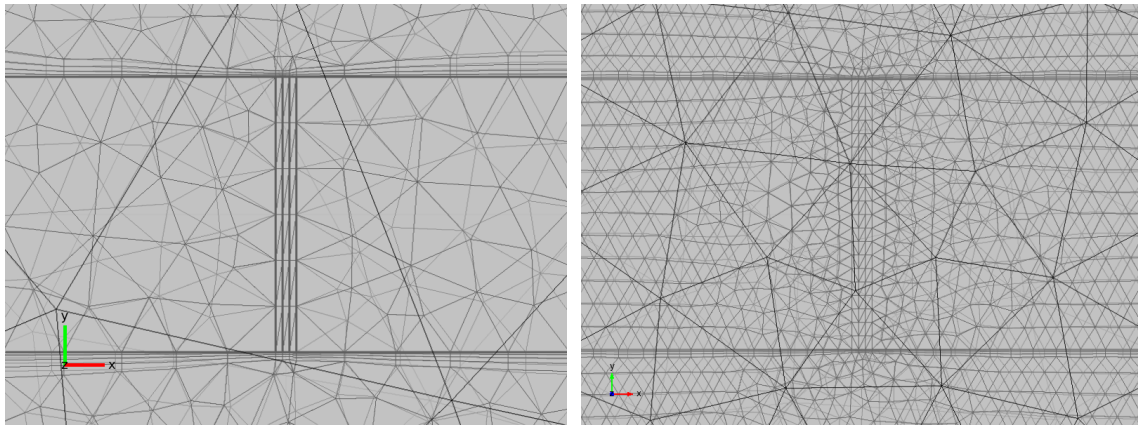


### D.3 Comparison of results on different computers

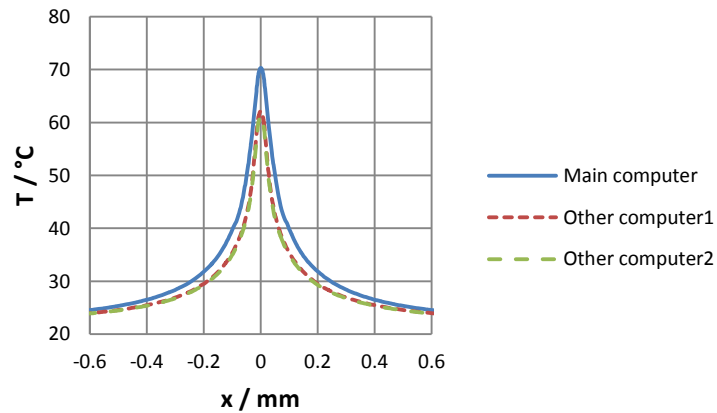
Below is a table of computers with COMSOL Multiphysics. The computer used for all results in the work is the “Main computer”. The results are for a joule heating simulation, which more accurately modeled in 3 dimensions to account for heat transfer in all directions. Consequently, this is a more computationally demanding simulation.

	Main computer	Other computer1	Other computer2
<b>Comsol version</b>	4.1	4.2	4.2
<b>Computer specs</b>	Intel Pentium 4, 768MB or 2GB Ram, 32-bit OS	Intel Core i7, 6GB Ram, 64-bit OS	Intel Core i7, 6GB Ram, 64-bit OS
<b>Custom or pre-defined mesh</b>	Custom	Pre-defined: Normal	Pre-defined: Finer
<b># elements</b>	29,966	238,330	556,136
<b>Degrees of freedom</b>	126,592	809,612	1,784,100
<b>Solution time</b>	164s (~3min)	128s (~2min)	1433s (~24min)

However, I am not technically allowed to use the other computer. This is documented in email correspondence, also included in this appendix section.



Mesh difference between “Main computer” (ver4.1) and “Other computer2” (ver4.2)



In this figure, x-data is taken at center of microfluidic channel, or  $z=0\mu\text{m}$  and  $y=0\mu\text{m}$ . The difference at the maximum temperature is  $9^\circ\text{C}$ . A scaling factor can be calculated as  $(\text{Other computer2})/(\text{Main computer}) = 0.87$ , which is okay to scale within a limited range.

As seen in the figure, the mesh is still a variable for the “Main computer”. The mesh is no longer a variable using “Other computer1”, as it uses an intermediate mesh but returns the same results as “Other computer2”.

Below is correspondence with ENS regarding use of COMSOL on the other computers in the engineering labs.

From: "ENS Help Desk" <help@engr.colostate.edu>  
Subject: Re: Ticket ID #11962 Comsol Multiphysics license error  
Date: Fri, April 6, 2012 4:34 pm  
To: jkindt@engr.colostate.edu

---

==== REPLY ABOVE THIS LINE ====

Dear [jkindt@engr.colostate.edu](mailto:jkindt@engr.colostate.edu),

A reply has been made to your ticket. Below are the ticket details.  
-----

Joel,

Your department did not contribute to the payment of the COMSOL license, therefore, you shouldn't be using it. While ENS technically does not prevent you from using it on the lab computers, it is good courtesy for your department to help pay for it. Currently the burden of paying for it is going to a different department. Because COMSOL, unlike some software, isn't licensed only for classroom use, it IS okay to use it for research, though.

If you do want to continue to use it, please have your advisor contact us about paying in to the shared college license for the software.

Dan Herrick  
ENS Client Services Manager

## Appendix E: PBS recipe

### 1X Phosphate Buffered Saline (PBS)

1. Dissolve 8g NaCl, 0.2g KCl, 1.44g Na<sub>2</sub>HPO<sub>4</sub>, and 0.24g KH<sub>2</sub>PO<sub>4</sub> in 800ml deionized H<sub>2</sub>O.
2. Adjust pH to 7.4 with HCl.
3. Adjust volume to 1L with additional deionized H<sub>2</sub>O.
4. Sterilize by autoclaving on Cycle 5 (liquid cycle). Loosen caps. Put 1-2" of water in bottom of autoclave pan and set bottles in it.
5. After bottles have cooled, label, date and initial. Store at RT. Once bottle is opened for use, store at 4°C.

## Appendix F: TFCalc references for H<sub>2</sub>O, HfO<sub>2</sub>, SiO<sub>2</sub>

Correspondence is in chronological order.

At 3:27 PM -0700 3/1/12, [jkindt@engr.colostate.edu](mailto:jkindt@engr.colostate.edu) wrote:

>Hi,

>

>I would like to know where you found refractive index values vs.

>wavelength for the following materials:

>- H2O

>- HfO2

>- SiO2

>I am using TFCalc 3.2.13 (April 1998), so I am more interested in the

>references for that version. If that is not available, I would still like

>to know what the general references are for those materials.

H2O: Handbook of Optical Constants of Solids II, page 1059

HfO2: Thin-Film Optical Filters, page 505

Kruschwitz and Pawlewicz 1997 OT Paper, page 2158

SiO2: Handbook of Optical Constants of Solids, pages 719 and 749

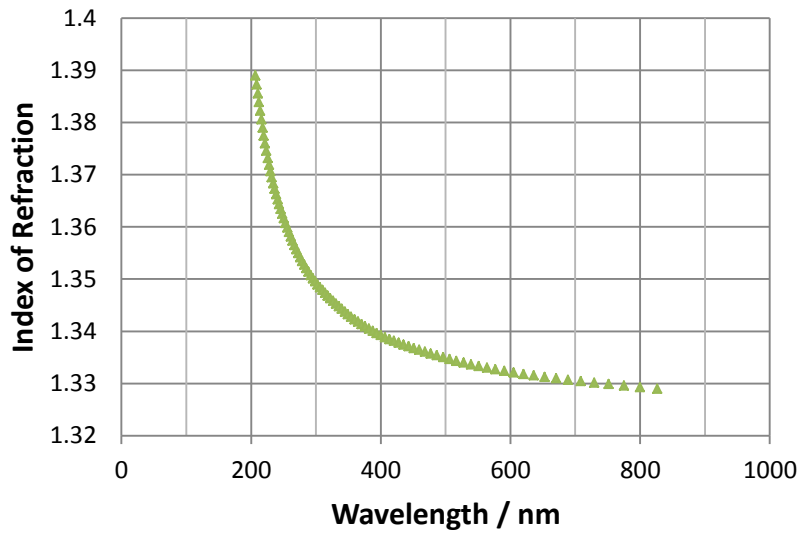
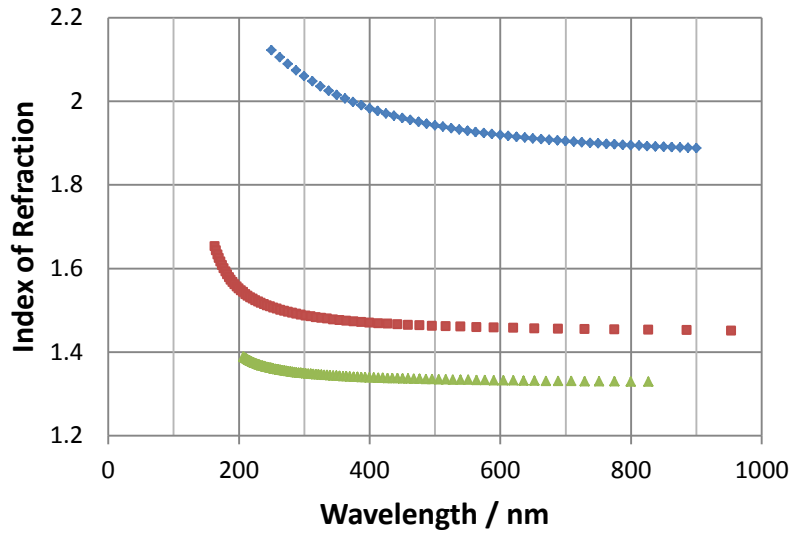
Hope that helps,

Tony

--

Tony Noe	voice:	503-690-2099
Software Spectra, Inc.	fax:	503-690-8159
14025 N.W. Harvest Lane	e-mail:	<a href="mailto:noe@sspectra.com">noe@sspectra.com</a>
Portland, OR 97229, USA	Web site:	<a href="http://www.sspectra.com">http://www.sspectra.com</a>

Below are plots of refractive index for HfO<sub>2</sub>, SiO<sub>2</sub>, and H<sub>2</sub>O directly from the TFCalc material database.



## Appendix G: Relevant journals

#	Relevant Journal (Grouped by Publisher)	Publisher	2010 Impact Factor [1]	5 –year Impact Factor [1]	Notable Papers (First author, year)
1	<i>Biomedical Optics Express</i>	The Optical Society of America (OSA)	New	New	
2	<i>Optics Express</i>	The Optical Society of America (OSA)	3.753	3.939	
3	<i>Applied Optics</i>	The Optical Society of America (OSA)	1.707	1.772	Garmire, 2003
4	<i>Electrophoresis</i>	Wiley	3.569	3.184	Dürr, 2003 Seger-Sauli, 2005
5	<i>Biophysical Journal</i>	Cell Press	4.218	4.692	Guck, 2005
6	<i>Bioelectrochemistry</i>	Elsevier	3.520	3.187	
7	<i>Biosensors and Bioelectronics</i>	Elsevier	5.361	5.397	
8	<i>Journal of Biotechnology</i>	Elsevier	2.970	3.225	
9	<i>Sensors and Actuators A: Physical</i>	Elsevier	1.941	2.011	
10	<i>Sensors and Actuators B: Chemical</i>	Elsevier	3.370	3.340	Gervinskias, 2011
11	<i>Enzyme and Microbial Technology</i>	Elsevier	2.287	2.936	Markx, 1999
12	<i>Biomedical Microdevices</i>	Springer	3.386	3.711	Hou, 2009
13	<i>Microfluidics and Nanofluidics</i>	Springer	3.507	3.632	Sun, 2010
14	<i>Annals of Biomedical Engineering</i>	Springer	2.376	2.799	He, 2005
15	<i>Lab on a Chip</i>	RSC	6.260	6.928	
16	<i>Analytical Chemistry</i>	American Chemical Society (ACS)	5.874	5.903	Ross, 2001
17	<i>Proceedings of the National Academy of Sciences of the United States of America (PNAS)</i>	National Academy of Sciences	9.771	10.591	Tekle, 1991
18	<i>Biomicrofluidics</i>	American Institute of Physics (AIP)	3.896	3.787	
19	<i>Journal of Applied Physics</i>	American Institute of Physics (AIP)	2.079	2.215	
20	<i>Applied Physics Letters</i>	American Institute of Physics (AIP)	3.841	3.863	Song, 2006 Domachuk, 2006

21	<i>Journal of Physical and Chemical Reference Data</i>	American Institute of Physics (AIP)	3.219	4.273	Harvey, 1998
22	<i>J. Phys. D: Appl. Phys</i>	Institute of Physics (IOP)	2.109	2.335	Ramos, 1998 Jaeger, 2007
23	<i>Journal of Micromechanics and Microengineering</i>	Institute of Physics (IOP)	2.281	2.539	Wouters, 2010
24	<i>Journal of Microelectromechanical Systems</i>	IEEE	2.157	2.726	Shao, 2005 *
25	<i>IEEE Sensors Journal</i>	IEEE	1.473	1.590	Shao, 2006 *
26	<i>IEEE Photonics Technology Letters</i>	IEEE	1.989	1.853	Shao, 2008 *
27	<i>IEEE Journal of Quantum Electronics</i>	IEEE	2.480	2.270	Babic, 1992
28	<i>IEEE Photonics Journal (Menoni editor)</i>	IEEE	2.344	2.344	
29	<i>IEEE Transactions on Plasma Science</i>	IEEE	1.076	1.225	Schoenbach, 2002 Schoenbach, 2008
30	<i>IEEE Transactions on Biomedical Engineering</i>	IEEE	1.790	2.347	
31	<i>IEEE Transactions on Biomedical Circuits and Systems</i>	IEEE	1.689	1.990	
32	<i>IEEE Transactions on Instrumentation and Measurement</i>	IEEE	1.106	1.158	

\* Papers from our group.

## References

[1] <http://admin->

[apps.webofknowledge.com/JCR/JCR?PointOfEntry=Home&SID=2DkgE@7K3GDkKn1geed](http://apps.webofknowledge.com/JCR/JCR?PointOfEntry=Home&SID=2DkgE@7K3GDkKn1geed)